THE UNIVERSITY OF MANITOBA

CYCLIC STRESS-STRAIN RESPONSE AND DISLOCATION STRUCTURES IN POLYCRYSTALLINE F.C.C. METALS

By

Yassir El-Madhoun

A thesis
submitted to the faculty of graduate studies
in partial fulfillment of the
requirements for the degree of
Master of Science

DEPARTMENT OF MECHANICAL AND INDUSTRIAL ENGINEERING

WINNIPEG, MANITOBA
AUGUST 2002

THE UNIVERSITY OF MANITOBA

FACULTY OF GRADUATE STUDIES

*****

COPYRIGHT PERMISSION

Cyclic Stress-Strain Response and Dislocation Structures in Polycrystalline F.C.C. Metals

BY

Yassir El-Madhoun

A Thesis/Practicum submitted to the Faculty of Graduate Studies of The University of Manitoba in partial fulfillment of the requirement of the degree

of

MASTER OF SCIENCE

ABSTRACT

Fully reversed strain-controlled push-pull fatigue tests were performed on polycrystalline specimens of commercially 99.0% purity aluminum and commercially 99.53% purity nickel to examine the evolution of dislocation structures and its dependence on the plastic strain amplitude and to investigate the influence of the strain amplitude and fatigue cycles on cyclic deformation behavior. The main objective is to provide qualitative comparison of cyclic deformation and dislocation structures for three f.c.c. polycrystalline metals. These metals are copper for which extensive studies on both single crystal and polycrystal were documented and nickel and aluminum for which low cycle fatigue response is not well conceptualized. Test specimens were prepared according to ASTM specifications E466. Fatigue tests were run under constant strain amplitude in air and room temperature with a constant strain rate of $0.0001 sec^{-1}$. Cyclic deformation behavior was characterized by analyzing the cyclic hardening response, and microstructural observations by means of transmission electron microscopy.

The cyclic stress strain curve (CSSC) of polycrystalline aluminum is characterized by strain hardening response at which the saturation stress increased with plastic strain amplitude at all plastic strain amplitudes tested. On the other hand, CSSC of polycrystalline nickel showed the presence of three distinct regions, namely two cyclic hardening regions at low amplitude and high amplitude ranges and short quasi-plateau region with a slight increase of saturation stress with plastic strain amplitude at intermediate amplitude range. A comparison of the cyclic stress-strain response of polycrystalline aluminum and nickel with previous results revealed that fine-grain material exhibited higher saturation stress than coarse-grained material equivalent to the Hall-Petch relationship of grain size effect. In addition, from the comparison of the cyclic stress-strain curve for both polycrystalline aluminum and nickel with grain size of 40 μm, nickel specimens exhibited higher saturation stress than aluminum specimens due to the high fatigue resistance offered by the nickel specimens. It is found the plastic strain amplitude at which the test was conducted influences the

cyclic hardening rate such that the larger the plastic strain amplitude, the more pronounced the cyclic strain hardening.

Microscopy investigation on the effect of changing strain amplitude on the cyclic hardening reinforces the analysis that dislocation cell structures control the observed deformation response in polycrystalline aluminum. In addition, there is a continual increase in the propensity for cell structure formation in polycrystalline aluminum with plastic strain amplitude and fatigue cycle number. Persistent slip bands and labyrinth structures have not been observed in fatigued pure aluminum. This behavior is due to the high stacking fault energy of aluminum polycrystals, which favors the activation of multiple glide systems and formation of three-dimensional dislocation structures. On the other hand, the dislocation structures observed in fatigued polycrystalline nickel are amplitude dependent. They consist of loop patches at low amplitudes, become mixed with labyrinth structure which becomes cellular at higher amplitudes. In addition, microscopy observations revealed that dislocation cells become increasingly equiaxed and smaller and cell walls become more condensed with increase of strain amplitude.

A correlation between stress-strain response and development of dislocation structures in deformed polycrystalline aluminum and nickel revealed that the reduction of dislocation cell size and wall spacing with plastic strain agrees qualitatively with mesh-length theory of work hardening. These dislocation structures observed in cyclically deformed polycrystalline f.c.c. metals are low energy structures, which govern the plastic hardening (saturated stress) behavior.

It is found that both polycrystalline copper and nickel exhibited similar cyclic deformation behavior as depicted by the plateau in the cyclic stress-strain curve as well as similar dislocation structure evolution from loop patches at low strain amplitudes to labyrinth to cell structure at high strain amplitudes. On the other hand, polycrystalline aluminum exhibited different cyclic deformation behavior and different dislocation structures than copper and nickel as depicted by the hardening

behavior in the cyclic stress-strain curve and the presence of only dislocation cell structures as the dominant dislocation structure at all strain amplitudes. Based on the stacking fault energy values of all three f.c.c. metals (copper, nickel and aluminum) and based on the above comparison, one would note that f.c.c. metals with stacking fault energy value of 55 to 125 mJ/m^2 exhibit similar cyclic deformation response. However, stacking fault energy of 166 mJ/m^2 would be large enough to enhance the cross slip of screw dislocations and hence the development of dislocation cell structures early in fatigue in polycrystalline aluminum.

ACKNOWLEDGEMENTS

I take this opportunity to express my sincere gratitude and to thank Dr. M.N. Bassim for his outstanding advice, guidance, encouragement and understanding throughout the course of this project. It has been of great educational value to work under his supervision.

Thanks are due to Dr. J. Cahoon and Dr. D. Oliver for their valuable and helpful suggestions and discussions. I would also like to acknowledge the technical assistance of Mr. John Van Dorp and Mr. Mike Boskwick at various stages of this work. I would also like to thank my friend Azeden and my colleagues for their help and support.

TABLE OF CONTENTS

LIST OF FIGURES

Page

CHAPTER TWO

CHAPTER THREE

CHAPTER FOUR

CHAPTER FIVE

LIST OF TABLES

Page

GLOSSARY

Burgers vector	Is the vector that defines the magnitude and direction of slip. It is the most characteristic feature of a dislocation.
Climb	Non-conservative movement in which the dislocation moves out of the glide surface normal to the Burgers vector.
Cross slip	A tendency of screw dislocations to glide from one {111}-type plane to another in face-centered cubic metals.
Cyclic hardening curve	It is a plot of stress amplitude σ_a versus cumulative plastic strain $\varepsilon_{p.cum} = 4\ N\ \varepsilon_{pa}$, where N is the number of cycles and ε_{pa} is the plastic strain amplitude. It is also a plot of stress amplitude versus cycle number
Cyclic saturation stress	Cyclic stress after which there is no increase in stress with cycling.
Cyclic stress-strain curve	It is a plot of stress amplitude versus plastic strain amplitude at which strain-controlled fatigue test was conducted.
Debris	Small dislocation loop left behind by moving dislocations and is a direct result of edge jogs on screw dislocations.
Dislocation	Linear lattice defect that is responsible for nearly all aspects of the plastic deformation of metals.
Dislocation dipole	Two edge dislocation lines of the same Burgers vector and opposite sign gliding past each other on parallel slip planes.
Dislocation loop	A closed dislocation line of any arbitrary shape. The character of each dislocation segment of the loop varies continuously from pure edge to mixed to screw dislocation.
Edge dislocation	A dislocation with Burgers vector perpendicular to the dislocation line. For an edge dislocation, the dislocation line moves parallel to the slip direction.
Glide	Conservative movement in which the dislocation moves in the surface which contains both its line and Burgers vector
Hardening coefficient, H	The slope of the hysteresis loop $d\sigma/d\varepsilon$ at the tension tip
Hysteresis loop	Provides cyclic stress-strain response of a cyclically deformed metal by a simultaneous, interdependent recording of the stress and strain signals on an X-Y chart recorder.
Jog	Short element of a dislocation with the same Burgers vector as the line on which it lies. It is a step on the dislocation, which moves it from one atomic slip plane to another.
Labyrinth structure	In multiple slip orientations a common feature is the formation of walls on 2 sets of {100} planes
Loop patch	Cluster or bundle of entangled dislocations composed of parallel dislocation dipoles formed by stacking of dislocation dipoles.
Loop shape parameter, V_H	The area enclosed by the hysteresis loop divided by the area of the circumscribing parallelogram
Low cycle fatigue	Fatigue that occur after relatively few cycles and at a lower than expected force.

Persistent slip band	A highly localized, soft, thin, ladder-like structure of high slip activity located parallel to the primary slip plane
Planar slip	Planar slip traces left by the dislocations suggest easy glide.
Plastic deformation	Occurs by the glide of dislocations and hence the critical shear stress for the onset of plastic deformation is the stress required to move dislocations.
Prismatic dislocation loop	Dislocation loop with Burgers vector not in the plane of the loop. The slip surface defined by the dislocation line and its Burgers vector is a cylindrical surface. It can only move conservatively by glide along the cylindrical surface.
Screw dislocation	A dislocation with Burgers vector parallel to the dislocation line. For a screw dislocation, the dislocation line moves at right angles to the slip direction.
Slip	The result of dislocation glide, which is the most common manifestation of plastic deformation in crystalline solids. It can be envisaged as sliding or successive displacement of one plane of atoms over another on so-called slip planes.
Slip plane	The plane with highest density of atoms and the direction of slip is the direction in the slip plane in which the atoms are most closely spaced.
Vein structure	Dislocation structure forms at low plastic strain amplitudes composing of loop patch structure and dislocation-free matrix.
Wavy slip	Wavy slip traces present in the wake of dislocations indicate cross slip of screw dislocations

CHAPTER ONE: INTRODUCTION

Cyclic hardening and plastic strain localization are key factors in determining the susceptibility of a material to fatigue failure. The study of cyclic plasticity includes investigation of dislocation microstructures and of the cyclic stress and strain response.

Most extensive studies in cyclic deformation of metallic materials toward the understanding of the fundamental mechanisms have been the studies of F.C.C. materials, especially copper and to a lesser extent aluminum and nickel. The basic features of cyclic plastic deformation of F.C.C. metals have been established mainly through studies on single crystals of copper and its alloys.

There are few reports on the cyclic deformation behavior of polycrystalline nickel and aluminum that address both macroscopic behavior such as cyclic hardening as well as microscopic behavior such as dislocation structures. Therefore, the objective of this thesis is **1)** to provide a fundamental study on cyclic deformation behavior of polycrystalline F.C.C. metals such as copper, nickel and aluminum. **2)** to study the fatigue behavior of polycrystalline aluminum and nickel by determining the role of dislocation structures on the cyclic stress-strain (CSS) curve. The experimental work involves studying the effect of plastic strain amplitude on the CSS curve. Analytical electron microscopy will determine the extent of the role of dislocation structures in the saturation stress as well as the cyclic deformation behavior. Also, following the model of Bassim and Liu [1], the evolution of dislocation structures in the various stages of deformation are identified.

Chapter two surveys the existing information on cyclic deformation studies of F.C.C. metals. The purpose is to outline the background for the present study. To further facilitate the reading, a glossary contains a list of the keywords used throughout the thesis is included. **Chapter three** describes the detailed experimental procedure used in the present work as well as the conditions, which the materials were mechanically tested.

The chapter also includes a description of the microscopial techniques used to characterize the evolution of dislocation microstructures.

The results are presented in the form of micrographs, figures and tables, and they have been grouped in two different chapters. Each chapter is closed with a separate discussion and summary. **Chapter four** summarizes the results and discussion for polycrystalline aluminum. The results and discussion for polycrystalline nickel are documented in **chapter five**. **Chapter six** outlines conclusions of the present work.

CHAPTER TWO: LITERATURE REVIEW

2.1 INTRODUCTION

Cyclic deformation universally implies the idea of fatigue, the failure of materials by cyclic loading at stresses either below or above the unidirectional yield stress. Fatigue has been known for more than 150 years, especially for metallic materials that exhibit a lower strength under cyclic loading conditions compared to static loading. For many decades it was a mystery as to why the stress level of the fatigue limit often occurs not only below the rupture but also below the yield stress. Fatigue involves a hierarchy of mechanisms and structures, ranging from individual dislocations to macroscopic cracks, and it depends upon the microstructure and the chemical composition of the material. Fatigue failure is the outcome of a gradual weakening of the material and microscopial observations of metallic materials, prior to fatigue failure, reveals a process of formation of microcracks, which accumulate into a fatal macroscopial crack responsible for fatigue failure. Fatigue is a cumulative effect of cyclic loading on a member or component that ultimately fails by fatigue fracture, which is only the final disastrous stage of a complex sequence of events. Figure 2.1 shows the sequence of processes during fatigue.

Although this sequence represents a very simplified description of the real situation, it applies to the behavior of many metallic materials under cyclic loading conditions and allows us to define the cyclic deformation behavior. The fatigue damage usually evolves from microstructural changes as a consequence of cyclic plastic deformation so the study of the cyclic stress-strain response and its correlation with microstructure leads to a better understanding of the early stages of the fatigue failure process.

Fundamental studies on the nature of fatigue damage must be based on well-designed cyclic deformation experiments in combination with a detailed evaluation of the microstructure failure mechanisms present in cyclically strained materials.

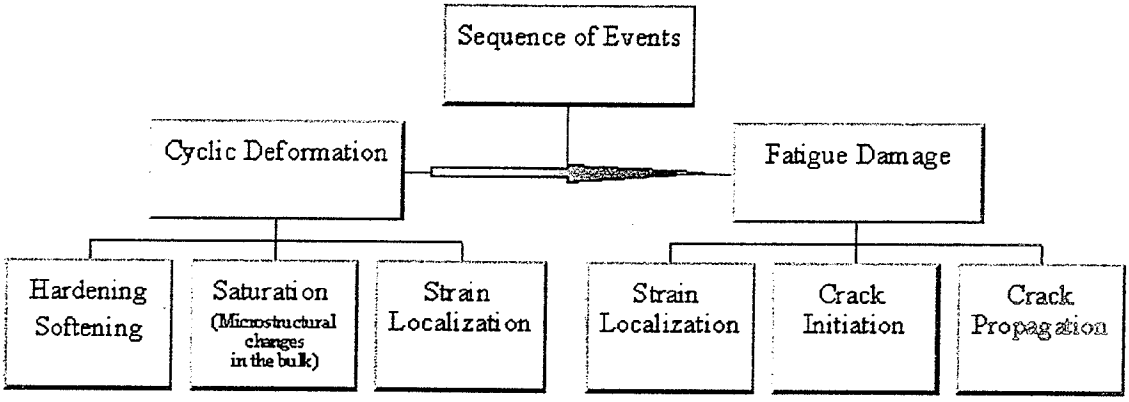

Figure 2.1 Schematic diagram for sequence of events during fatigue [2]

The approach to be followed in this chapter is to review the salient features of cyclic deformation on FCC metals such as copper, nickel and aluminum and then to address the evolution of dislocation structures associated with such cyclic loading.

2.2 THEORY AND BACKGROUND

2.2.1 Strain-Controlled Low Cycle Fatigue Testing

To generate fatigue data, several specimens are subjected to constant amplitude completely reversed cycles in which the strain is the controlled variable. In low cycle fatigue testing, the plastic component of the strain amplitude is characterized by the fatigue ductility properties and the elastic component by the fatigue strength properties of the metal [3].

2.2.2 Fatigue Hardening / Softening Response

Fatigue hardening and/or softening of a material can be presented with respect to fatigue cycle number in a cyclic hardening curve, which is a plot of stress amplitude versus cycle number. The cyclic hardening curve could also be presented as plot of stress amplitude σ_a versus cumulative plastic strain $\varepsilon_{p,cum} = 4\ N\ \varepsilon_{pa}$, where N is the number of cycles and ε_{pa} is the plastic strain amplitude at which the fatigue experiments was conducted. The fatigue response can also be represented in terms of the saturation behavior in cyclic stress-strain curve (CSS) curve, which is a plot of the saturation stress versus the plastic strain amplitude. The cyclic stress-strain curve is usually obtained by connecting the tips of stable hysteresis loops from constant-strain-amplitude fatigue tests of companion samples at different strain amplitudes [4]. A schematic illustration of this method is shown in Figure 2.2.

From cyclic stress-strain curves, one can determine whether or not the material that is cyclically strained softens or hardens (that is, whether the stress amplitude stays constant with constant strain amplitude, or decrease or increase). For metals which cyclically harden, the cyclic stress-strain curve will be above the monotonic stress-strain

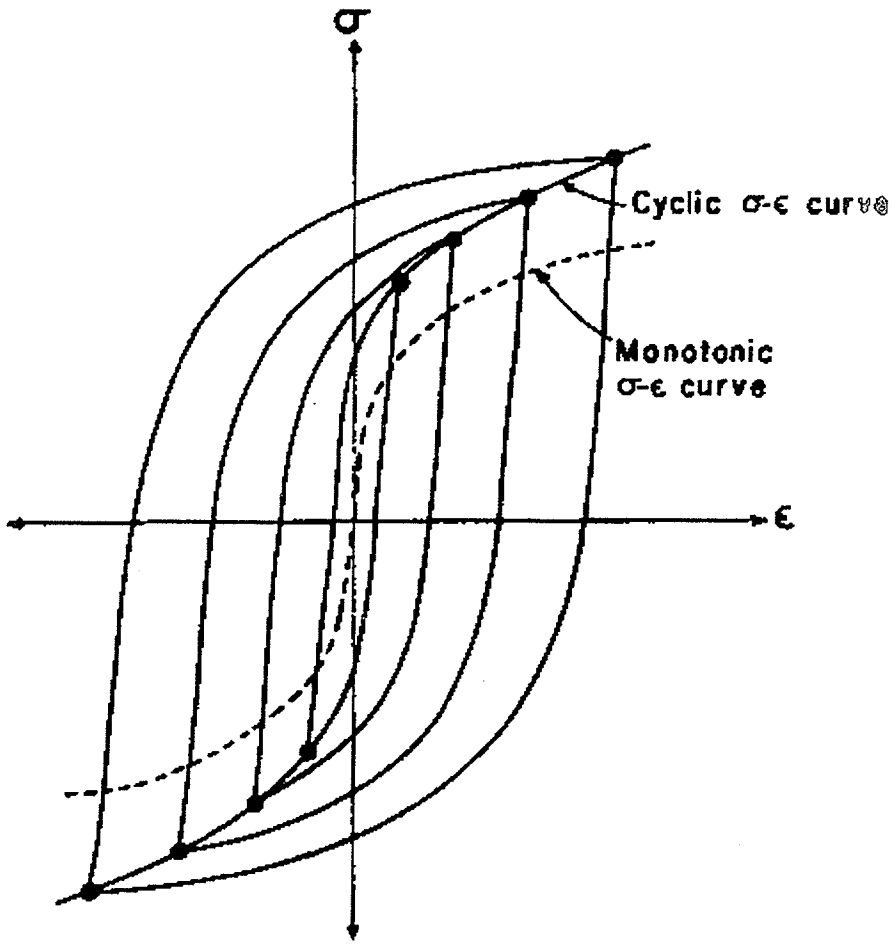

Figure 2.2 Schematic representation of monotonic and cyclic stress-strain curves for a material that cyclic hardens [4]

curve; for metals which soften, the cyclic stress-strain curve will be below the monotonic curve [3].

2.2.3 Stress-Strain Hysteresis Loop

If a metal is cycled to produce plastic deformation of a predetermined amount in both tension and compression, the resulting cyclic stress-strain response will produce a hysteresis loop. Thus, the basic information on the cyclic stress-strain response of a cyclically deformed metal is provided in the form of the stress-strain hysteresis loop. In contrast to monotonic yielding, cyclic deformation does not lead to a unique relationship between stress,σ and strain, ε but rather to a hysteresis loop for each loading cycle. The loop represents the microscopical deformation processes occurring during a load cycle. During low-cycle fatigue testing, the hysteresis loop is provided by a simultaneous, interdependent recording of the stress and strain signals on an X-Y chart recorder. Figure 2.3 shows a schematic of a typical hysteresis loop. The mechanical parameters associated with the hysteresis loop are indicated on the figure.

2.2.4 Characteristics of the Stress Strain Hysteresis Loop

Stress strain hysteresis loops depend not only on the material being tested, but also on the load frequency and the strain control mode. The tips of the loops represent the stress and strain limits for each cycle, and the area inside the complete loop is the energy associated with the plastic work per cycle.

Some important quantities can be taken directly from the hysteresis loop as shown in Figure 2.3. The unloading after the load reversal point in tension, which is described by the coordinates (ε_{max}, σ_{max}) for the maximum strain and stress, occurs with a slope of the tangent that represents the value of Young's modulus. The size of the hysteresis loop can be defined in terms of its width, which represents the strain range ($\Delta\varepsilon$) and its height, which represents the stress range ($\Delta\sigma$). The distance between the maximum stress and the intersection of the extended elastic strain line with the strain axis represents the

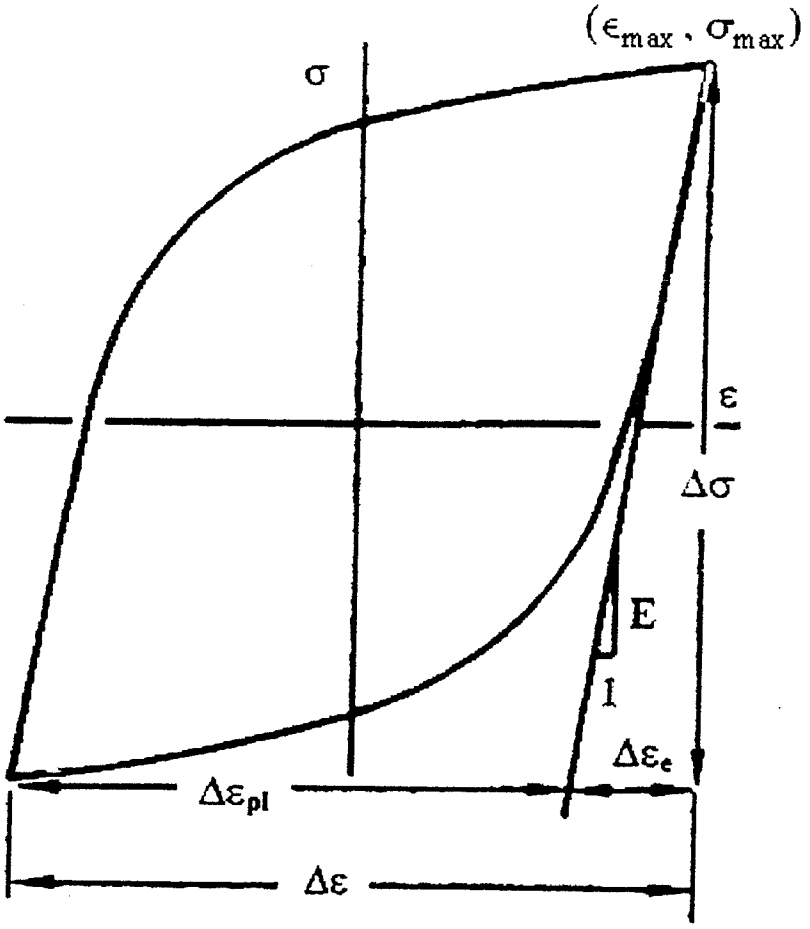

Figure 2.3 Schematic of a typical hysteresis loop showing the stress and strain parameters. [5]

plastic strain ($\Delta\varepsilon_{pl}$). The total elastic strain (ε_{tot}) is composed of both plastic (ε_{pl}) and elastic (ε_{el}) strains ($\varepsilon_{tot} = \varepsilon_{pl} + \varepsilon_{el}$) [2].

2.2.5 Transient Cyclic Deformation Behavior

Three general features can be observed for the hysteresis loop of cyclically strained materials. These are cyclic hardening, cyclic softening and cyclic stability. Cyclic hardening or softening refers to a continuous change in the cyclic strength that may occur throughout a test or at least in the first stage of cyclic deformation. The type of transient behavior is mainly determined by the pretreatment of the material tested as well as the microstructural changes induced by deformation.

2.2.5.1 Cyclic Hardening

Cyclic hardening leading to an increase in the stress amplitude for increasing cycles at constant strain amplitude and subsequently the hysteresis loop becomes larger in size. Figure 2.4 shows the stress course for cyclic hardening and the hysteresis loop shape. Hardening is often attributed to increased dislocation interaction, which increases the resistance to dislocation movement. Thus the trapped dislocations gather in bundles and act as a barrier to further dislocation movement resulting in an increase in the applied stress for the same amount of deformation. Cyclic hardening is a characteristic of annealed pure metals, many aluminum alloys and as-quenched steels [6].

2.2.5.2 Cyclic Softening

Cyclic softening leads to a decrease in the stress amplitude for increasing cycles at constant strain amplitude and a reduction in the size of the hysteresis loop. Figure 2.5 shows the stress course for cyclic softening and the hysteresis loop shape. This behavior indicates that with continuing cycling the material sustains less stress to deform the same amount. Cyclic softening is a characteristic of cold worked pure metals and many steels at small strain amplitudes [6].

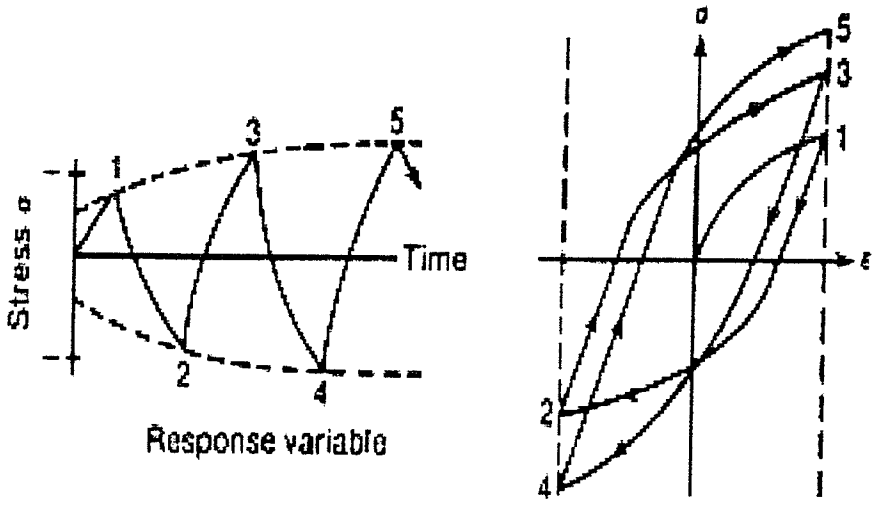

Figure 2.4 Schematic of the stress course and hysteresis loop shape for cyclic hardening. [6]

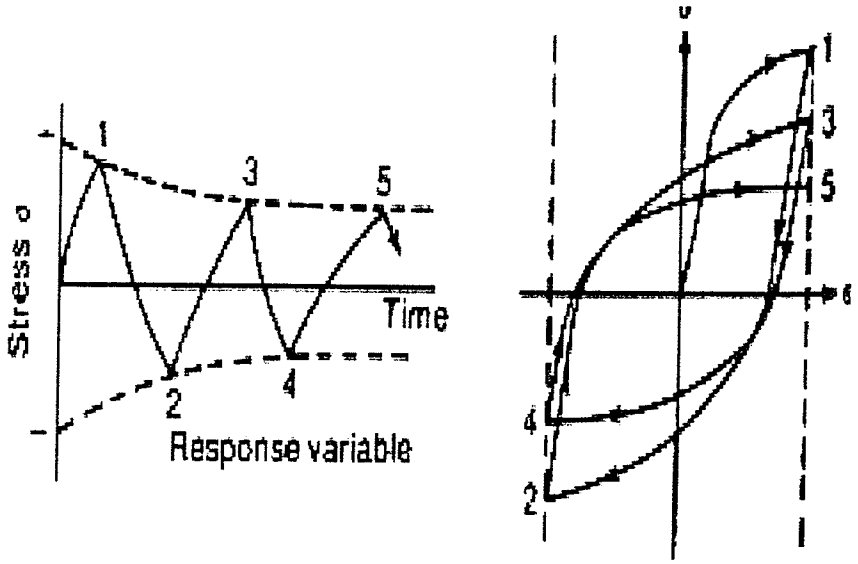

Figure 2.5 Schematic of the stress course and hysteresis loop shape for cyclic softening. [6]

2.2.5.3 Cyclic Stability

Cyclic stability represents steady-state conditions at which the degree to which the stress amplitude of the hysteresis loops increases for each consecutive cycle gradually decreases until eventually the strain amplitude reaches a maximum where there is no further increase in stress amplitude for further cycling. Cyclic stability is reached when the hysteresis loop starts repeating the same loop for many cycles as indicated in Figure 2.6. The corresponding peak stress is the saturation stress, which is an important parameter in evaluating the cyclic stress-strain behavior of a material. This condition is usually achieved in about 20 to 40 % of the fatigue life in materials that are either hardened or softened [6].

2.3 CYCLIC DEFORMATION BEHAVIOR OF SINGLE CRYSTAL F.C.C METALS

Single crystals have been extensively used in the study of fundamental phenomena in deformation processes, such as creep, monotonic and cyclic deformation. Monocrystalline metal has the advantage of clearly defined slip systems and no grain boundary or second phase particle complications. A large number of studies have been conducted on cyclic deformation of metallic single crystals, especially copper single crystal, such as the works of Feltner [7], Hancock and Grosskreutz [8], Winter [9], Woods [10], Basinski et al. [11], Antonopoulos and Winter [12], Finney and Laird [13] and Mughrabi [14,15].

From the study of Mughrabi [15] on copper single crystal the cyclic stress-strain curve can be divided into three regions as shown in Figure 2.7a which is similar to the idealized model of CSS curve for single crystal documented by Mughrabi et al. [16] and shown in Figure 2.7b.

In low-amplitude region (region A), cyclic strain hardening occurs more or less homogeneously and the saturation stress increases with strain amplitude, which is related to the formation of dislocation bundles, and loops due to long-range dislocation glide and

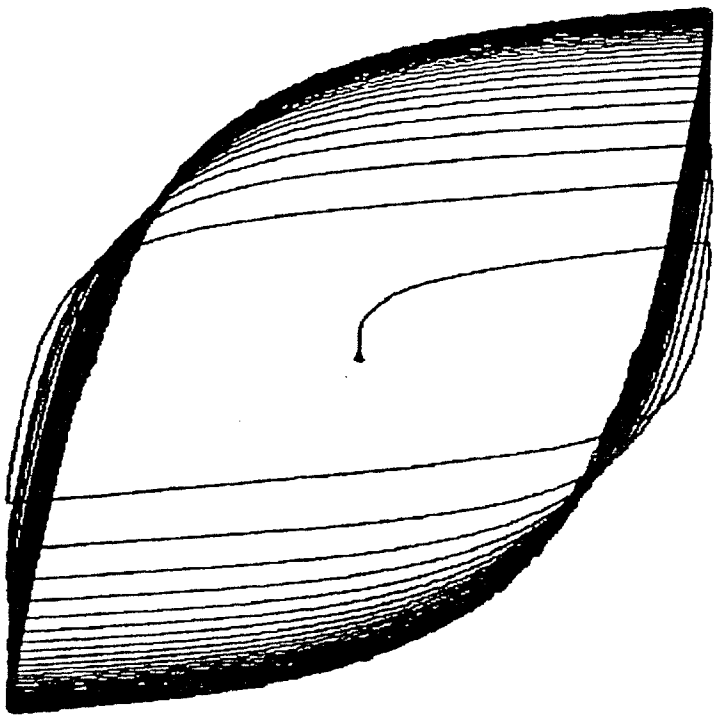

Figure 2.6 Schematic of a typical hysteresis loop showing cyclic saturation. [17]

(a)

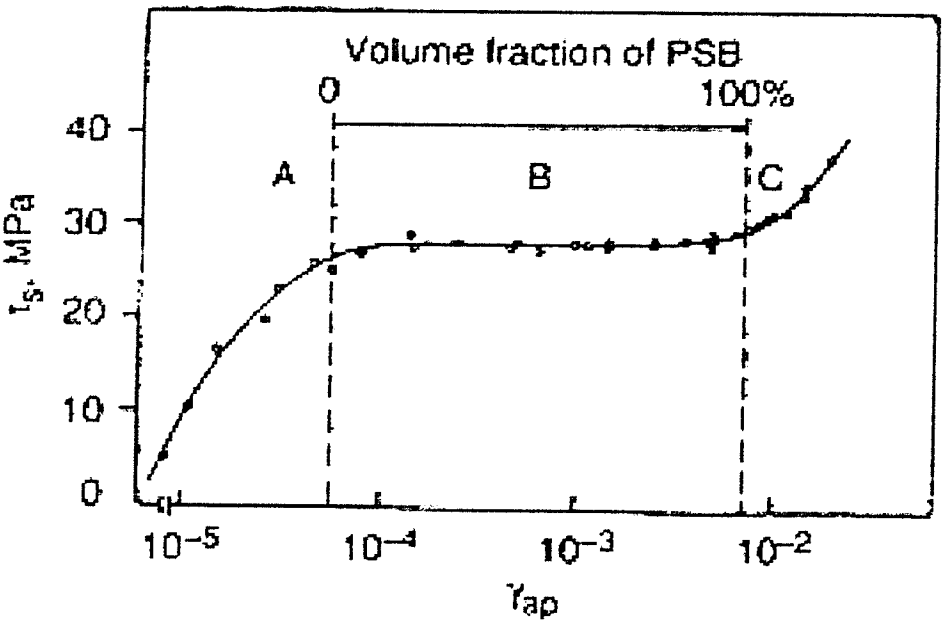

(b)

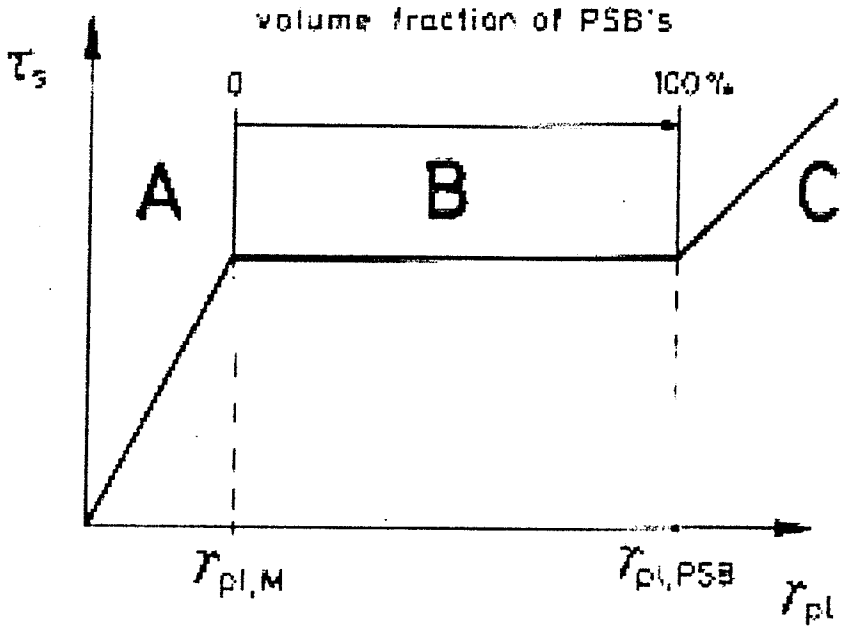

Figure 2.7 Cyclic stress-strain (CSS) curve of monocrystalline copper

(a) CSS curve of monorcrystalline copper oriented for single slip [15]
(b) Idealized CSS curve of single crystal copper [16]

jogs formed at point defects. Feltner [7] suggested that flip-flip model might be in operation in this region. The homogenous deformation is due to the microstructural balance between edge-dislocation and intervening matrix channels piled by screw dislocations. Elongated and fragmented edge-dislocation dipole and loop patches as shown in Figure 2.8a characterize the dislocation pattern in this region. These loop patches cluster into dense bundles called "Veins" as the plastic strain increases. These veins are separated by dislocation-poor channels that are oriented parallel to the veins. The number of cycles to failure is infinite. Thus, the material in this region is below the fatigue limit.

The critical threshold stress level at the end of region A represents the transition point between regions A &B. At this point the stress and strain fatigue limits of the material are determined. At this transition point the "vein" structure in the matrix becomes locally unstable (i.e. it cannot accommodate more strain) and gradually transforms into thin lamellae of persistent slip bands that form parallel to the primary slip plane as shown in Figure 2.8b. This transition is marked by the first development of PSBs and the deformation becomes inhomogeneous and strongly localized in the PSBs.

In the intermediate-amplitude region (plateau, region B), the saturation stress is independent of strain amplitude used. In this region, persistent slip bands (PSBs) form and the amount of PSBs increases with strain amplitude. These bands are regions of localized slip in which the plastic deformation is much larger than the overall deformation of the crystal. The saturation stress, representing essentially the stress required for the localized deformation of the soft PSBs, remains virtually unchanged until the end of the plateau region, when the entire crystal is filled with PSBs. As plastic strain amplitude increased in region B, the volume fraction of the PSBs increases according to the rule of mixtures.

It was found that PSBs were embedded within the matrix composing the Winter's two-phase model [18]. The model of Finney and Laird [13] using bowing out of edge dislocations between walls in the PSB structure and the annihilation of screw components

by cross slip can also explain the saturation behaviors which was supported by TEM observations of Antonopoulos and Winter [12] and Mughrabi et al. [16].

In the low amplitude part of region B, the matrix consists of a vein structure in which single slip prevails, whereas secondary slips form at high amplitudes leading to an arrangement of dipolar wall structure that resembles a cell structure as shown in Figure 2.8c.

In the high-amplitude region (region C), the stress again increases with increasing strain amplitude and PSBs are observed to diminish because the capacity to form new ladder PSBs is exhausted. As a result further structure changes are required to sustain the increase in plastic strain. This region is characterized by the existence of PSB-like dense dipolar walls and dislocation cell structures as shown in Figure 2.8d. Mughrabi [15] suggested that a rearrangement of the existing dislocations and, due to a stress build up, secondary slip systems have been enhanced to contribute to the overall homogeneous plastic deformation with no slip localization causing the cellular structure to form.

2.4 CYCLIC DEFORMATION BEHAVIOR OF SINGLE-PHASE POLYCRYSTALLINE F.C.C. METALS

Study of cyclic deformation of single-phase polycrystalline metals has the advantageous in that anisotropy of mechanical response of the material can be neglected, and in that no second phase particles complicate the microstructural observation.

In polycrystalline metals, the individual crystals have different orientations, and the applied resolved shear stress for slip varies from grain to grain. The grain boundaries, being regions of considerable atomic misfit, act as strong barriers to dislocation motion. The stress strain curve is therefore not simply a single crystal curve averaged over random orientations. Furthermore, the internal stresses around piled-up groups of dislocations at the boundaries of grains that have yielded may cause sources in

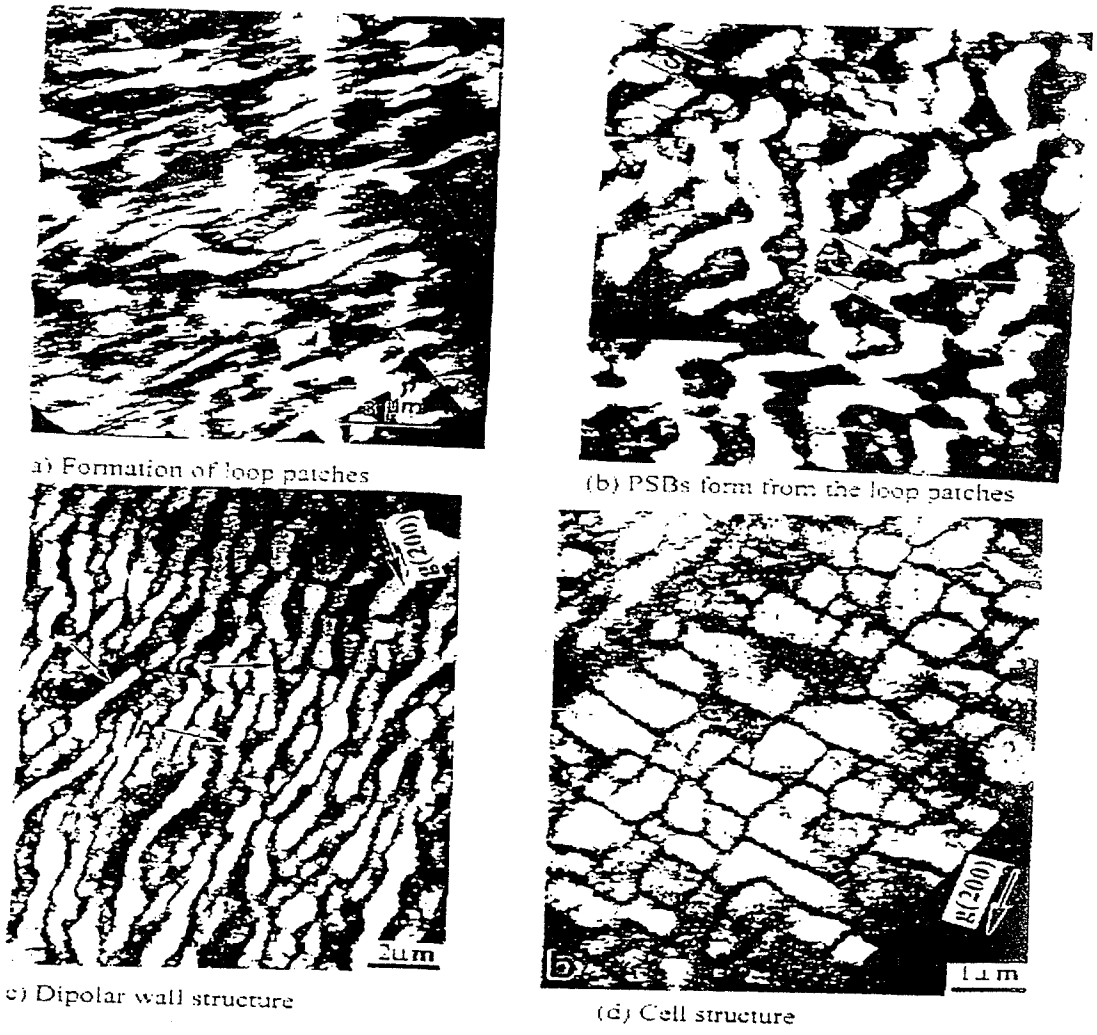

Figure 2.8 Dislocation arrangements in copper single crystals [19]

(a) Formation of loop patches.
(b) PSB's form from the loop patches.
(c) Dipolar wall structure.
(d) Cell structure.

neighboring grains to operate. Thus, the macroscopic yield stress at which all grains yield depends on grain size.

In polycrystals the grains do not deform independently and each grain has its own stress-strain characteristics. As a result the stress-strain response of polycrystals is not a simple "average" over all the grains. Compatibility requirements between the grains of polycrystals lead to the formation of secondary slips in the vicinity of the grain boundaries. Also the equilibrium requirements between the grains result in the existence of an internal stress field within the grains. In polycrystalline materials the textures favoring multi-slip orientations have large effect on the behavior of polycrystals as compared to single crystals.

Rasmussen and Pedersen [20], Bhat and Laid [21], Kuokkala and Kettunen [22] Laird and Buchinger [23] indicated that the polycrystal CSS curve exhibits a plateau similar to that found in monocrystalline copper. Bhat and Laird [21] examined the data available at their time (1978) and came to the conclusion that plateau behavior was a general feature of both single-crystal and polycrystalline metals. They argued that the occurrence of a plateau could be at least as general for polycrystalline materials as it appears to be for single crystals of different metals and alloys. However, Lukas and Kunz [24] and Giese et al. [25] reported no evidence of a plateau in the cyclic stress strain curve as shown in Figure 2.9 and Figure 2.10 respectively.

Mughrabi [26,27] asserted that the saturation stress could not be governed by the PSBs in a polycrystal as in the case of monocrystals, and the plateau could not be expected to occur, because the ladder PSBs are believed to be observed in grains located at the surface, but not be found in the interior of the grains.

In studies performed by Kettunen and Tiainen [28,29] for commercially pure copper, a plateau region with no increase in stress with the increase in the prescribed cyclic strain was observed in CSS curves for both monocrystals and polycrystals as shown in Figure 2.11. Rasmussen and Pedersen [30] observed that the cyclic stress-strain

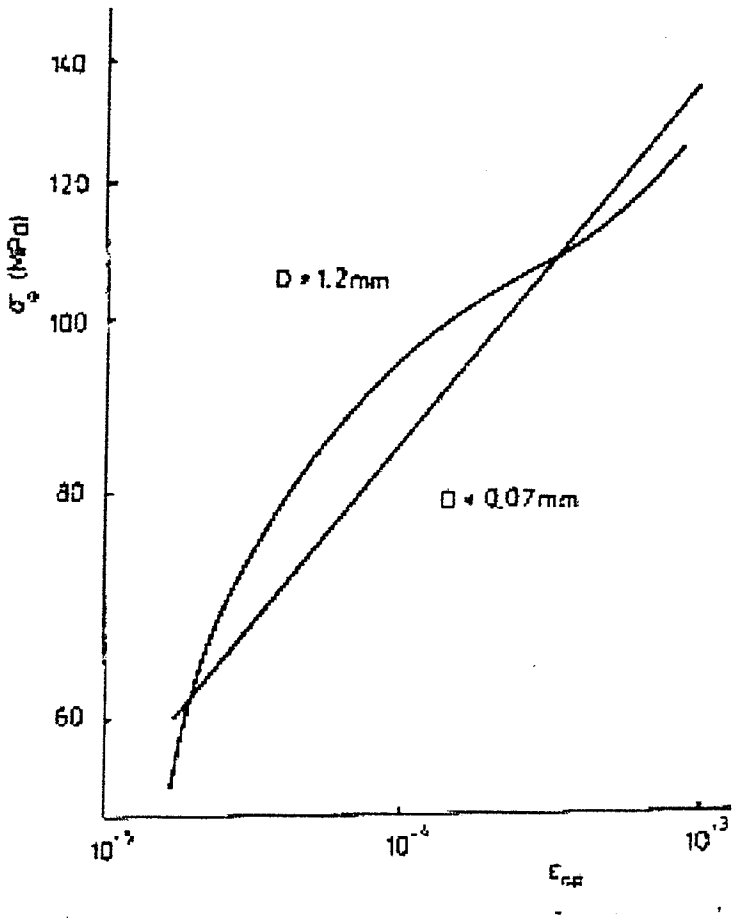

Figure 2.9 Cyclic stress-strain curve of polycrystalline copper for small grain size (0.07mm) and large grain size (1.2mm). [24]

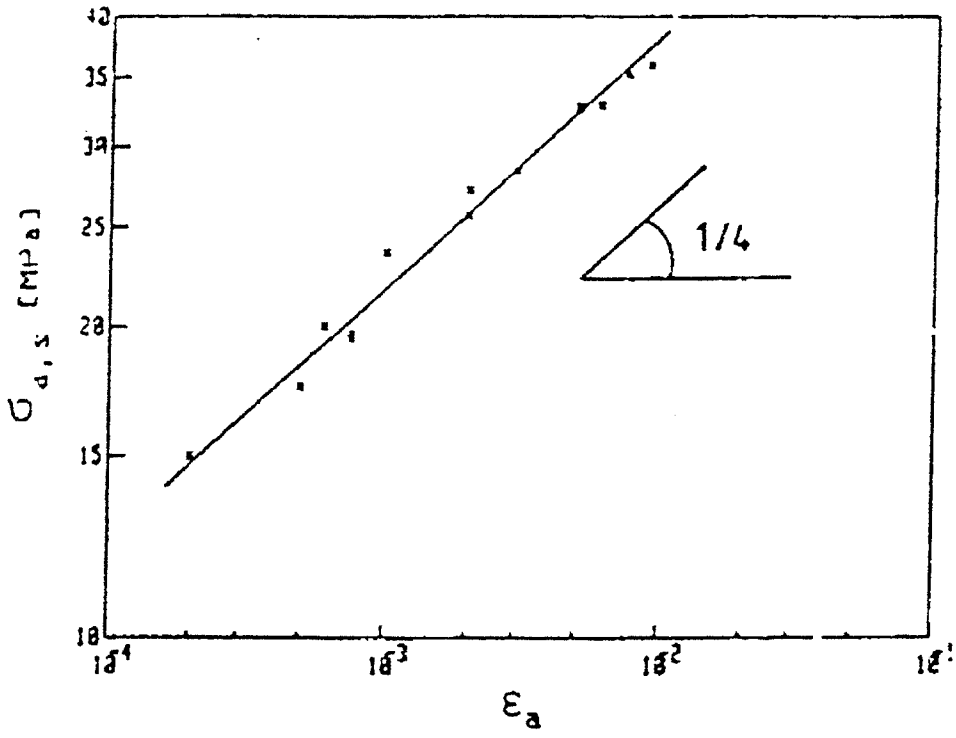

Figure 2.10 Cyclic stress-strain curve for 99.999% polycrystalline aluminium [25]

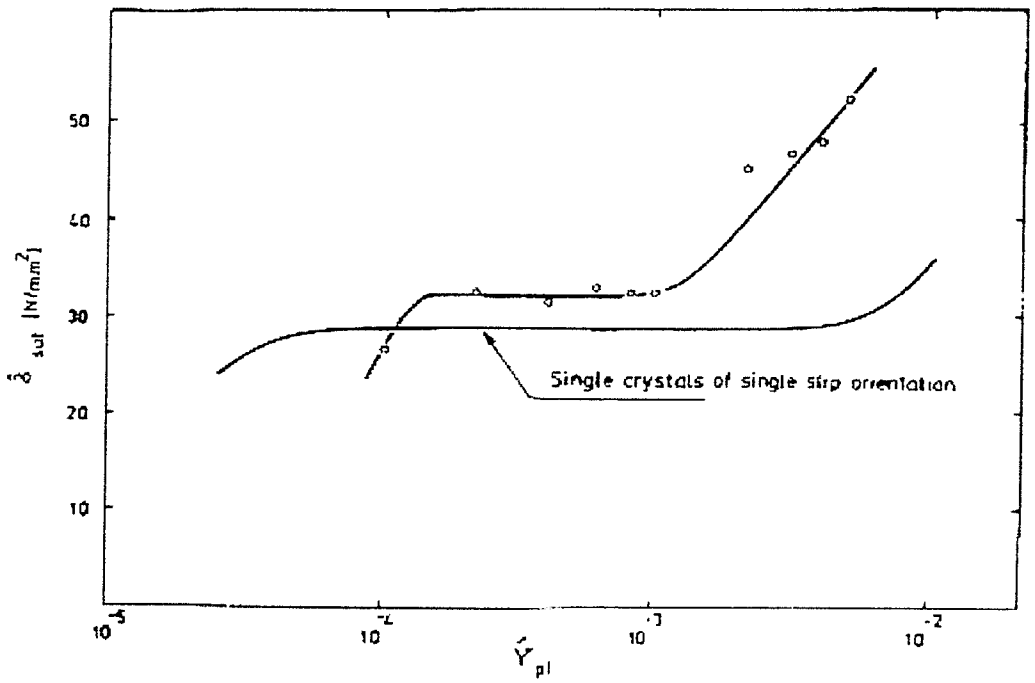

Figure 2.11 Cyclic stress-strain curve for polycrystalline copper of 2 mm grain size compared with the CSS curve for monocrystals [28]

(CSS) curve measured for polycrystals shows a "plateau" which reflects the plateau displayed by the single crystal CSS curve as shown in Figure 2.12. However Mughrabi [31] deduced that FCC polycrystals do not exhibit a plateau region in the CSS curve in strain-controlled tests as in the case of monocrystals as shown in Figure 2.13.

Bassim and Liu [1] performed cyclic tests on polycrystalline copper and concluded that the CSS curve is characterized with the occurrence of a quasi-plateau where a slight constant increase in stress is observed. Figure 2.14 shows CSS curve in polycrystalline copper.

2.5 CYCLIC DEFORMATION BEHAVIOR OF POLYCRYSTALLINE NICKEL

Since both nickel and copper have the face centered cubic crystal structure and have relatively high staking fault energies, one would expect the deformation characteristics to be similar. Morrison and Chopra [32], Polak et al [33] concluded that polycrystalline copper and nickel exhibit similar cyclic deformation behavior and demonstrated that similarities in the CSS behavior and evolution of dislocation structures exist.

Previous work by Mughrabi et al. [16] demonstrated that monocrystal CSS curves of nickel and copper are similar when shear stress is normalized with shear modulus as shown in Figure 2.15. Using this method, similarities in the polycrystalline copper results of Polak et al. [33] and nickel results of Morrison and Chopra [32] are shown in Figure 2.16 where the saturation stress amplitudes are normalized by dividing by Young's modulus. They argued that the divergence of the results at high plastic strain amplitude is due to the small grain size of the copper or differences in crystallographic texture. In addition, other previous work on single and polycrystalline nickel indicated that there are some similarities in the cyclic responses of nickel and copper [34,35]. Table 2.1 summarizes microstructural observations in polycrystalline nickel at different plastic strain amplitudes.

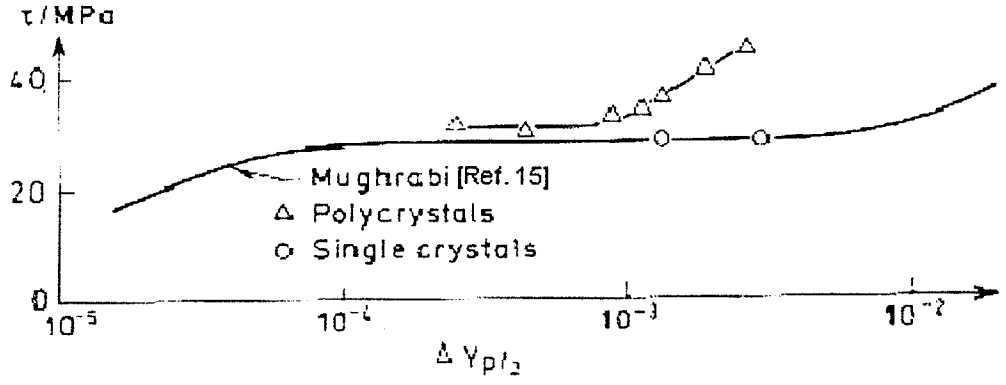

Figure 2.12 Cyclic stress-strain curve for copper single crystals and polycrystals [30]

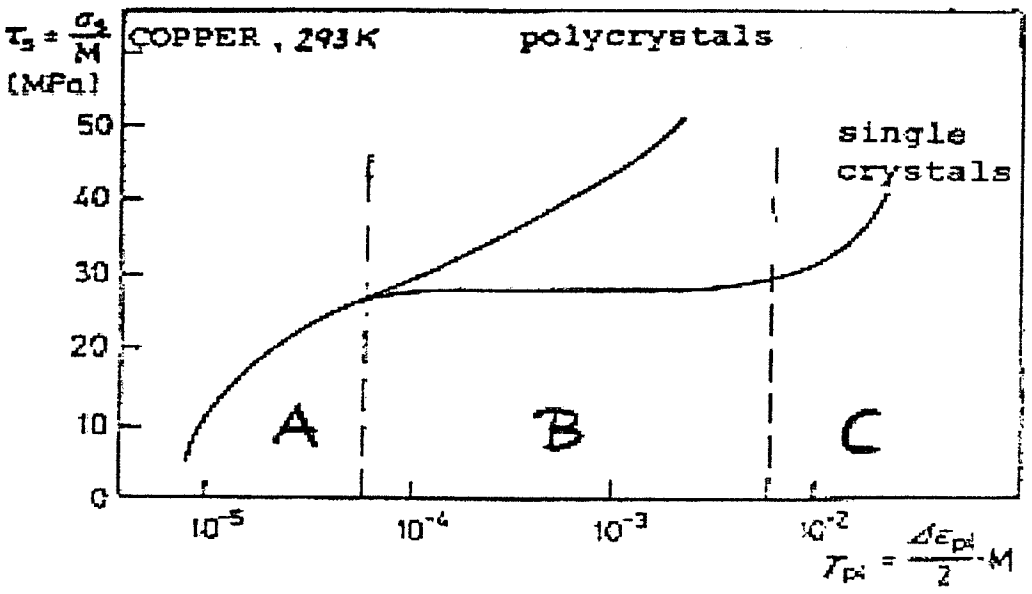

Figure 2.13 Cyclic stress-strain curve of fatigued copper mono- and polycrystals [31]

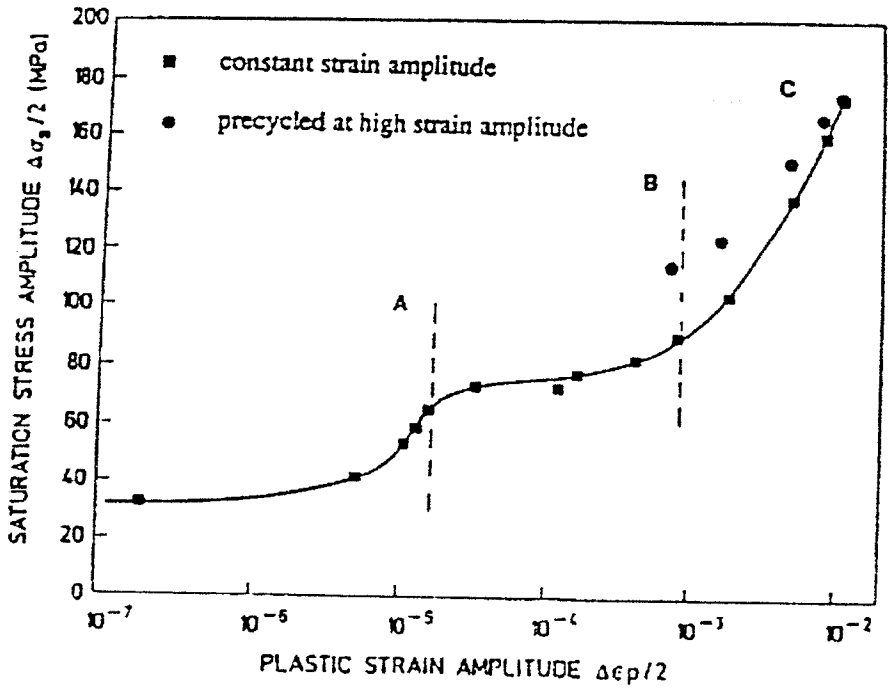

Figure 2.14 Cyclic stress-strain curve for polycrystalline copper [1]

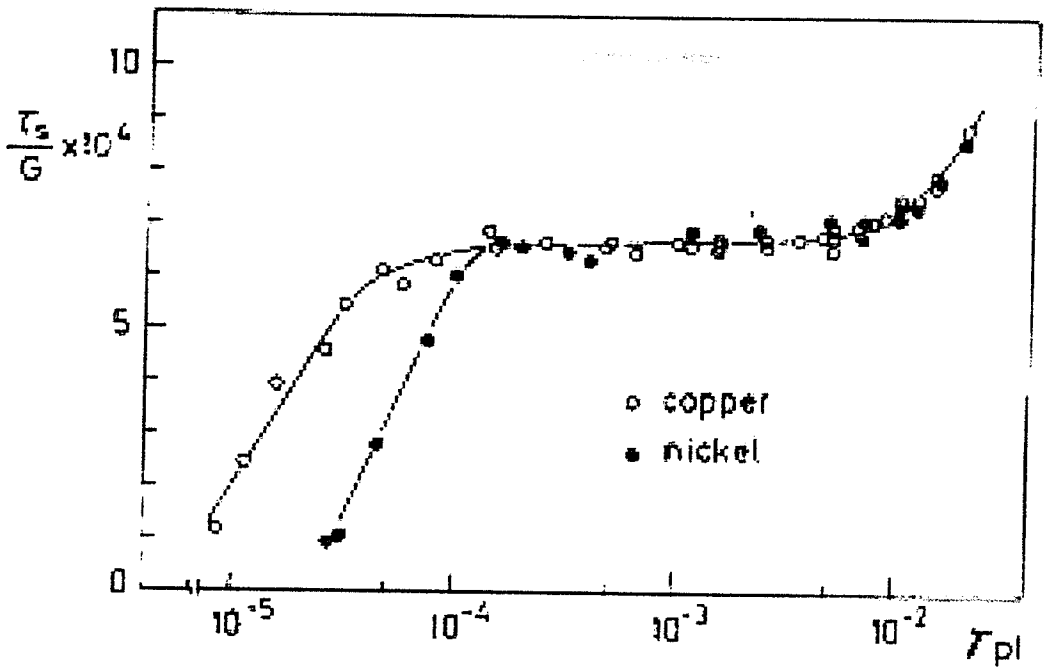

Figure 2.15 Cyclic stress-strain curves for copper and nickel single crystals in which the stress has been normalized against the shear modulus [13]

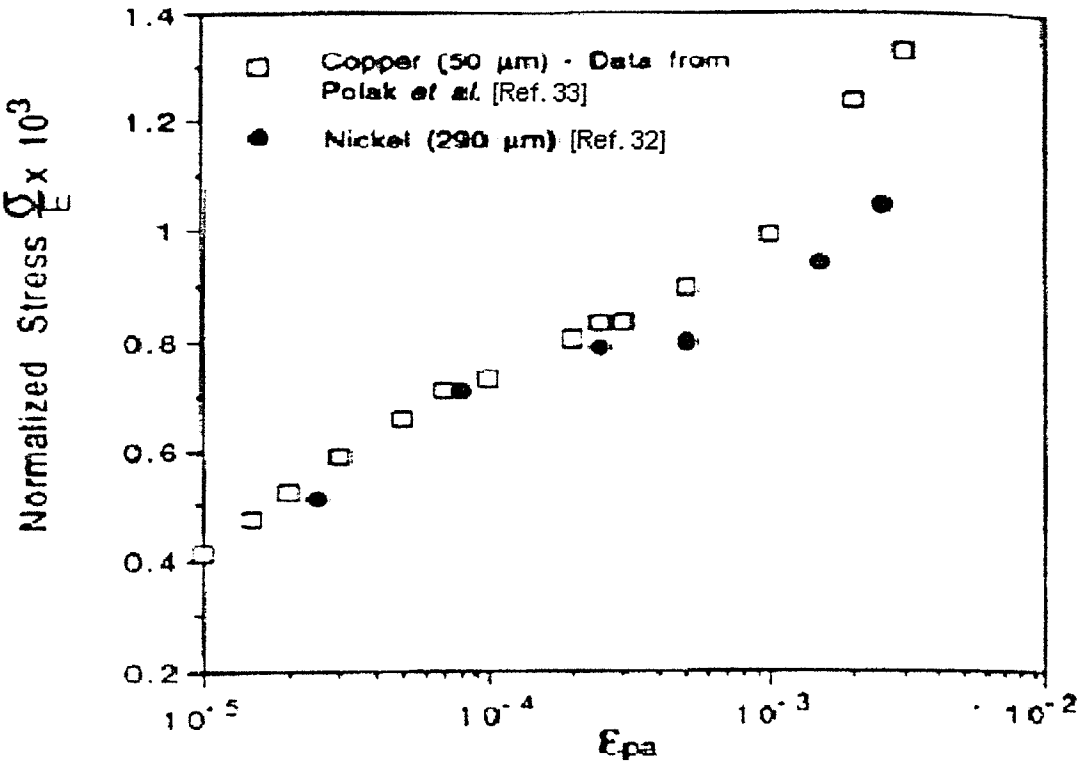

Figure 2.16 Cyclic stress-strain curve for polycrystalline copper and nickel [32]

Plastic Strain Amplitude	*Surface Observations*	*Transmission Electron Microscopy*
2.5×10^{-5}	few isolated slip bands	---
8.0×10^{-5}	Number of slip bands increased	Loop-patch / channel (vein)
2.5×10^{-4}	PSB macro-bands formed	Vein structure, PSBs
5.0×10^{-4}	Homogeneous thinner PSBs	Vein, PSBs, Labyrinth*, cell
5.0×10^{-4} and below	Predominate single slip Secondary slip systems	---
2.5×10^{-3}	Secondary slip systems Wavy appearance slip bands	Cell type of dislocation structure

* While the labyrinth structure was frequently seen in the fine-grain specimen cycled at 5.0×10^{-4}, this structure was not observed in coarse-grain nickel.

Table 2.1 Summary of microstructural observations on polycrystalline nickel

2.6 CYCLIC DEFORMATION BEHAVIOR OF POLYCRYSTALLINE ALUMINUM

Li et al. [36] conducted fully reversed strain-controlled push-pull tests on polycrystalline commercially pure aluminum and noted the absence of plateau region in the cyclic stress-strain curve as shown in Figure 2.17

Jo-Chi Tsou [37] studied the cyclic deformation behavior of pure polycrystalline aluminum over a range of strain amplitudes using conventional fatigue testing methods. Cyclic hardening response revealed a rapid increase in stress in the early stage of deformation and a gradual decreasing rate toward a steady state of stress amplitude response as shown in Figure 2.18. In addition, the cyclic stress strain curve shown in Figure 2.19 exhibited an increase in the saturated stress amplitude with increasing plastic strain amplitude. The increase in the stress was found to be faster at lower strain amplitude and became more gradual at higher strain amplitude, which has been observed for most FCC polycrystals.

The dominant surface slip character is the persistent slip band (PSB) structure, which could not be found within interior grains from TEM observations. The explanation of the existence of PSBs on the surface not in the interior could be the result of less grain boundary restriction on the slip activity near the surface and at those places, dislocation activity is closer to that of single-slip condition.

TEM observations revealed only the dislocation cell structure as the dominant deformation structure of deformed aluminum. It was observed that cell walls consist of large number of dislocation meshes and some edge dipoles near and within cell walls, which their thickness decreases with increasing strain amplitude. In addition, cells are more equiaxed at large strain amplitude fatigue.

Giese et al. [25] conducted fatigue study on coarse-grained (216 μm) polycrystalline aluminum tested at room temperature in tension-compression under total strain control conditions. They concluded that the dependence of the stress amplitude σ_a

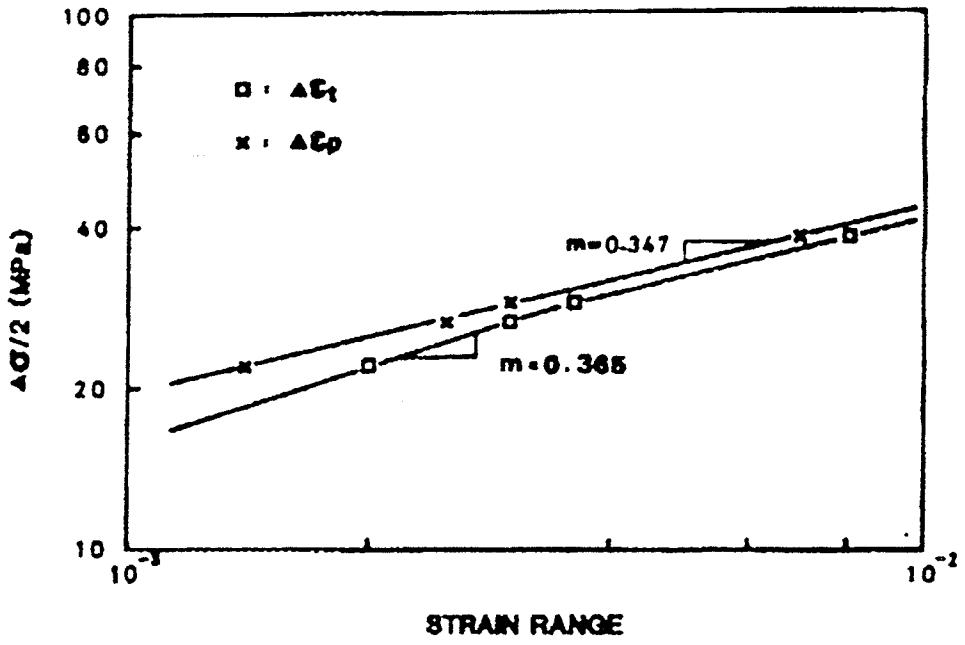

Figure 2.17 Cyclic stress-strain curve for polycrystalline aluminium 1199 [36]

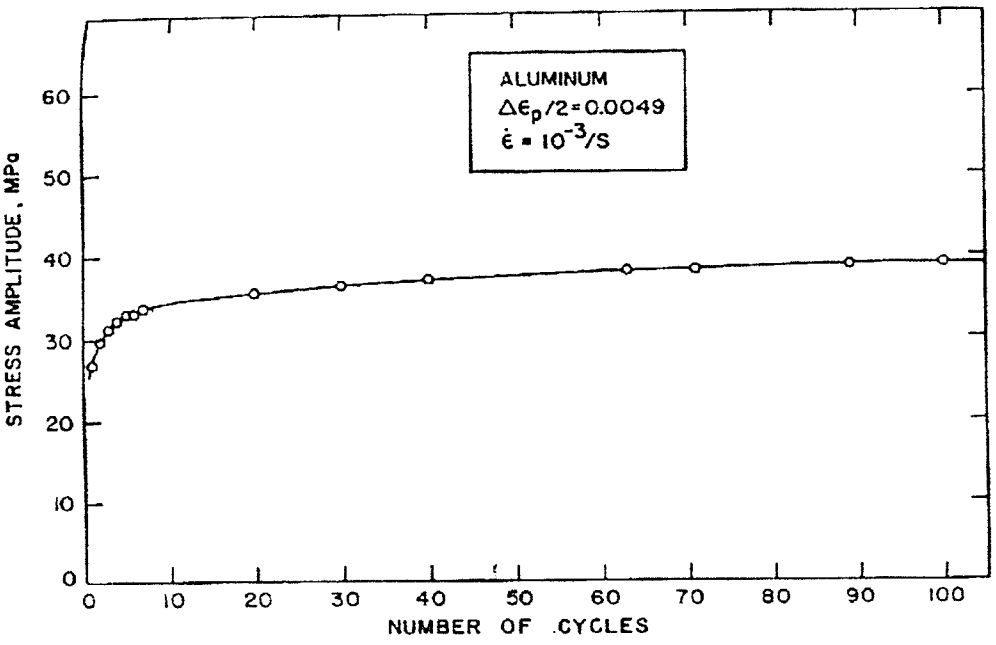

Figure 2.18 Cyclic hardening curve for polycrystalline aluminium [37]

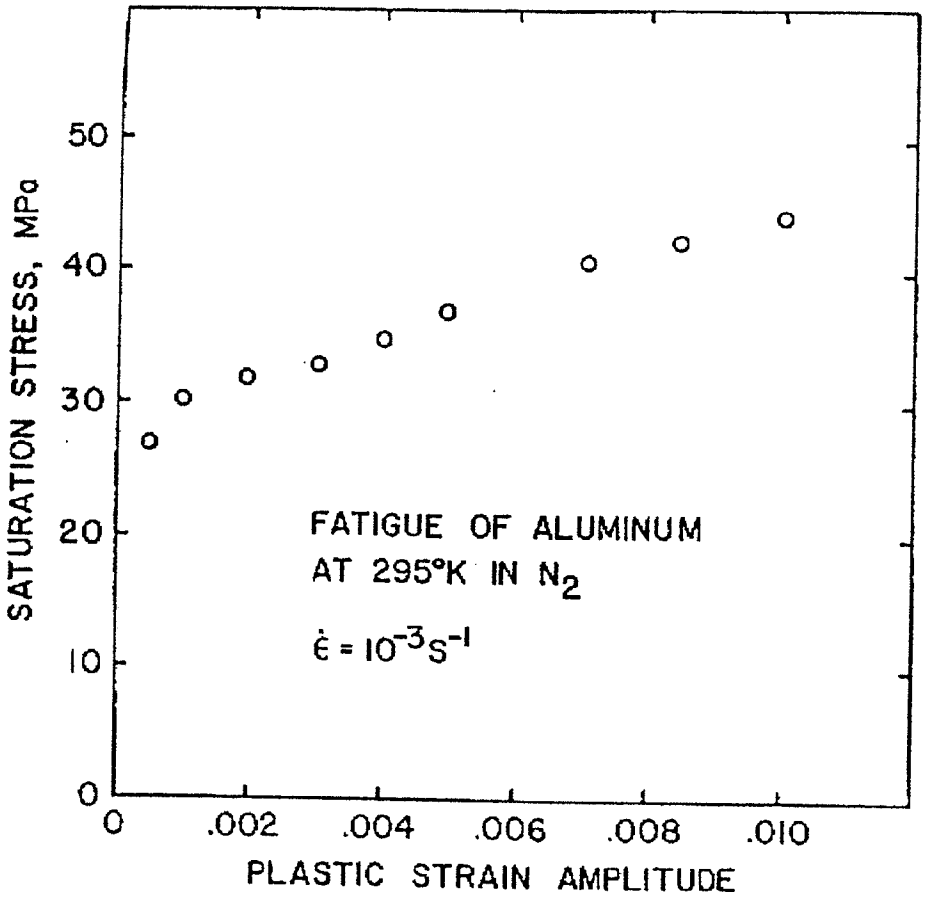

Figure 2.19 Cyclic stress-strain curve for polycrystalline aluminium [37]

on the cumulative strain ε_{cum} is determined by the plastic strain amplitude ε_a. At small amplitudes a softening stage has been found while at large cumulative strains the cyclic hardening curves exhibits a tendency to saturation. The dependence of the saturation stress $\sigma_{a,s}$ on ε_a has been shown to obey a simple power-law with the exponent n of ¼ as shown in Figure 2.10.

Guichon et al. [38] performed cyclic deformation studies on polycrystalline aluminum fatigued under total strain control conditions at room temperature. They concluded that as a consequence both of a high value of the staking fault energy and of high dislocation mobility at room temperature, a cellular structure of dislocations appears very soon, as early as the first cycle, in fatigued pure aluminum in all strain ranges. PSBs or labyrinth structures have not been observed even in the vicinity of the specimen surface. They explained that cell walls contribute to plastic deformation and the interface nature between cell walls and cell interiors is probably the contributing factor.

Another TEM study on polycrystalline aluminum fatigued at 77K by Charsley and Harris [39] revealed the presence of matrix structure consisting of dense irregular regions of dislocation loop patches with narrow irregular channels, which have a relatively low dislocation density. The dislocations, which cross the channels of the structure, have a single value of the Burgers vector and are close to a screw orientation.

2.7 CYCLIC DEFORMATION BEHAVIOR

Cyclic deformation behavior as depicted by the cyclic stress-strain curve of monocrystalline and polycrystalline metals and alloys depends strongly on history, microstructure, and test conditions. Such dependence would explain the different experimental results and conclusions reached by researchers. This section briefly summarizes previous findings on the study of low cycle fatigue of metals and alloys such as the effect of testing conditions, plastic strain amplitude, and grain structure on the cyclic deformation response.

2.7.1 Effect of Testing Conditions

Winter [18] and Marchand et al. [40] found that polycrystals tested at low strain rate exhibited a plateau in the CSS curve Although Figueroa et al [41] did not find a true plateau under constant strain control tests in copper, they observed a plateau in constant stress testing under cyclic loading.

Llanes and Laird [42] showed that the CSSC of copper polycrystals is sensitive to different values of peak stress during the ramp-loading process of initiating tests. The dependence of the CSSC on the peak stress decreases with increasing the plastic strain amplitude and is almost negligible for values higher than 4.0-5.0 x 10^{-4} as shown in Figure 2.20. Yan et al. [43,44] have also found that the cyclic deformation tends to be more strongly and more uniformly localized than in tests at constant amplitude, if the tests are initiated by the ramp-loading method used by Neumann [45]. In addition, Wang and Laird [46] reported a plateau, which occurred at a stress value of 98 MPa in polycrystalline copper tested in strain control if the specimens were previously ramped at stress levels above 64 MPa. They concluded that a plateau could be induced in the polycrystalline copper CSS curve by initiating the experiment under a ramp-loading condition that favored single slip and enhanced the formation of PSBs. Also Lukas et al. [47] have also concluded that ramp-loading appeared to have the strongest effect, resulting in higher degrees of strain localization leading to a plateau in the CSS curve.

2.7.2 Effect of Plastic Strain Amplitude

Polak et al. [33] studied cyclic deformation of polycrystalline copper of medium grain size (50 μm) and concluded that after the saturation or the achievement of local stress maximum, secondary hardening or appreciable secondary softening, depending on the applied plastic strain amplitude was present. Copper specimens cycled at plastic strain amplitudes below 7 x 10^{-4} experienced cyclic softening due to the localization of plastic strain in PSBs and the condensation of the existing dislocation structure. On the other

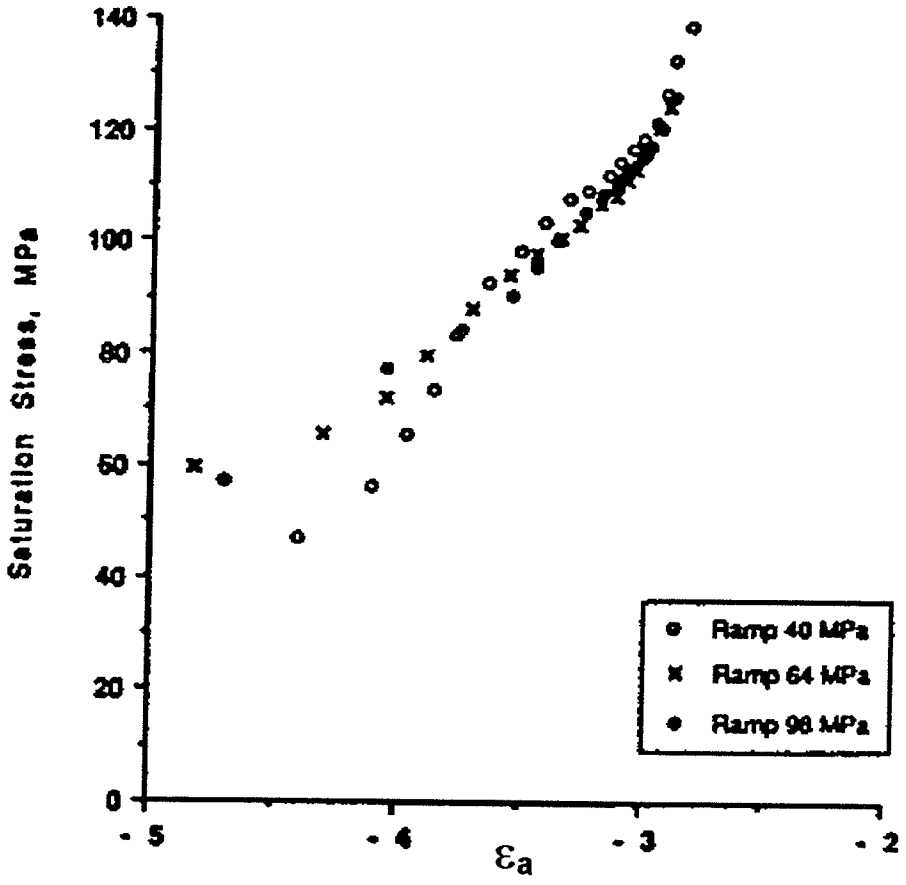

Figure 2.20 Effect of peak stress during ramp-loading initiation of a fatigue test on the cyclic stress-strain curve of polycrystalline copper [42]

hand, secondary hardening has been reported in polycrystalline copper cycled at plastic strain amplitudes above approximately 7×10^{-4}.

C.D. Liu and M.N. Bassim [48] found that polycrystalline copper tested in fatigue at incremental strain amplitudes displays sequential strain hardening behavior and had the same stress as at conventional constant strain amplitudes. However, when tested at decremental strain amplitudes, it displays a sequential strain softening and had a history effect on the stress as compared with that at conventional constant strain amplitudes. In addition, they concluded that the incremental loading produced a dislocation wall structure similar to that at constant amplitudes. Under the decremental loading, the cellular dislocation structure formed at higher strain amplitude reconverts to labyrinth structure. This degeneration process was found to be incomplete and the dislocation structure remained dense dipolar walls.

Guichon et al. [38] concluded that the lower strain amplitude and the cycle number are, the higher will be the microstructure heterogeneity. On the other hand, dislocation cell walls were observed better condensed with increasing strain amplitudes or cycle number.

2.7.3 Effect of Grain size

Grain size modifies the rate at which a polycrystal hardens to a degree that depends on whether dislocations are arranged in cells or in coplanar arrays, i.e. wavy or planar slip. Furthermore, the plastic strains over which grain size effects are important also depend on slip character

Johnston and Feltner [49] studied the effect of grain size on the strain hardening response of cyclically deformed polycrystalline copper and concluded that the influence of grain size on the plastic deformation can be explained in terms of strain compatibility, which constitutes the very foundation of grain boundary effects. The need to maintain continuity of plastic strain across grain boundaries between randomly oriented neighbors

demand that multiple slip systems or shear modes be brought into operation when the polycrystal as a whole is deformed. As the strain level increases, the number of different slip systems necessary to maintain continuity of strain increases. While strain compatibility induces the operation of many slip systems, the latter causes the rate of strain hardening to increase by the interaction between individual systems generating dislocation barriers, debris which affect the mobility and mean free path of dislocations in the interior of the grain.

Llanes [50] showed that Grain size effect on polycrystalline copper was more pronounced at low plastic strain amplitude and diminished at high plastic strain amplitude. In contrast, the study performed by Morrison [51] on Fine-grain (24μm) polycrystalline nickel reflects exactly the opposite behavior (from Llanes [50] study). A large difference in saturation stress at high plastic strain amplitude (i.e. fine-grain nickel saturates at higher stress amplitude than the coarse-grain nickel) was noted. A small difference or no difference in saturation stress at low plastic strain amplitude was noted as shown in Figure 2.21.

Morrison [51] concluded from his study on polycrystalline nickel that secondary hardening is more pronounced in the fine-grain material and is related to an increase in back stress. Whereas, no secondary hardening is evident in the coarse-grain nickel as shown in Figure 2.22.

Mughrabi et al. [26] reported that grain size also influences the slip character of the material and it has been shown that the onset of multiple slips occurs at lower plastic strain amplitudes in fine-grain than in coarse grain copper. Mughrabi and Wang [52] studied the cyclic stress-strain response of polycrystalline copper with grain sizes ranging from 25 μm to 400 μm and found that grain size had very little effect on cyclic stress-strain response.

Polak et al [33], Wang and Mughrabi [53], Kuokkala and Kettunen [22] studied cyclic deformation of fine-grain and coarse-grain copper. They found that secondary

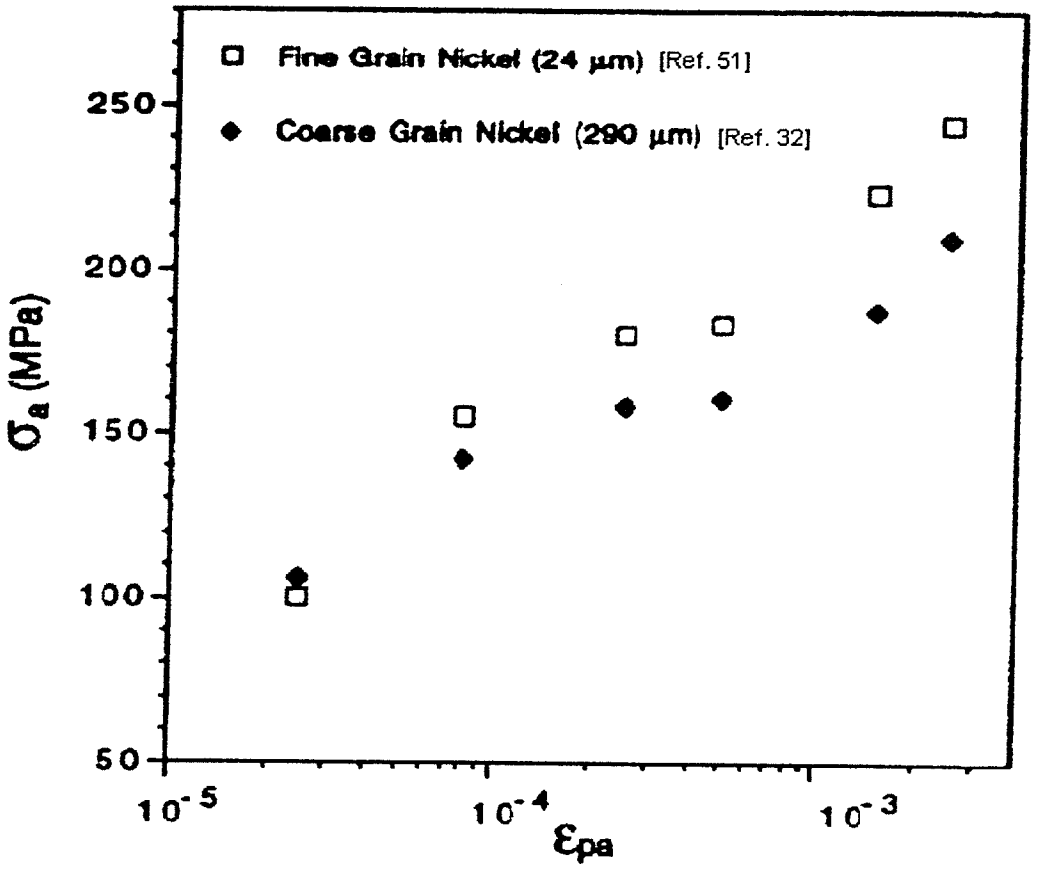

Figure 2.21 Cyclic Stress strain curve for polycrystalline nickel comparing cyclic deformation behaviour between fine-grained and coarse-grained nickel [51]

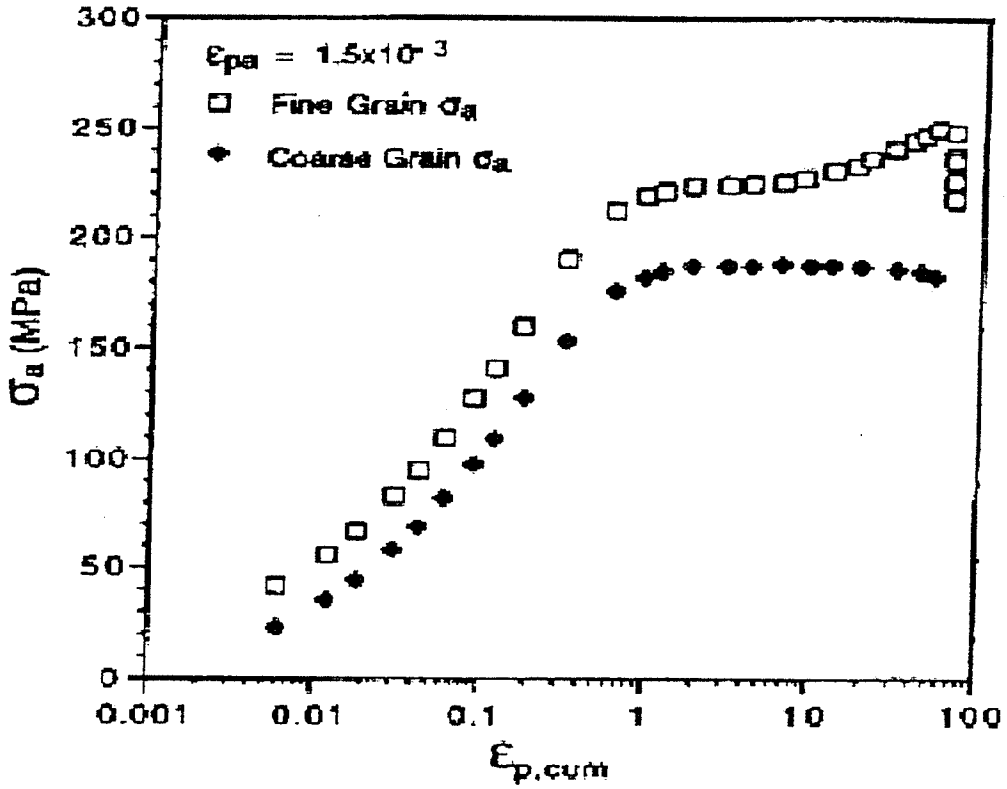

Figure 2.22 Cyclic hardening curve of both coarse-grained and fine-grained polycrystalline nickel cycled at plastic strain amplitude of 1.5 x 10^{-3} [51]

hardening was reported in fine-grain copper cycled at plastic strain amplitude of 7×10^{-4} but not in coarse-grain copper cycled at plastic strain amplitude of 4×10^{-3}. They concluded that secondary hardening occurs at lower plastic strain amplitudes and earlier in the fatigue test in polycrystalline than in monocrystalline copper because of the greater tendency for multiple slip in polycrystals. The occurrence of secondary hardening is related to the activation of secondary slip systems and the formation of a dislocation cell structure with increasing misorientations.

Figueroa et al. [41] observed a plateau in the CSSC of fine-grained copper (grain size of 35 μm) cycled under load control. Rasmussen and Perdersen [20] found an insignificant plateau in coarse-grained copper (grain size of 150μm) cycled under plastic strain control. Kuokkala et al. [54] reported an extensive plateau (extending over almost one order of the plastic strain) in very coarse-grained copper (grain size of 2mm) cycled under conditions of controlled plastic strain.

Lukas and Kunz [24] have shown that a large grain size in copper gives a higher flow stress than does small-gained copper and changes the shape of CSSC. As shown in Figure 2.23 and Figure 2.24, there is no plateau in fine-grained copper but there is a bulge in coarse-grained copper. The plateau in single crystals and the bulge in coarse-grained polycrystals both correspond to the continuous increase in the volume occupied by the PSBs. Lukas and Kunz [55] also found that at low strain amplitude, the saturation stress of copper increased as grain size increased. However, at higher strain amplitudes the fine grain copper exhibited a slightly higher saturation stress

Horibe et al. [56] found that coarse grain age-hardened Al-4%Cu alloy exhibited a higher saturation stress than fine grain material. CSSC has been found to vary systematically with grain size, finally showing a plateau with essentially zero slope when the grain size exceeds 1mm. In addition, Tiainen and Kettunen [28] have reported a proper "horizontal" plateau in polycrystalline copper extending over the range of longitudinal strain amplitudes from 5×10^{-5} to 3×10^{-4}, where the grain size was roughly 2mm.

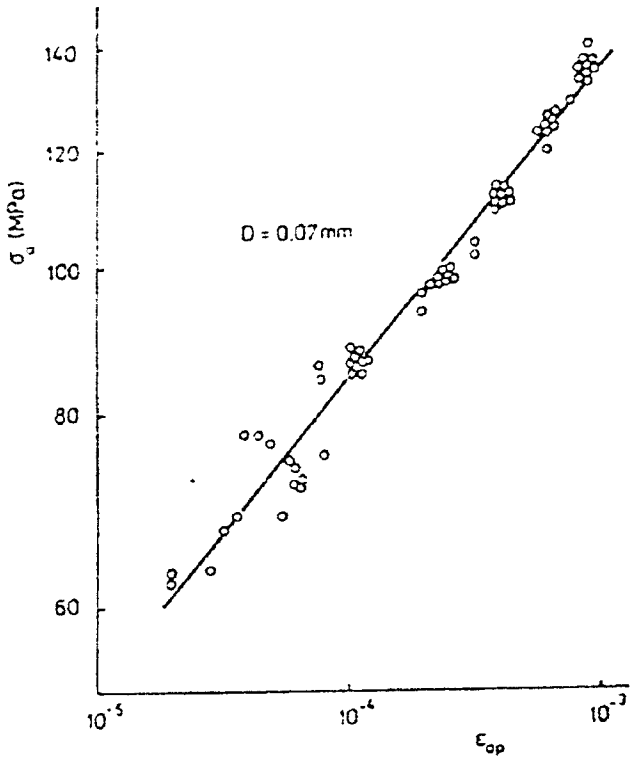

Figure 2.23 Cyclic stress-strain curve for fine-grained polycrystalline copper [24]

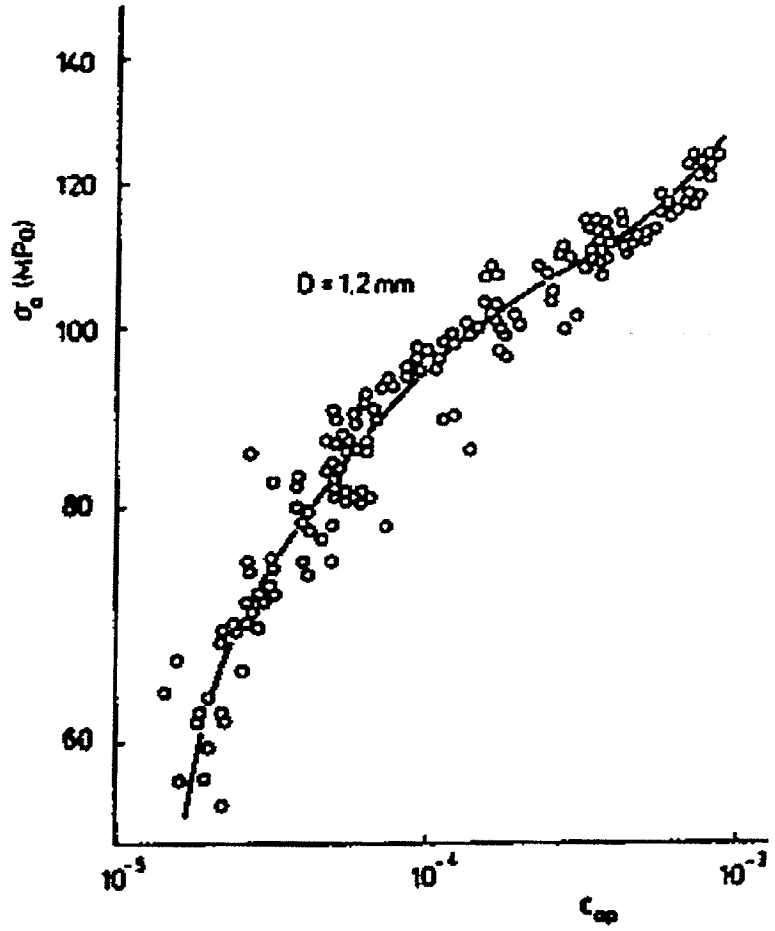

Figure 2.24 Cyclic stress-strain curve for coarse-grained polycrystalline copper [24]

Llanes and Laird [42] reported that the grain size has a significant effect on the cyclic stress-strain response of polycrystalline copper in the low amplitude regime. The saturation stress depends on the grain size in the range of plastic strain amplitude studied and there exists a "threshold", corresponding to a grain size of 85 μm, below which the grain size has no effect on the cyclic flow stress. They reported that the effect of grain size on saturation stress was the opposite to that predicted by a Hall-Petch type of argument which is a reduction of grain size cause a decrease in the cyclic saturation stress (i.e. coarse-grain copper had a higher saturation stress than fine-grain copper).

Morrison, Chopra and Jones [57] reported the opposite effect in polycrystalline nickel-270. They concluded that grain refinement reduces the degree of bulk cyclic strain localization in PSBs and increases fatigue life. (i.e. fine grain nickel exhibited a higher cyclic saturation stress than coarse grain nickel).

Boettner, Laird and McEvily [58] reported from their studies that at high strain amplitudes and for materials in which cross-slip is easy, sensitivity of the fatigue life to grain size exists. On the other hand, Thompson and Backofen [59] concluded that at somewhat lower amplitudes, the fatigue behavior appears to be insensitive to the grain size

2.7.4 Secondary Cyclic Hardening and the Role of grain boundary

The secondary hardening behavior is dependent on microstructural changes taking place during cyclic loading, such as the activation of secondary slip systems and the formation of a dislocation cell structure with increasing disorientation and decreasing cell sizes. In cyclic deformation, the build-up of constraint stresses between adjacent grains, the dislocation pile-ups, and PSB impingement against grain boundaries will activate secondary slip systems to operation and increase the resistance to dislocation motion. As a result, grain boundaries will promote an early occurrence of secondary hardening and enhance the strength.

Xia et al. [60] found that secondary hardening is observable in a certain range of strain amplitudes, which depends on the grain size of the specimen. Xia et al. and Wang et al [61-63] studied the secondary cyclic hardening in coarse-grained aluminum polycrystals and claimed that the strain incompatibility at gain boundaries made an important contribution to secondary cyclic hardening

2.8 CONFIGURATION AND EVOLUTION OF DISLOCATION STRUCTURES

Dislocation structures produced by cyclic strain deformation have been examined in a number of metals by transmission electron microscopy. These studies have produced a variety of interesting and often seemingly conflicting results. For example, different investigators have reported such structural features as cells [64, 65], bands of tangled dislocations [64, 66], dense patches or clusters of prismatic dislocation loops [67,68], planar arrays [64, 69], and various combinations or mixtures of these different structures.

Mughrabi [31,70,71] and Laird et al. [72] conducted TEM analysis on face-centered cubic metals, particularly Cu and Ni fatigued at room temperature and revealed the formation of a matrix structure at low fatigue amplitudes which is replaced, either wholly or partially, by a more compact or "condensed" dislocation structure at larger values of cumulative plastic strain. In addition, they observed a 'ladder structures' formed from primary dislocation dipoles, which are stacked in walls perpendicular to their Burgers vectors. In multiple slip orientations a common feature is the formation of walls on 2 sets of {100} planes – the so-called labyrinth structure.

Liu et al. [19] studied the evolution of dislocation structures in fatigued polycrystalline copper and correlated such evolution to the cyclic deformation behavior as depicted by the cyclic stress-strain curve. They concluded that the dislocation structures are arranged into three types of dipolized dislocation configurations, which correspond to the three regions in the cyclic stress strain curve. All three types of dislocation structures contain rather free dislocation channels, which are terminated by loop patches or ladders in PSBs or walls regardless of their contribution to the strain hardening.

Another study by Liu and Bassim [73] reveled that the dislocation structures can be viewed as form of dipolar structure irrespective of the difference in their appearance such as loop patch, PSB, labyrinth and dipolar wall. They explained that the differences between the dislocation structures are due to being compressed at different levels with different spacings. They concluded that the saturated stress is linearly related to the inverse spacing between the dislocation walls as shown in Figure 2.25.

2.8.1 Two-Phase Structure

Intense studies of the dislocation structures in copper single crystals lead to the proposal of a simple model of the behavior of the PSBs in single crystals as a bulk feature (winter [18]). The model considers the fatigue properties of copper as being correlated with a two-phase system, the two phases being the inactive matrix structure and the active PSB structure. Therefore the model is called the two-phase model, and it originates from the observation that the relative amount of PSBs increases with increasing plastic strain amplitude. So the fatigue crystal seems to adjust the relative amounts of the active and inactive phases to accommodate the applied strain amplitude.

Woods (10) reported that the dislocation microstructure in copper single crystal contains two phases, the relative abundances of which depend on the strain amplitude. At low amplitudes, the 'uncondensed phase', contains irregular clumps and veins of dislocations separated by relatively undislocated material. At higher plastic strain amplitudes (0.3%) the 'condensed phase' known as the 'wall structure' contains a three-dimensional array of regularly spaced dislocation wall perpendicular to the primary slip direction. It has been found that the 'uncondensed phase', or in Winter's notation the 'matrix', is associated with the inactive parts of the specimen between the persistent slip bands and is presumably intrinsically stronger that the wall structure. A typical two-phase dislocation structure is shown in Figure 2.26.

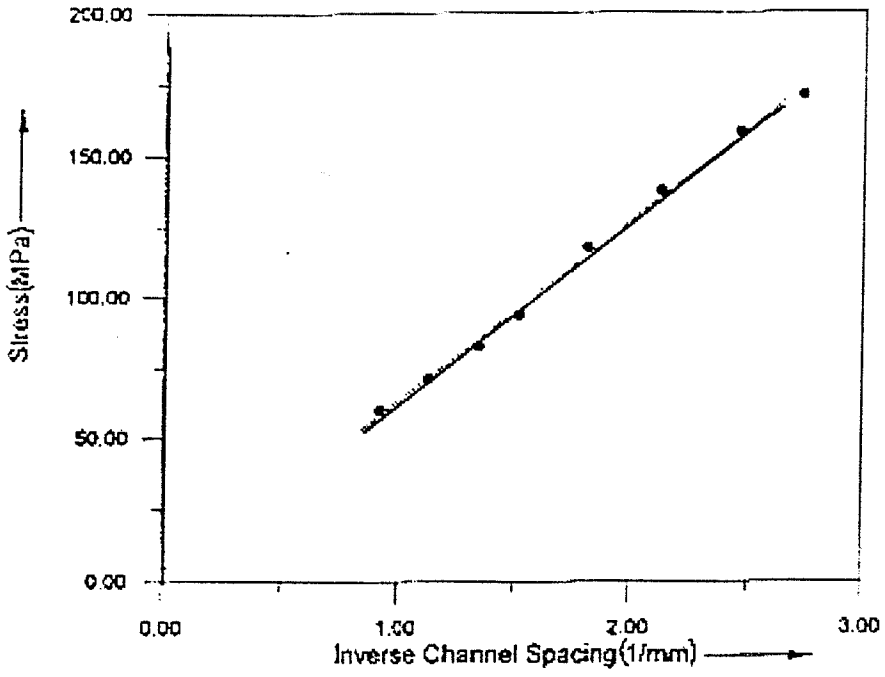

Figure 2.25 Relationship between dislocation structure and saturated stress for cycled polycrystalline copper [73]

Figure 2.26 PSBs and matrix veins constituting a two-phase structure [74]

2.8.2 Loop Patch Structure

Liu and Bassim [75] studied the configuration of saturated dislocation loop patch structures in polycrystalline copper fatigued at low strain amplitudes and revealed that three types of low-energy dislocation patch structures were observed as follows:

2.8.2.1 Cylindrical Loop Patches

Cylindrically shaped loop patches (Figure 2.27) consist of dipolar debris with a primary Burgers vector. This type of loop patch is constructed from the deposition of edge dipolar debris in the process of sweeping screw dislocations in the free-dislocation channels. An example of edge dipolar debris in the free-dislocation channel is shown in Figure 2.28.

2.8.2.2 Irregular Loop Patches

Irregular loop patches (Figure 2.29) are predominated by two kinds of dislocation and are developed mainly from the staking of their dipolar debris and loops. The irregular loop patches are found in the grains oriented with double slip.

2.8.2.3 Cellular Loop Patches

Cellular loop patches (Figure 2.30) contain four types of dislocations; three of them have dipolar debris and loops. It is believed that the cellular loop patches are formed in grains oriented for multislip.

In addition to the three types of loop patch structure, cubic sessile dislocations are formed to coexist with the irregular loop patches and the cellular loop patches in polycrystalline copper at low strain amplitude of 1.2×10^{-5}. The cubic sessile dislocations are formed from the reaction between edge dislocations and screw dislocations, which are perpendicular to each other.

Figure 2.27 Cylindrically-shaped loop patches in polycrystalline copper [75]

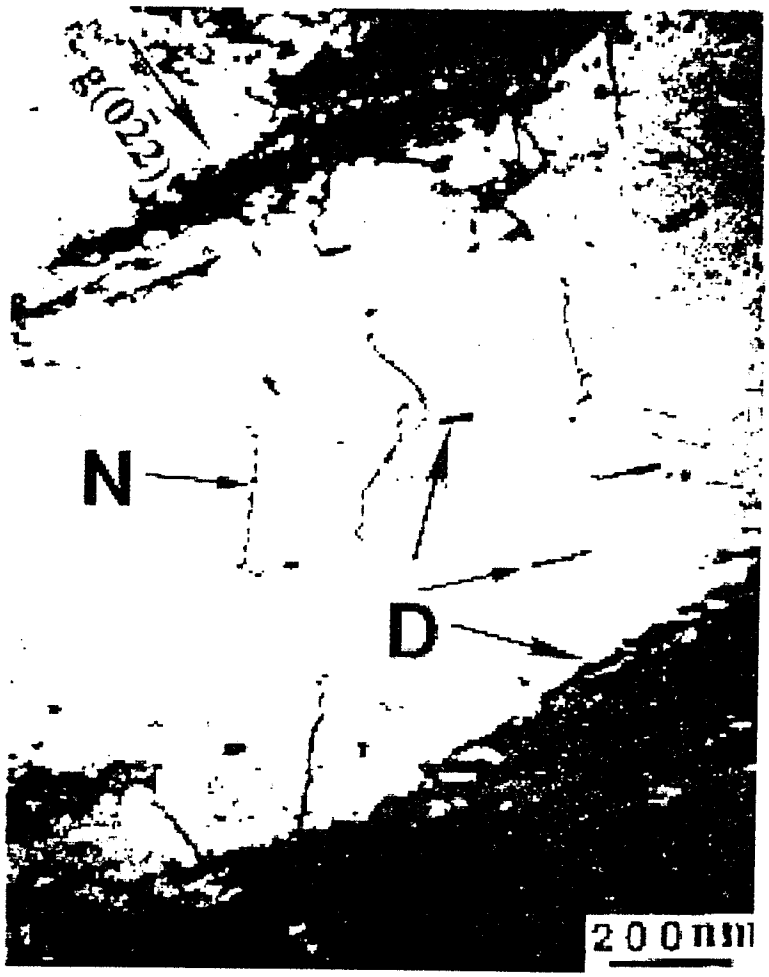

Figure 2.28 Dislocation clusters stacked by dislocation "debris" of dislocation dipoles – marked by "D". "N" is separated dislocation anchored by point defect [19]

Figure 2.29 Irregular loop patches in polycrystalline copper [75]

Figure 2.30 Cellular loop patches in polycrystalline copper [75]

2.8.3 Persistent Slip Bands (PSBs)

Persistent slip bands are the most prominent feature developed during cycling loading. They mark the onset of plateau region in the cyclic stress-strain curve and they are considered the sites for crack initiation. This name originated from the fact that during fatigue studies, certain grains with the "softest" orientation for plastic deformation formed intense bands, which "persisted" when a thin layer of the surface was removed by electro-polishing. Mughrabi [2,15] defines PSBs as highly localized soft thin lamellae of high slip activity located parallel to the primary slip plane. Liu et al [17] define PSBs on the polycrystals as short and straight thin lines that are found to be restricted within the grains and cover a very small area. As explained by Wang and Mughrabi [53] PSBs do not always maintain constancy of structure. If fatigue failure is delayed by cycling in vacuum, then the dipolar walls eventually transform to cells by "secondary hardening".

Such persistent slip band structures have recently been discovered in polycrystalline copper under low strain amplitude fatigue. At such low plastic strain amplitude fatigue deformation is inhomogeneous, and as result of this non-uniform deformation, some grains may be deformed in single slip condition. Since single slip is the requirement of forming persistent slip band structure (PSB), PSB could be found in those grains. For larger strain amplitude fatigue of polycrystalline metals, multiple slip may occur in the early stage of deformation which would suppress the formation of PSBs. [20] As a result, cyclic deformation of polycrystalline metals at medium to large strain amplitude should result in formation of cell structure.

In the 60s vast studies of dislocation structures in fatigued copper were performed. Basinski et al. [11] investigated the development of dislocation arrangements during the early stages of cyclic hardening of copper single crystals. They revealed the formation of a 3D network of interconnected veins packed tightly with mainly primary edge dislocations in dense multipole configuration, separated by dislocation-poor regions as shown in Figure 2.31. This structure, called the matrix structure, is a metastable structure and a local breakdown occurs after the veins have hardened to a critical extent

at which they can no longer accommodate the imposed plastic strain amplitude. The veins condense into a so-called wall structure, which appears as a characteristic ladder-like structure viewed in a (121)-section. This is illustrated in Figure 2.32

2.8.3.1 Persistent Slip Band formation and Plateau region

Finney and Laird [13] and Winter [18] found that in the regime of the plateau, loop patch structures and PSB structure coexist and the flow stress of the PSBs is a little softer than that of the loop patch structures. Consequently the strain is highly localized in the PSBs. The volume fraction of PSBs increases when more overall strain is called for by application of higher strain amplitude to the specimen. Throughout the plateau, the PSB structure consists of dipolar walls dominated by primary dislocations. Since this structure is reasonably constant, differing only in the height of the dipolar walls as the strain amplitude is increased, the flow stress is approximately constant, at least until the whole gage length is occupied by dipolar walls. At still higher strains, increasing activity on secondary slip systems produces the well-known fatigue cell structure in which wall misorientations are negligible, and the plateau give way to increased hardening.

The localization of plastic strain in persistent slip bands causes pronounced changes in the shape of the hysteresis loop. Such strain localization in PSBs would lead to more parallelogram-shaped hysteresis loop, which causes an increase in loop shape parameter, V_H and decrease in hardening coefficient, H. [15,76-78]

2.8.3.2 Dislocation Structure of Matrix and PSB

Both the matrix and the PSBs can be visualized as composite consisting of hard dislocation-rich component (matrix) and soft dislocation-poor component (PSBs) as shown in Figure 2.32. PSBs consist of low dislocation density channels separated uniformly by walls of edge dislocations forming a ladder-like structure, which occupy smaller volume fraction. On the other hand the matrix consists of a clustered bundles of veins separated by dislocation-poor channels.

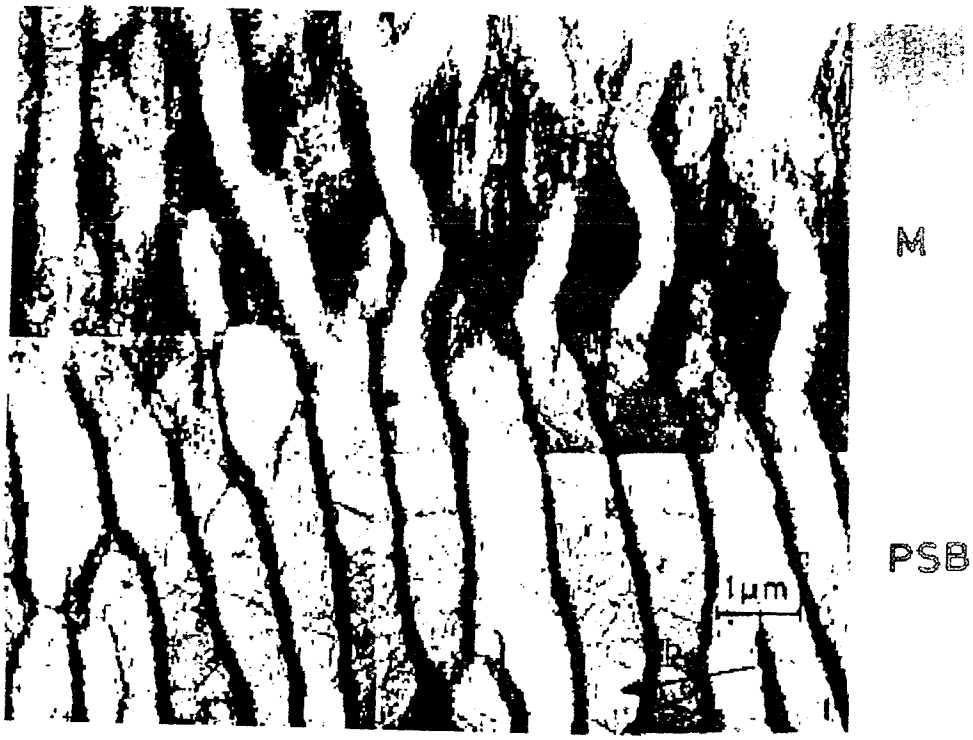

Figure 2.31 TEM micrograph of a copper single crystal. The vein structure has condensed into a wall structure. [16]

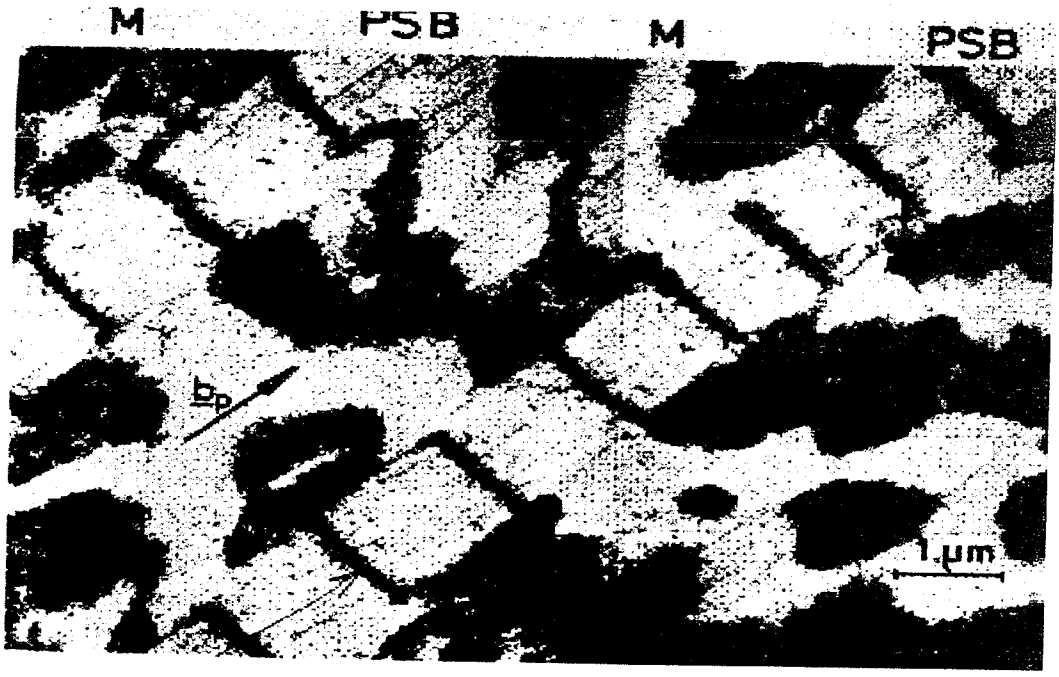

Figure 2.32 Wall structure appears as the characteristic ladder-like structure [16]

2.8.3.3 Dislocation Arrangements in Saturation

The dislocation structure of the PSB is significantly different from that of the matrix with its loop patches. It essentially consists of a cleared channel interrupted by rather thin-but dense- hedges of dislocations with an average wall-to-wall spacing of approximately 1.5 μm (characteristic of room-temperature deformation, at least at room temperature). [6]

The dislocation distributions in the matrix and in the PSBs are illustrated schematically in Figure 2.33 The edge-dislocation dipole loops form the dense veins in the matrix as shown in Figure 2.33a, whereas in the PSBs they form the wall or ladder structure as shown in Figure 2.33b. Because of the high local edge-dislocation densities, the veins and the walls are much harder than "channels" between them, which contain mainly screw dislocation in much lower density. Since the volume fraction occupied by the hard walls in the PSBs is much smaller than that occupy by the hard veins in the matrix, PSBs are relatively. soft with respect to the matrix. As a result, PSBs act like a soft layer sandwiched within a harder matrix. [2]

As shown in Figure 2.33 the dislocation arrangement in the PSBs is characterized by the following differences, which reflect the much larger strain localized in the PSBs with respect to that of the matrix [16]:

- The dense dislocation arrays occupy a smaller volume fraction.
- The density of free mobile screw dislocations is higher.
- Many short curved edge dislocation segments bowing out of the walls of the PSB structure indicates the existence of long-range internal stresses at these sites whereas there is no such evidence of internal stresses in the matrix.

As shown in Figure 2.34, dislocation segments in the center of the channels are much less strongly curved than those near the walls. At the wall/channel interfaces, there is an abundance of short strongly curved edge-dislocation segments bowing away from

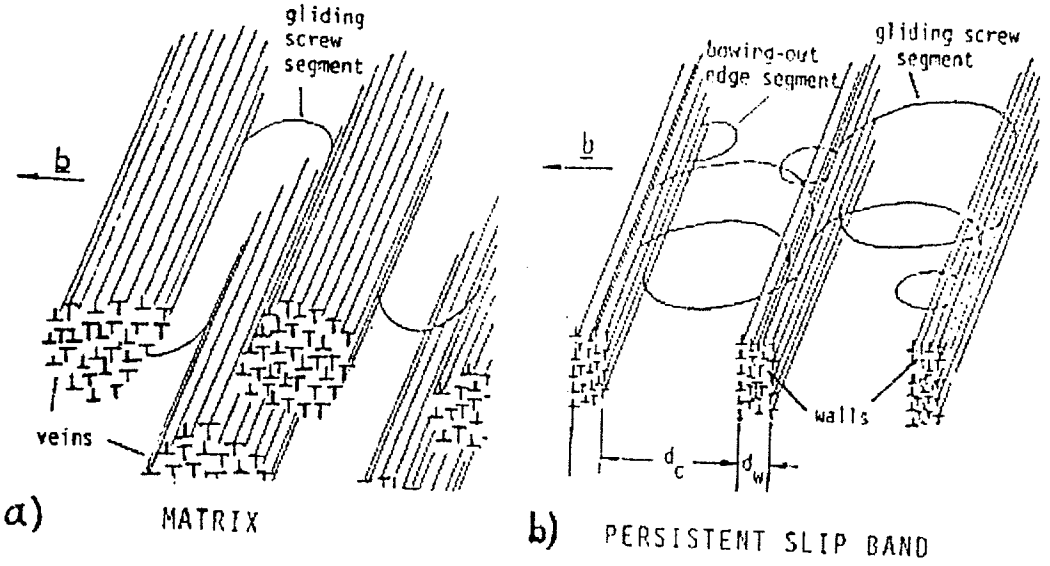

Figure 2.33 Schematic representation of the dislocation arrangements in a) a matrix structure and b) a persistent slip band [2]

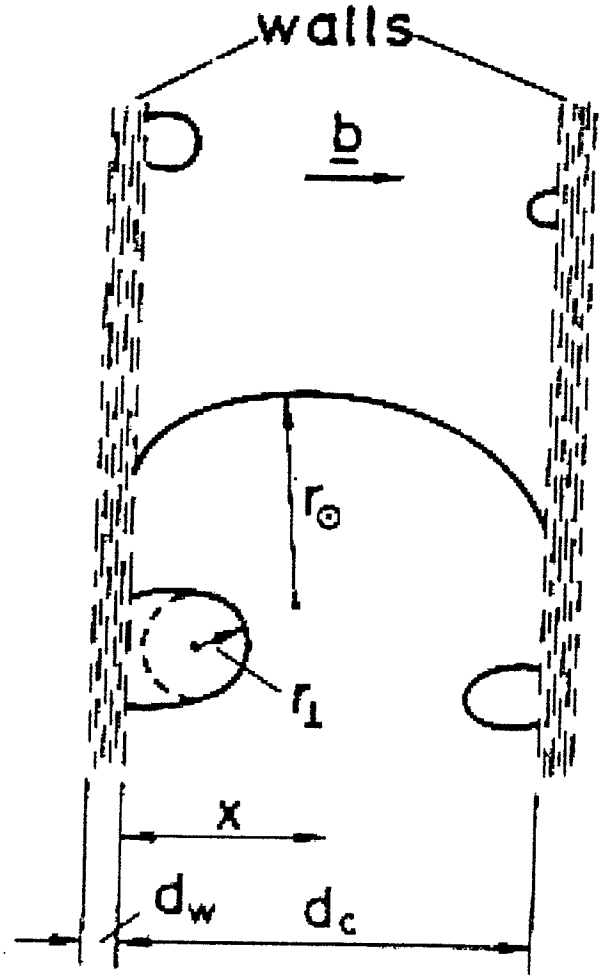

Figure 2.34 Schematic drawing of PSB walls showing bowed out edge and screw dislocation segments between walls [71]

the walls. The local stress is found to be as large as 70-80 MPa near the walls and only 15 MPa in the center of the channel. Figure 2.35 is a TEM micrograph of PSB dislocation wall-structure. The PSB-walls are clusters of narrow elongated dipolar primary edge-dislocation loops, corresponding to a high local dislocation density. The so-called channels between the walls contain a much lower dislocation density with predominant screw-character dislocations. It is clearly shown in this figure the screw segments bowing away from the walls across the channels.

2.8.4 Labyrinth Structure

A typical "labyrinth" configuration of the wall phase is shown in Figure 2.36. It has been assumed that the walls of the labyrinth structure can be of the {100}-type for nickel single crystals [34]. In addition, it has been found that walls are parallel to <100> with a spacing of 0.75μm as in the observation of Winter and coworkers on copper [79] and of Charsley on copper-nickel polycrystals [80]. In the labyrinth configuration, more than two Burgers vectors can be operative locally. Although this structure is apparently complex, its components pertaining to the wall phase has some analogy with the structure of PSBs.

2.8.5 Cellular Structure

The last stage in the evolution of dislocation structures in fatigue is the formation of cell structure. Cell structure formation is triggered by the onset of multiple glide when non-primary dislocations (i.e. secondary dislocations) are operative because the stress becomes large enough to start slip on non-primary systems. The cell structure constitutes a near-minimum energy configuration of the stored dislocation content. Figure 2.37 is a TEM photograph of dislocation cellular structure.

Figure 2.35 TEM micrograph of the wall structure of a persistent slip band [16]

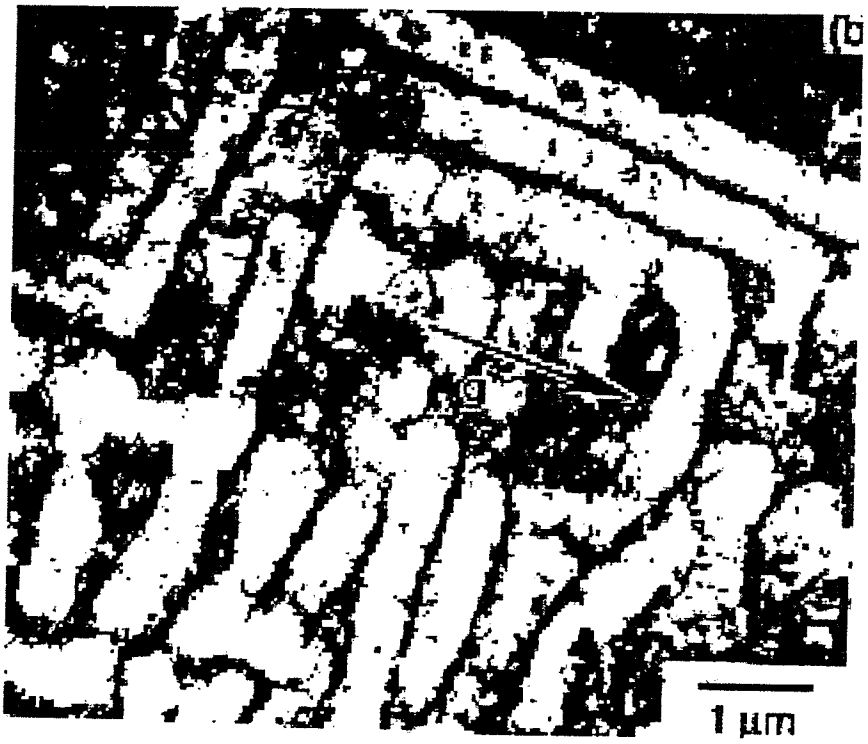

Figure 2.36 Typical labyrinth structure of the matrix phase [51]

Figure 2.37 TEM micrograph of closed cellular structure [19]

2.9 MECHANISM OF CYCLIC DEFORMATION

2.9.1 Mechanism of Steady-State Cyclic Deformation

The basic requirement of cyclic steady-state deformation is that the dislocation density does not change. This requirement is achieved by the absence of dislocation annihilation and multiplication or by a dynamic equilibrium between dislocation annihilation and multiplication. The vein structure in the matrix accommodates the small plastic strain by the flip-flop motion of existing dislocation dipoles until the saturation. Since in saturation neither multiplication nor annihilation of dislocations occurs in the vein structure a steady-state cyclic deformation is reached.

The wall structure in the PSBs undergoes continuous changes namely dislocation multiplication when the edge dislocation bow out of the walls and become entangled in neighboring walls and dislocation annihilation when the edge dislocations that are newly formed in the wake of moving screw dislocations are incorporated into the walls. As the result of the dynamic equilibrium between dislocation multiplication and annihilation a localized dislocation activity exists in the PSBs at which state the steady-state cyclic deformation is reached.

Steady state is maintained by an equilibrium between dislocation multiplication and annihilation of (edge and screw) dislocations, not only in the channels but also in the walls. Because of compatibility requirements, there must be a constant dislocation flux through the channels and the walls in the fully plastic state.

2.9.2 Mechanism of dislocation behavior in the dipolar wall structure

Typical dipolar wall structure is shown in Figure 2.38. It is agreed by Mughrabi et al. [14] that screw dislocations carry the bulk of the strain in the PSBs. Kuhlmann-Wilsdorf and Laird [81] imagined screw dislocations as gliding down the channels between the dipolar walls, usually in coordinated fashion between adjacent channel, and interacting with walls by laying down edge dislocations. Finney and Laird [13]

suggested that the screw dislocations are formed by the bowing of edge dislocations out of the walls and their gliding across the channel to the opposite wall, where the edge component becomes trapped by the dipolar wall and the screw dislocations are released to glide down the channel until they encounter screw dislocations of opposite sign which can mutually annihilate by cross slip. If screw dislocations are annihilated, it is necessary, as Mughrabi and coworkers [16] have pointed out, also to annihilate the edge dislocations trapped in the walls. Such annihilation could occur only by climb and would produce point defects, especially vacancies. Figure 2.39 is a TEM micrographs showing the presence of primary and secondary screw dislocations bowing out and gliding down across the channels between the dipolar walls.

2.9.3 Stacking-Fault Energy and Cross Slip

Materials response to cyclic deformation can be classified as wavy slip or planar slip, which is related to the ease with which dislocations cross-slip [82,83]. Materials with high SFE such as Al, Ni, Cu and Fe [82] are wavy slip materials, which have been shown to exhibit unique cyclic stress-strain behavior. Materials with low SFE, because the cross-slipping of screw dislocations is suppressed show more planar slip and history dependent stress-strain behavior, such as Cu-7.5%Al [83].

The stacking-fault energy (SFE) of the material has a large effect on the deformation substructures of cyclically strained materials and hence on the cyclic stress-strain behavior. Depending on the stacking fault energy as it relates to the ease of cross-slip of dislocations, materials with high stacking fault energy (SFE) tend to exhibit dislocations arranged in tangles or equiaxed cells those with low SFE tend to exhibit deformation substructures characterized by two-dimensional banded, linear arrays of dislocations such as persistent slip band (PSB).

In low-SFE metals cross-slip is more difficult to form because the dislocations have to constrict in order to change slip planes. Therefore, the dislocations arrange themselves into parallel bands such as PSB. On the other hand the metals with high SFE

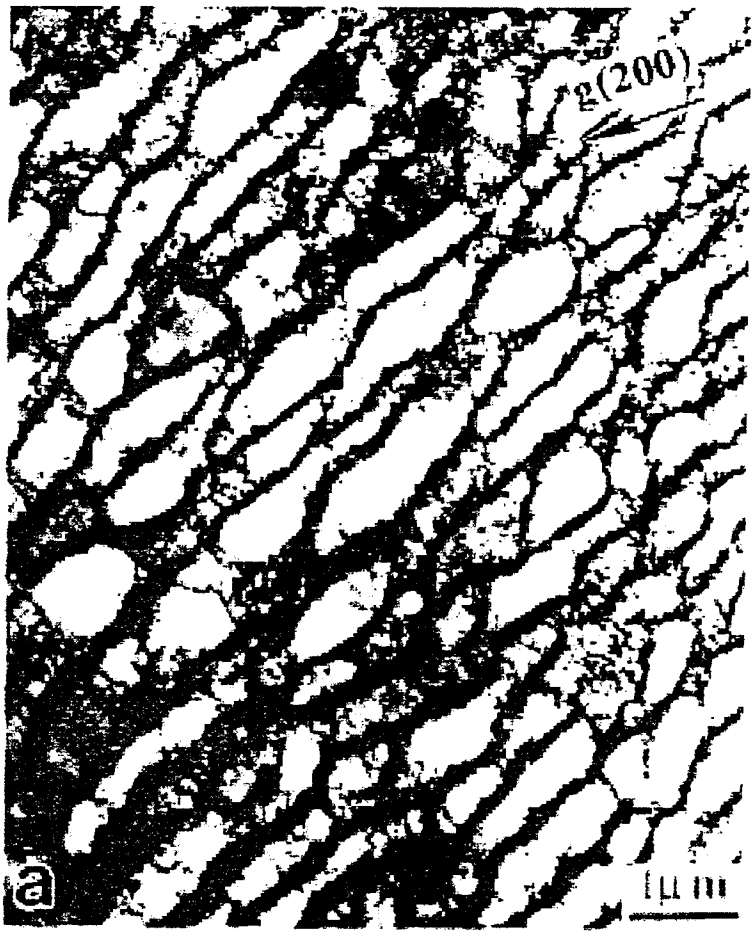

Figure 2.38 TEM micrograph of dipolar wall structure [19]

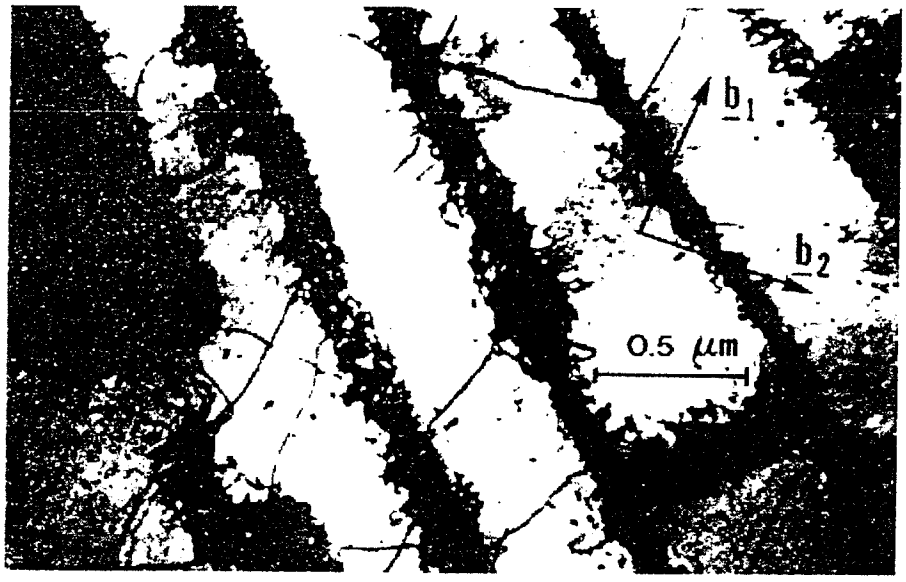

Figure 2.39 Screw dislocations gliding in the channels between wall structure [74]

exhibit a formation of cross slips that are considered an influence in the annihilation process of screw dislocations, which suppress the formation of PSBs [84,85].

Dislocation mobility that strongly affects dislocation substructures stability depends on the material's stacking fault energy (SFE). When SFE is high, dislocation mobility is great because of enhanced cross-slip; conversely, cross-slip is restricted in low SFE materials. As a result, some materials cyclically harden or soften more completely than others [64]. For example, in a relatively high SFE material such as copper, initially hard samples cyclically strain soften, and initially soft samples cyclically harden; thus, the cyclically stabilized condition is the same regardless of the initial state of the material as shown in Figure 2.40a. In this case, the mechanical properties of the material in the stabilized state are independent of prior strain history. This is not true for a low stacking fault energy material, where restricted cross-slip will prevent the development of a common dislocation state from an initially hard and soft conditions, respectively. Figure 2.40b shows that the low SFE material will cyclically soften or harden, but a final stabilized state is never completely achieved and is not equivalent for the two different starting conditions. For such materials, the "final" cyclically stabilized state is dependent on prior strain history [64]. Table 2.2 lists stacking fault energies of f.c.c. materials studied in this project including Cu-Zn alloy as an example of f.c.c. alloy.

It is apparent that factors, which favor easy cross slip of screw dislocations lead to the formation of cells and dipoles during fatigue. On the other hand, factors that favor difficult cross slip lead to multipoles and planar arrays. Variation in dislocation pattern appears to be determined chiefly by three variables, namely, slip character of the material, test temperature, and strain amplitude as shown schematically in Figure 2.41 [86].

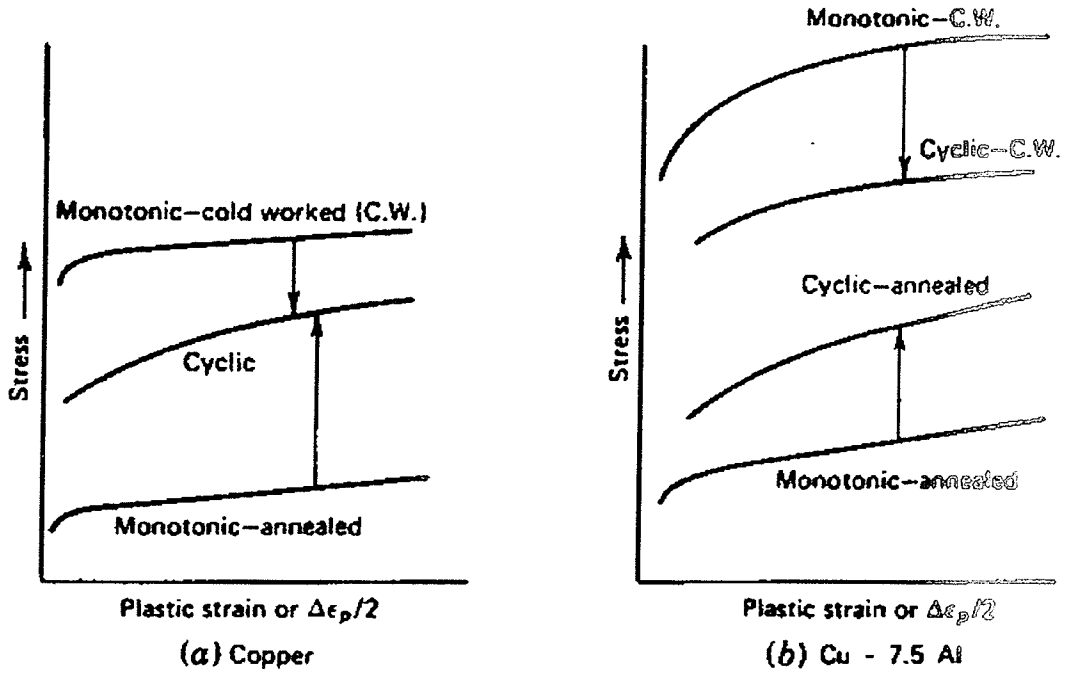

Figure 2.40 Cyclic response of (a) high stacking fault energy copper and (b) low stacking fault energy Cu-7.5% Al alloy [64]

Material	Stacking fault energy [mJ/m^2]
Aluminum	166
Nickel	125
Copper	55
Cu-15%Zn	27

Table 2.2 Stacking fault energy values of f.c.c. metals and alloys

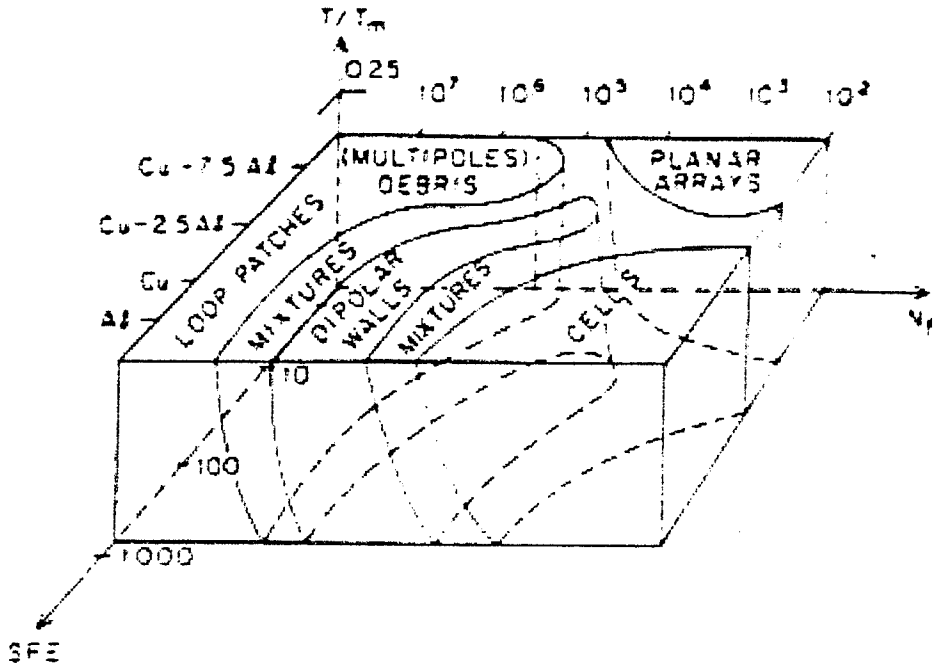

Figure 2.41 Schematic diagram of dislocation structures in f.c.c. metals as a function of amplitude life, temperature and slip character (SFE) [86]

CHAPTER THREE: EXPERIMENTAL PROCEDURE

3.1 INTRODUCTION

The metals that are being tested in this study are 99.0% purity aluminum belonging to the 1100 series and 99.53% purity nickel. The chemical compositions of aluminum and nickel are listed in Table 3.1. Both the aluminum and nickel rod stocks were machined into cylindrical fatigue specimens according to ASTM E466 standard. But prior to fatigue testing, sample preparation was carried out on both materials. A grain size of approximately 40 μm was obtained for both metals, by performing the appropriate heat treatments. The heat-treated specimens were then subjected to low cycle fatigue tests performed under constant strain amplitude control for various strain amplitudes. The tested specimens were then sectioned and prepared for microscopic examination. A detailed description of the experimental procedure followed in this study is provided in this chapter.

In order to be consistent with previous studies performed on aluminum and nickel, the experimental procedure and test parameters used in this study closely follow the methods used by Bassim and Liu [1] in their study of low cycle fatigue of polycrystalline copper.

3.2 SPECIMEN PREPARATION

A set of specimens for each of the two materials was machined to the specimen geometry shown on Figure 3.1 prior to heat treatment. These specimens were prepared to ASTM specifications E466 [5]. To permit mounting to the test fixture the specimens were threaded at both ends. In addition, to eliminate stress concentration, large radii were machined at the ends of the gauge length of the specimens, as indicated in Figure 3.1. The aluminium and nickel specimens were then heat treated at 500°C for 3hrs and at 650°C for 52hrs respectively. All specimens were wrapped up with steel foil wrap before putting them in the furnace in order to minimise surface oxidation. Both of these heat treatments yielded a grain size of approximately 40μm.

Material	Chemical Compositions (%)
Aluminium 1100	0.95 max. (Si + Fe), 0.05-0.2 (Cu), 0.1 max. (Zn), 0.05 max. (Mn), 99 min. (Al)
Nickel 200	0.35 max. (Si), 0.25 max. (Cu), 0.35 max. (Mn), 0.40 max. (Fe), 0.01 max. (S), 0.15 max. (C), 99 min. (Ni)

Table 3.1 Chemical compositions of polycrystalline aluminium and nickel

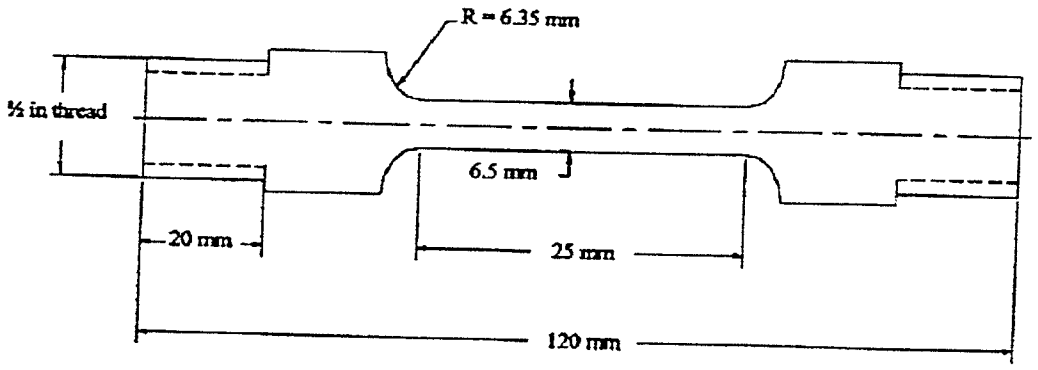

Figure 3.1 Specimen geometry according to ASTM Standard E466 [5]

3.3 OPTICAL MICROSCOPY

Samples were prepared, polished and etched for microscopic examination. Various chemical solutions as well as electro-etching were used in an attempt to reveal the microstructure of aluminium. Fluoboric acid is the elecro-etchant that revealed the microstructure of aluminium shown in Figure 3.2. The chemical solution used for etching nickel consists of a mixture of 50ml acetic acid and 50 ml nitric acid (HNO_3). The microstructure of nickel is shown in Figure 3.3.

3.4 LOW CYCLE FATIGUE TESTING PARAMETERS

In order to produce meaningful data for the generation of CSS curves and to allow comparison to previous studies, the appropriate test parameters have been chosen. The parameters used in the current study closely follow the test parameters used by Bassim and Liu [1].

3.4.1 Strain Control

Low cycle fatigue testing was performed under strain-controlled conditions as opposed to load-controlled conditions. Based on previous studies, it has been noted that for small plastic strain under load controlled conditions, cell structures could be created and the plateau region could be suppressed due to the high starting loads. Therefore fatigue cycling is performed under strain-controlled conditions. The product of the frequency and the total strain range (i.e. strain rate) was kept constant at 1E-04.

3.4.2 Strain Amplitude Range

The strain amplitude values used for aluminum and nickel ranged from 1.0E-03 to 1.1E-02. It should be noted that before these values are entered into the control unit they are multiplied by the gauge length of the displacement gauge since it measures the elongation of the specimen along its gauge length. In addition, the intermediate strain

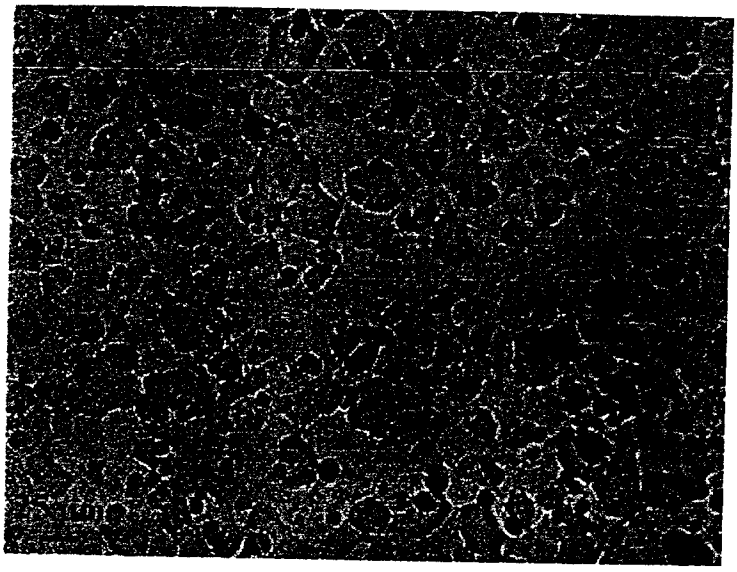

Figure 3.2 Optical micrograph of the microstructure of polycrystalline aluminium Etchant: Fluoboric acid.

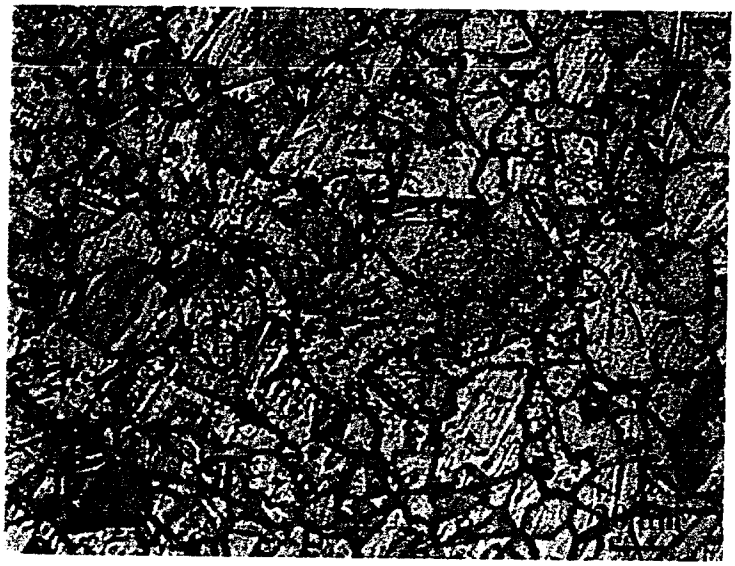

Figure 3.3 Optical micrograph of the microstructure of polycrystalline nickel Etchant: 50ml acetic acid and 50 ml nitric acid (HNO_3).

amplitude values were chosen by creating a rough cyclic stress-strain curve from various samples. In order to firmly define the transition between regions in the cyclic stress-strain curve, the strain amplitudes for the remaining test specimens were chosen to lie closely to the transitional areas.

3.4.3 Wave Form Control

The use of a triangular waveform results in a constant strain rate throughout a cycle. Whereas the use of a sine wave for the strain waveform results in a continually varying strain rate during the course of one cycle. Therefore, a triangular waveform was used for testing in the current study.

3.4.4 Frequency Control

The first concern, once the testing equipment has been balanced and calibrated, is to select the testing frequency. For cyclic frequencies of 0.1 to about 10 Hz and isothermal conditions, no significant differences in the life of metals at room temperature were found [3]. The testing frequency is more dependent on the system capabilities. The recording equipment and the dynamic characteristics of the extensometer usually limit the actual test frequencies, which can be employed [3]. The frequency used for cycling fatigue testing was adjusted such that the strain rate was constant in companion tests at different strain amplitudes.

3.5 LOW CYCLE FATIGUE TEST SET-UP

The specimen is firstly bolted into the upper fixture, then the hydraulic actuator is moved upwards until the lower end of the test fixture can be hand tightened to the actuator. A zero control load is then entered into the control unit allowing the lower bolts to be tightened further without incurring a pre-load on the specimen. The extensometer with an effective gauge length of 10mm was carefully positioned along the gauge length of the specimen using small elastic bands. When the specimen and extensometer in place

the next step is to select the desired strain-time waveform and the frequency at which the test will be run

3.5.1 Instron 1332 Servo-Hydraulic Test Unit

Fatigue testing was conducted using the Instron 1332 testing machine, which is connected to the Instron 8500 programmable control unit. The Instron 1332 unit has a load cell with a full load scale of 1000kg/1V. It is capable of accurately producing low strain amplitudes in the range of 10E-03 to 10E-05mm, which is actually necessary for performing strain controlled low cycle fatigue tests. The servo-hydraulic test unit applies a load with a hydraulic actuator while a computer-controlled servomechanism controls the oil flow to the actuator. The specimen is mounted on the test unit between the actuator and the load cell by screwing it into the test fixture. Figure 3.4 is a photograph of the test unit as well as testing set up.

The Instron 8500 programmable control unit is used to set up all the testing parameters. Furthermore, the Instron 8500 programmable control unit receives data from the displacement gauge and the load cell during fatigue testing. This data are then processed by the computer and based on the programmed test parameters, feedback is sent back to the servo valve to control the hydraulic actuator. This data is also sent to an X-Y analogue chart plotter, which generate the stress-strain hysteresis loops from which the saturated stress and plastic strain can be determined. Figure 3.5 is a block diagram of the control unit showing the input and output signals.

3.6 LOW CYCLE FATIGUE TESTING

These tests were conducted at room temperature under symmetric tension and compression at constant total strain amplitudes. Each specimen was tested at a constant strain rate of 10^{-4} until the saturation stress was reached. The saturation stress was determined when there is no further increase in saturation stress observed in hysteresis

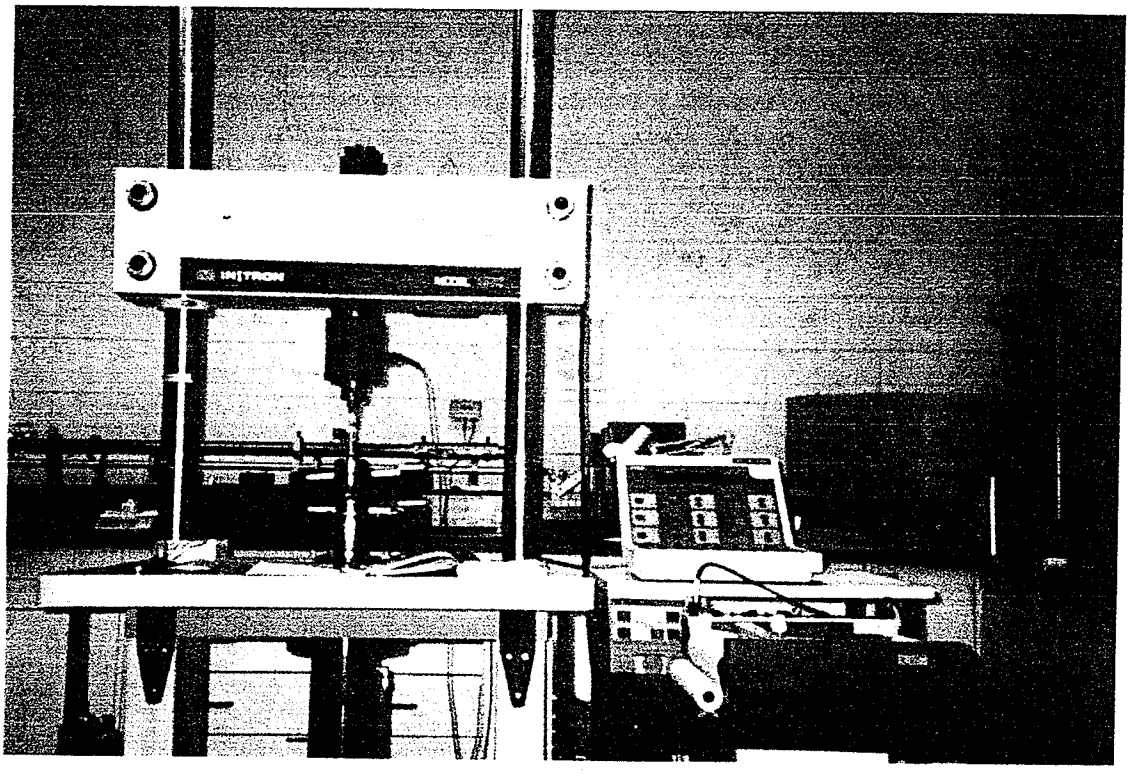

Figure 3.4 Photograph of Instron 1332 testing instrument, Instron 8500 programmable unit and chart recorder

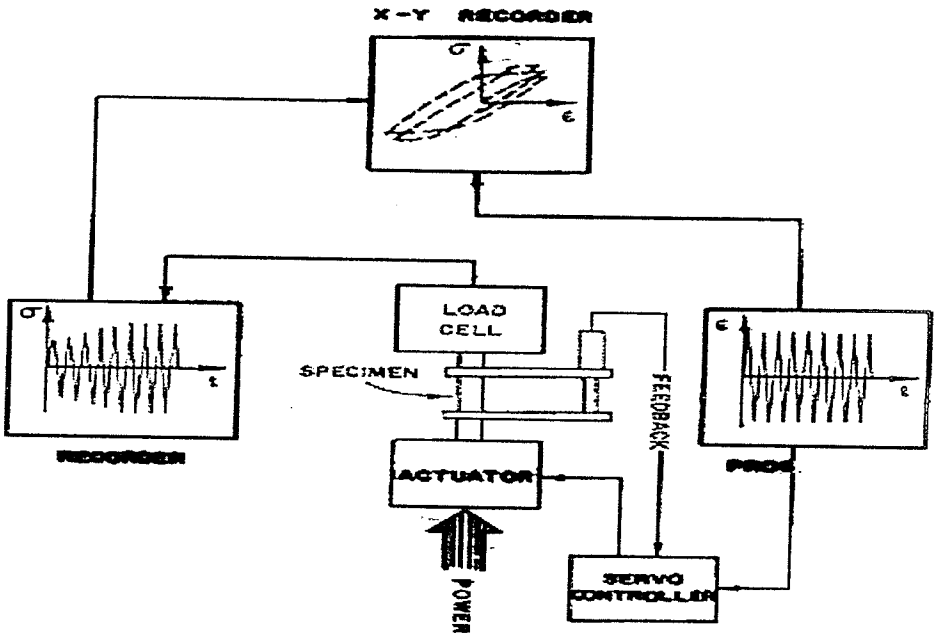

Figure 3.5 Block diagram of fatigue testing set-up

loops displayed on the chart plotter. From the hysteresis loops the stress amplitude σ_a, the strain amplitude ε_a and the plastic strain amplitude ε_{ap} were evaluated.

3.7 MICROSTRUCTURAL EXAMINATION OF TESTED SPECIMENS

In order to confirm the existence and study the characteristics of persistent slip bands as well as other micro-scale features, the microstructure of the fatigued specimens was analyzed microscopically. The gauge length of the specimens was cut along the longitudinal axis using the spark cutter in order to conserve the microstructure of the specimens. After cutting, the specimens were mounted polished and etched. Microstructural examination was performed using the JEOL 2000FX Transmission Electron Microscopy (TEM).

3.7.1 Transmission Electron Microscopy (TEM)

Detailed microstructural examination was carried out using JEOL 2000FX TEM operating at 180KV. A photograph of the microscope is shown in Figure 3.6. Thin foils of longitudinal section of the fatigued specimens were made to observe the through thickness grain structure as well as micro-scale defects. A 10 mm longitudinal strip was cut from the fatigued specimen. The strip was glued to a metal block and mechanically polished to a thickness between 70 μm and 100 μm. A 3 mm diameter punch was used to prepare several 3 mm diameter thin foils from the strip. All the thin foils were finally prepared by electropolishing in Struers Tenupol-3 Jet polisher. Table 3.2 lists the electrolyte solution and the optimum polishing conditions used in the preparation of TEM thin foils for both aluminium and nickel. The electrolyte was cooled by passing a liquid nitrogen coolant into the tank through cooling coils immersed in the electrolyte. Electrolyte flow rate was adjusted to a proper value since too fast flow rate may deform the foil and too slow flow rate may not attack the centre of the foil adequately.

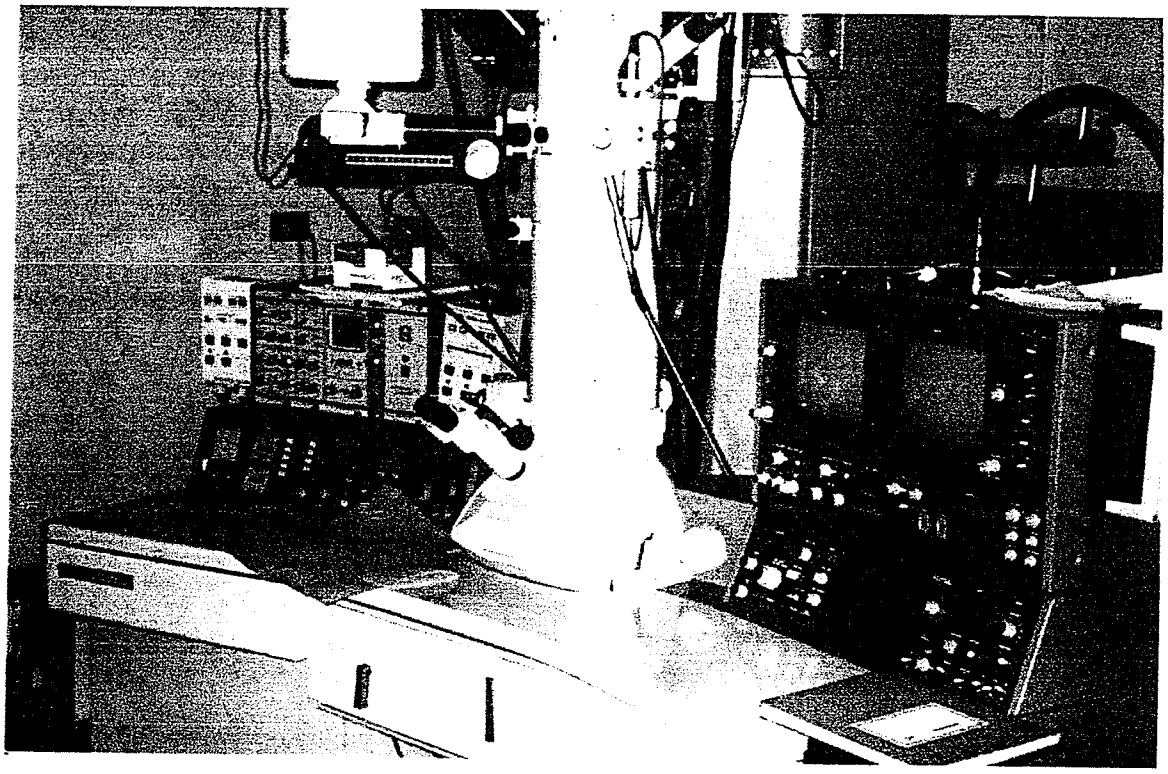

Figure 3.6 Photograph of JEOL 2000FX transmission electron microscope

Material	Electrolyte Solution	Optimum Polishing Conditions
Aluminium	25% nitric acid and 75% methanol	–18 °C, 16V
Nickel	20% Perchloric acid and 80% ethanol	–30°C, 20V

Table 3.2 Electrolyte solution and optimum polishing conditions for TEM thin foil preparation

CHAPTER FOUR: RESULTS AND DISCUSSIONS
POLYCRYSTALLINE ALUMINUM

4.1 INTRODUCTION

This chapter summarizes the experimental results for polycrystalline aluminium such as the cyclic response in terms of cyclic stress-strain curve and cyclic hardening curve. In additions, a detailed study of dislocation structures evolved upon cyclic deformation is included.

4.2 STRESS-STRAIN HYSTERESIS LOOP

Experimental stress-strain hysteresis loops of polycrystalline aluminium fatigued at different plastic strain amplitudes are shown in Figure 4.1 (a, b and c). It is noted from these loops that the linear elastic portion of the loop is the same regardless of plastic strain amplitude. The plastic part of the loop, i.e. the loop width characterizing material's ductility, is changed based on the controlled value of the plastic strain amplitude. However, the height of the loop corresponding to loading increases until saturation is reached. In addition, the hysteresis loop is more pointed at low amplitudes and becomes parallelogram in shape with higher plastic strain amplitude.

4.3 FATIGUE DATA

To present the cyclic deformation behaviour in terms of cyclic stress-strain curve, some calculations are needed to obtain the saturation stress and plastic strain amplitude from stress-strain hysteresis loop. Figure 4.2 is an example of a hysteresis loop showing the parameters used to calculate the stress and strain amplitudes

The height of the hysteresis loop depicts the total stress range, $\Delta\sigma_s$, and width of the loop depicts the total strain range, $\Delta\varepsilon_t$. The measured height is 40 mm for the stress range and the measured widths are 68 mm, 58 mm and 10 mm for the total strain, $\Delta\varepsilon_t$,

(a)

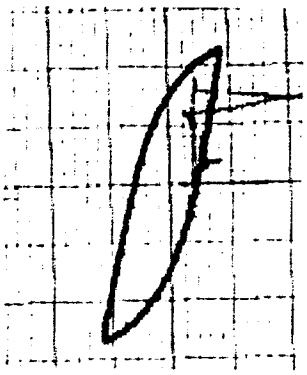

(b)

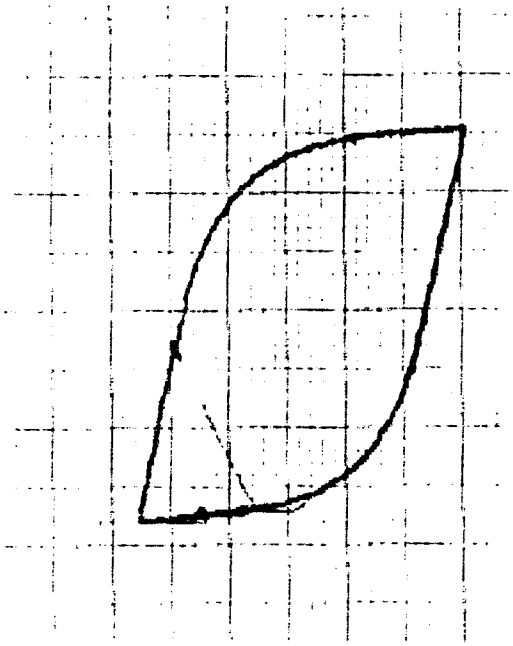

(c)

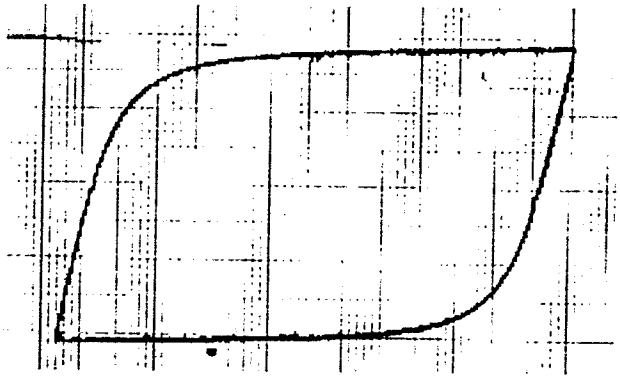

Figure 4.1 Stress-strain hysteresis loops

(a) $\Delta\varepsilon_{pl}/2 = 6.25 \times 10^{-4}$, $\Delta\sigma_s/2 = 37$ MPa
(b) $\Delta\varepsilon_{pl}/2 = 2.60 \times 10^{-3}$, $\Delta\sigma_s/2 = 49$ MPa
(c) $\Delta\varepsilon_{pl}/2 = 7.25 \times 10^{-3}$, $\Delta\sigma_s/2 = 59$ MPa

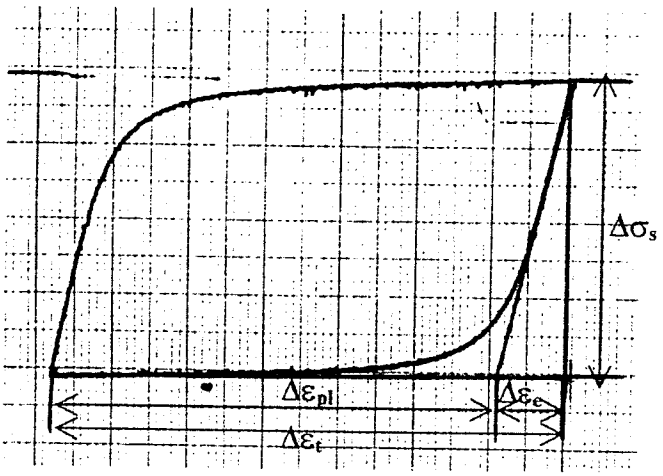

Figure 4.2 Stress-strain hysteresis loop ($\Delta\varepsilon_{pl}/2 = 7.25 \times 10^{-3}$, $\Delta\sigma_s/2 = 59$ MPa) showing stress and strain ranges.

plastic strain, $\Delta\varepsilon_{pl}$, and elastic strain, $\Delta\varepsilon_e$, ranges respectively. The stress and strain amplitudes are calculated by taking half of the stress and strain ranges. The extensometer gage length of 10 mm was used to obtain the strain values.

Calibration Factors:

0.25 V / 10 mm = calibration factor of Instron testing unit

0.1 mm / 1V = calibration factor of the chart recorder

a) Total strain amplitude, $\Delta\varepsilon_t/2$

$$68mm \times \left(\frac{0.25V}{10mm}\right) \times \left(\frac{0.1mm}{1V}\right) \times \left(\frac{1}{2}\right) = 0.085mm$$

$$\frac{0.085mm}{10mm} = 8.5 \times 10^{-3}$$

b) Plastic strain amplitude, $\Delta\varepsilon_{pl}/2$

$$58mm \times \left(\frac{0.25V}{10mm}\right) \times \left(\frac{0.1mm}{1V}\right) \times \left(\frac{1}{2}\right) = 0.0725mm$$

$$\frac{0.0725mm}{10mm} = 7.25 \times 10^{-3}$$

c) Elastic strain amplitude, $\Delta\varepsilon_e/2$

$$10mm \times \left(\frac{0.25V}{10mm}\right) \times \left(\frac{0.1mm}{1V}\right) \times \left(\frac{1}{2}\right) = 0.0125mm$$

$$\frac{0.0125mm}{10mm} = 1.25 \times 10^{-3}$$

d) Saturation stress

$$40mm \times \left(\frac{0.1V}{10mm}\right) \times \left(\frac{1000Kg}{1V}\right) \times \left(\frac{1}{2}\right) = 200Kg$$

$$F = mg = 200Kg \times 9.81\frac{m}{s^2} = 1962N$$

$$\sigma = \frac{F}{A} = \frac{4F}{\pi D^2} = \frac{4(1962N)}{\pi(0.0065)^2} = 59.1 \times 10^6 \frac{N}{m^2} = 59.1MPa$$

Table 4.1 lists the experimental conditions and results for all specimens tested, including the total strain amplitude, plastic strain amplitude and the saturation stress amplitude as well as the frequency used.

4.4 CYCLIC DEFORMATION BEHAVIOR

4.4.1 Cyclic Stress-Strain Curve

By plotting all saturation stress amplitudes, $\Delta\sigma_s/2$, as a function of plastic strain amplitudes, $\Delta\varepsilon_{pl}/2$, the cyclic stress-strain curve was obtained as shown in Figure 4.3. For comparison, the data of Tsou on polycrystalline aluminium [37] are also included with the present result in Figure 4.4. The difference in saturation stress may have resulted from the fact that polycrystalline aluminium of the current study with grain size of 40 μm exhibits higher saturation stress. This finding is in agreement with Hall-Petch relationship of grain size effect on cyclic deformation behaviour. It is also observed from the cyclic stress strain curve that the saturation stress increases markedly with increasing $\Delta\varepsilon_{pl}/2$ over all the strain amplitudes used in this study. This behaviour indicates that polycrystalline aluminium exhibits strain hardening upon cyclic deformation. Such hardening response would be due to the activation of secondary slip systems and the formation of three-dimensional dislocation structures.

Specimen	*Input Values*		*Output Values*	
	$\Delta\varepsilon_t/2$	**Frequency (Hz)**	$\Delta\varepsilon_{pl}/2$	$\Delta\sigma_s/2$ **(MPa)**
Al **5**	1.00E-03	0.100	1.84E-04	25.1
Al **4**	1.50E-03	0.067	3.47E-04	32.5
Al **3**	2.20E-03	0.045	6.48E-04	33.7
Al **6**	2.70E-03	0.037	7.99E-04	38.4
Al **2**	3.10E-03	0.032	1.03E-03	41.4
Al **7**	3.50E-03	0.029	1.24E-03	46.0
Al **1**	3.80E-03	0.026	1.28E-03	43.2
Al **16**	4.00E-03	0.025	1.40E-03	42.1
Al **15**	4.20E-03	0.024	1.45E-03	44.3
Al **8**	4.70E-03	0.021	1.63E-03	46.0
Al **9**	5.40E-03	0.019	2.00E-03	43.5
Al **10**	6.00E-03	0.017	2.18E-03	47.6
Al **11**	7.00E-03	0.014	2.70E-03	51.4
Al **12**	8.00E-03	0.013	3.17E-03	51.1
Al **13**	9.00E-03	0.011	3.62E-03	52.5
Al **14**	1.10E-02	0.009	4.37E-03	54.7

Table 4.1 Fatigue test data for polycrystalline aluminium

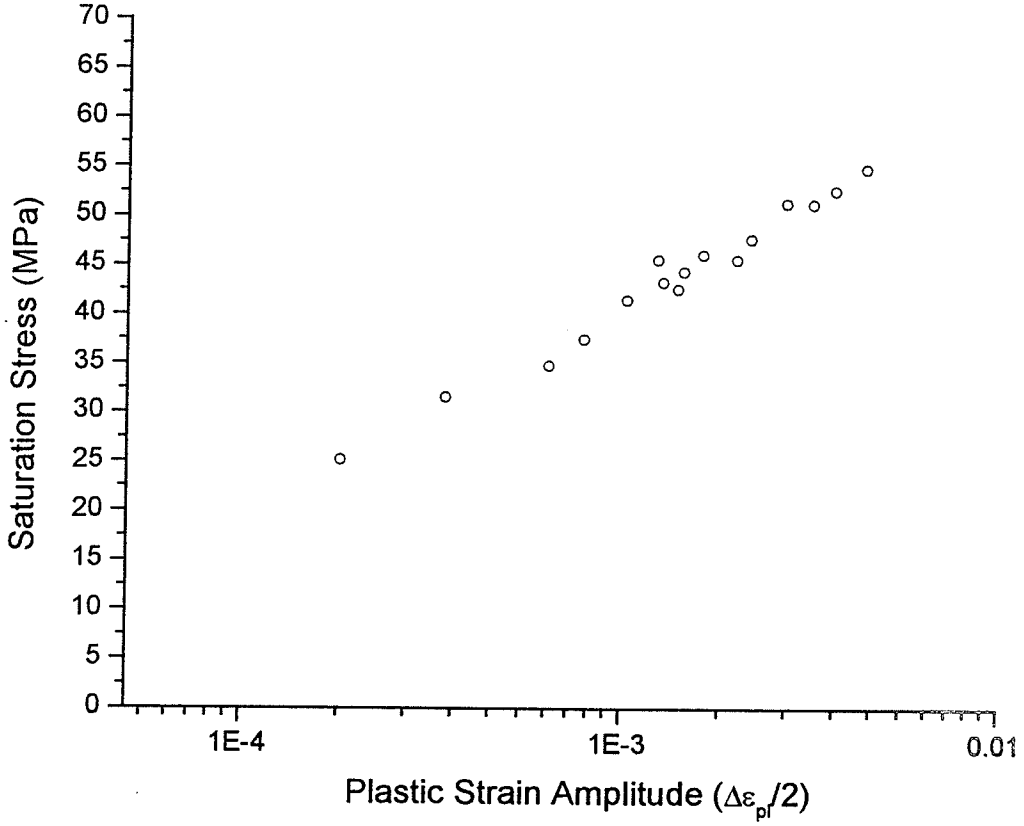

Figure 4.3 Cyclic stress-strain curve for polycrystalline aluminum

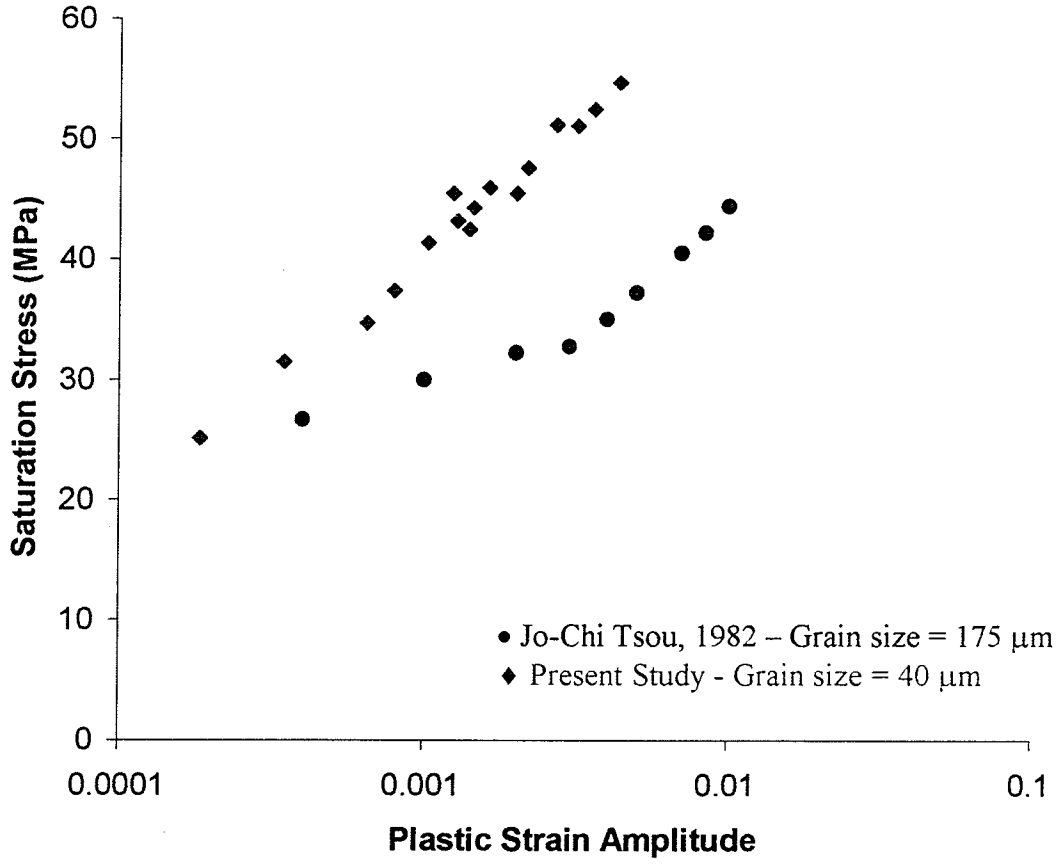

Figure 4.4 Cyclic stress-strain curve for polycrystalline aluminum as compared to Jo-Chi Tsou findings

4.4.2 Cyclic Hardening Curve

For annealed single phase FCC polycrystalline aluminium, the cyclic deformation response as depicted by the cyclic hardening curve in terms of fatigue cycles, N, is shown in Figure 4.5 for specimen tested at plastic strain amplitude 6.25×10^{-4}. Figure 4.6 is the cyclic hardening curve expressed in terms of cumulative plastic strain, ε_{cum}. Both figures show similar cyclic hardening behaviour regardless of the variable used in the x-axis. This would indicate that for a controlled plastic strain fatigue test, cyclic hardening behaviour could also be expressed with respect to cumulative plastic strain, which is 4 times number of cycles times plastic strain tested ($\varepsilon_{cum} = 4N\Delta\varepsilon_{pl}/2$). Cyclic hardening curve consists of an initial rapid hardening stage and a stress saturated stage. The continuously decreasing cyclic hardening rate (i.e. slope of the cyclic hardening curve) implies recovery mechanisms become more efficient upon further cycling deformation. In the stress-saturated stage of the cyclic hardening curve, the hardening mechanisms are completely balanced by recovery mechanisms.

An attempt was made to study the effect of plastic strain amplitude on the cyclic hardening behaviour and on the evolution of dislocation structures. Low cycle fatigue study was conducted using the same testing conditions, outlined in chapter 3, for three different plastic strain amplitudes. The relationship between the saturation stress and the plastic strain amplitude is shown in Figure 4.7. The cyclic hardening curves for specimens tested at three different plastic strain amplitudes are presented in Figure 4.8. It is shown in Figure 4.8 that the hardening rate decreases with cycling until saturation is reached. The number of cycles to saturation decreases with higher plastic strain amplitude. In addition, it is also noted that the cyclic hardening rate (i.e. the slope of the cyclic hardening curve) was most pronounced in the early stage of cycling and increased with plastic strain amplitude. The above findings indicated that, at large plastic strain amplitude, multiple glide systems become in operation enhancing cyclic strain hardening.

During the rapid hardening stage, mutual trapping of mobile dislocations into bundles and subsequent development into dislocation networks has been attributed to be

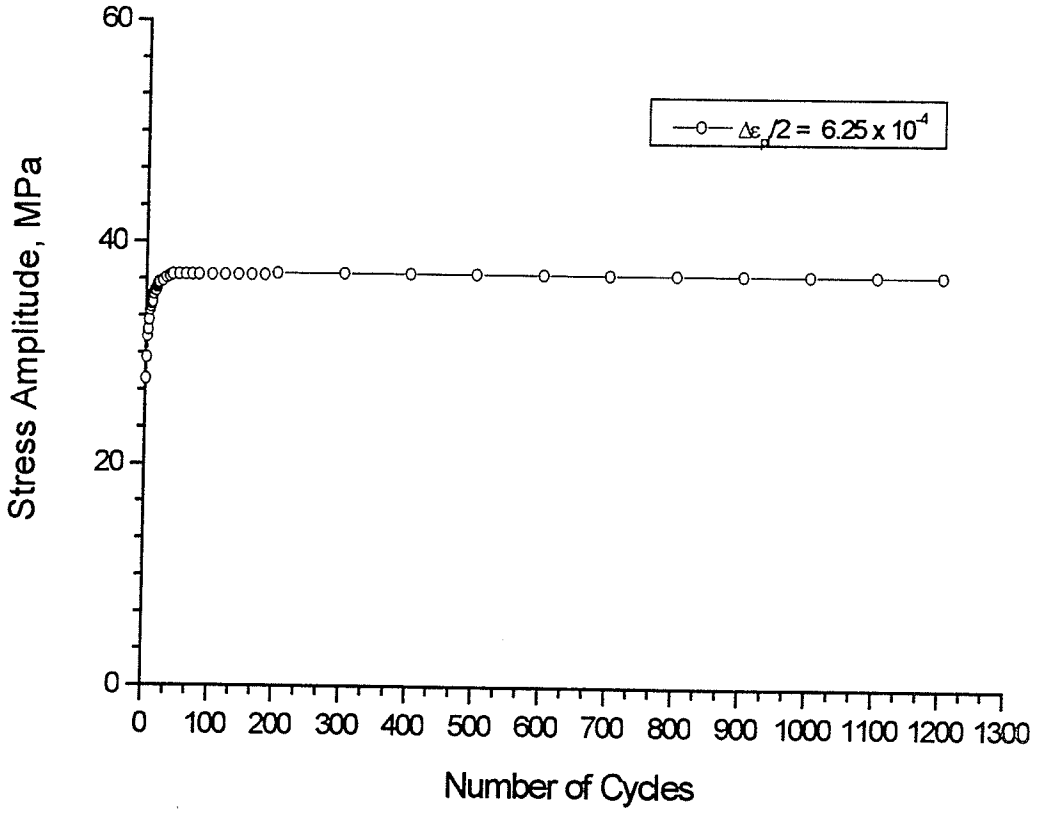

Figure 4.5 Cyclic hardening curve (with respect to number of cycles) for polycrystalline aluminum

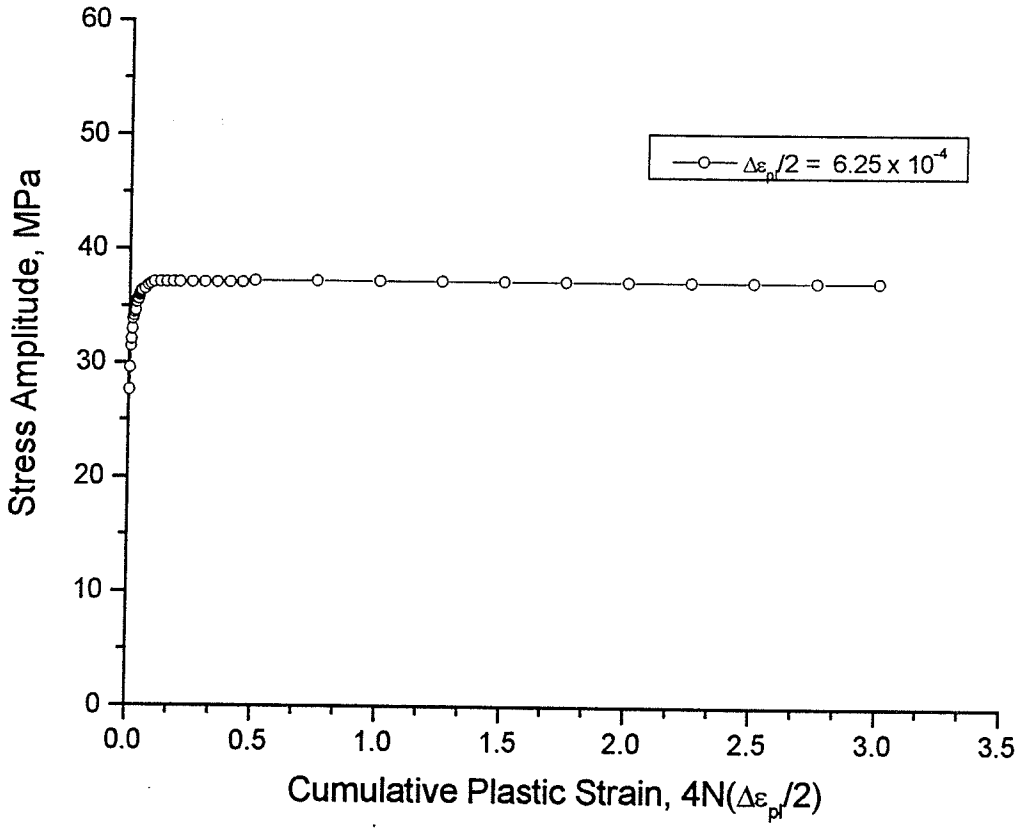

Figure 4.6 Cyclic hardening curve (with respect to cumulative plastic strain) for polycrystalline aluminum

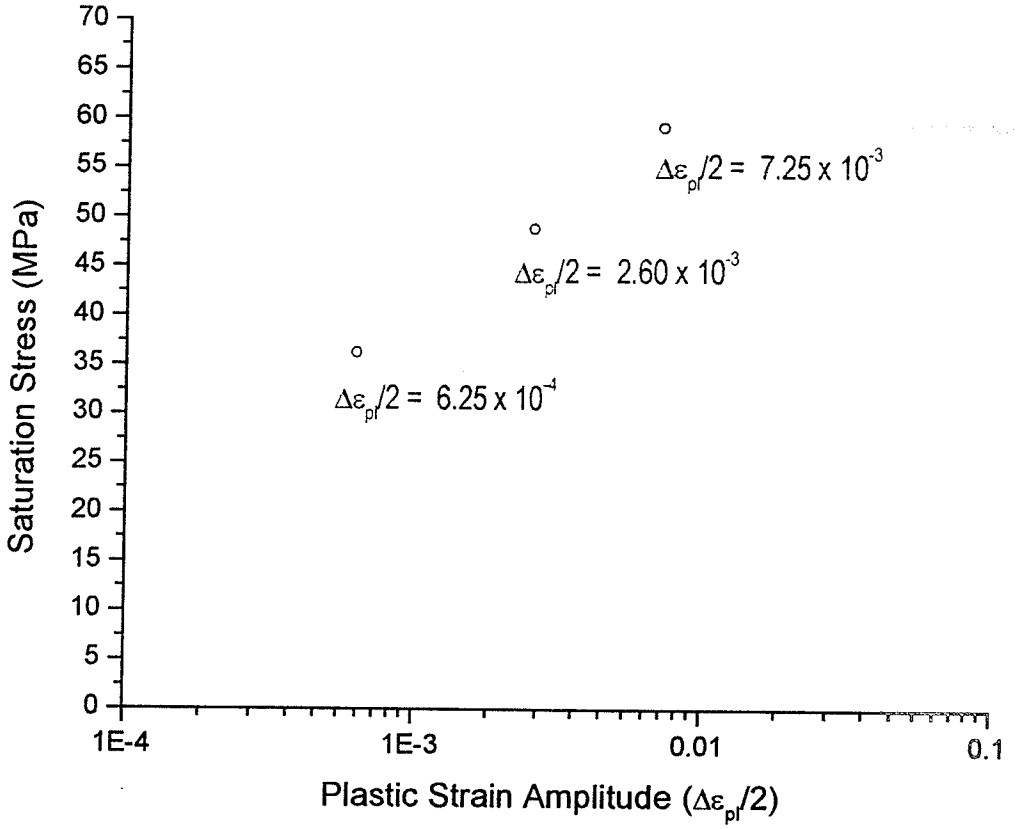

Figure 4.7 Relationship between plastic strain amplitude and saturation stress

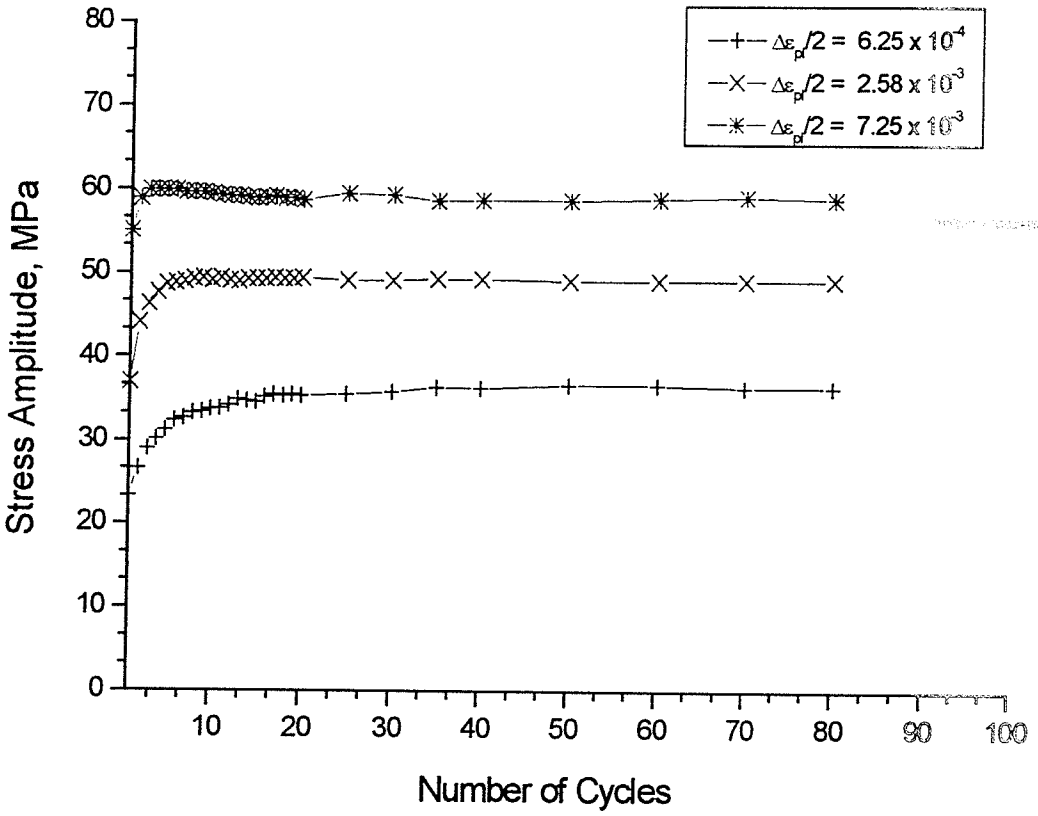

Figure 4.8 Cyclic hardening curves for polycrystalline aluminum showing the effect of plastic strain amplitude on the cyclic hardening behavior

the operating hardening mechanism. As the cyclic hardening rate levels off and eventually reaches a stress-saturated stage, the deformation reaches that of a dynamic steady state, which is termed the saturation stage.

Stable dislocation cellular structure consists of dislocation free regions (cell interiors) and regions of high dislocation density (cell walls), as shown in Figure 4.9, will not exist if a trapping mechanism is in operation during saturation fatigue. This suggests that the hardening mechanism during saturation fatigue can only be the result of the developed microstructure. As suggested by Feltner and Laird [64], the hardening mechanism during stress saturation is bowing of screw dislocations situated in the cell walls toward cell interior, which is called dislocation cell shuttling mechanism. A TEM micrograph showing bowed out screw dislocations within cell interior is shown in Figure 4.10. In the saturation stage, after further cyclic deformation, hardening mechanism is balanced with recovery mechanism associated with migration of cell wall driven by "cell wall energy" to form a stabilized low energy dislocation structure.

4.5 MICROSTRUCTURAL OBSERVATIONS

4.5.1 Cyclic Stress-Strain Response and Dislocation Structures

Dislocation cell structure is the predominant dislocation structure in polycrystalline aluminium subjected to cyclic deformation at plastic strain amplitudes used in this study. The dependence of dislocation cell size on saturation stress was evaluated over the plastic strain amplitude range studied. The average cell size was obtained by measuring the two dimensions of each cell from many electron micrographs (shown from Figure 4.11 to Figure 4.16). Table 4.2 summarizes the cell size in microns of dislocation cell structure formed at different plastic strain amplitudes.

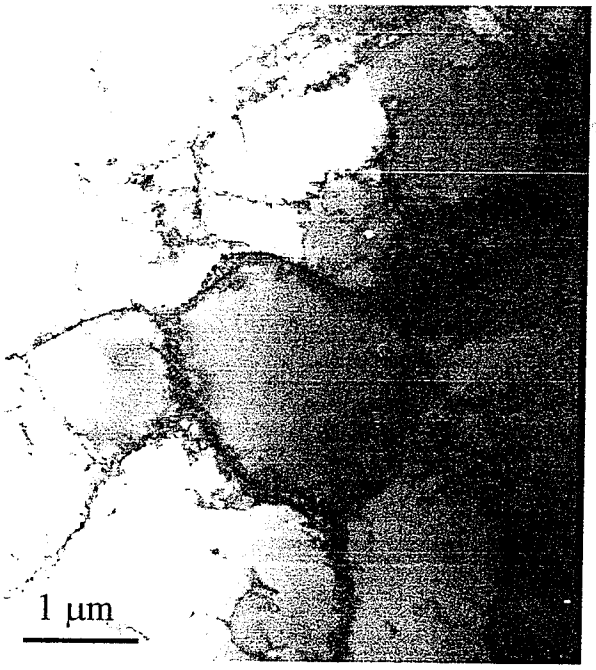

Figure 4.9 Dislocation cell structure showing dislocation-free cell interior and condensed cell walls.

Figure 4.10 Dislocation cell structure showing curved screw dislocations (as indicated by arrows) bowing towards and gliding within cell interior.

$\Delta\varepsilon_{pl}/2$	$\Delta\sigma_s/2$ (MPa)	*Cell Size (μm)*	*Reference*
1.84×10^{-4}	25	1.83	Figure 4.11
6.48×10^{-4}	34	1.72	Figure 4.12
1.4×10^{-3}	42	1.60	Figure 4.13
2.18×10^{-3}	48	1.53	Figure 4.14
2.70×10^{-3}	51	1.46	Figure 4.15
4.37×10^{-3}	55	1.35	Figure 4.16

Table 4.2 Dislocation cell size at different plastic strain amplitudes

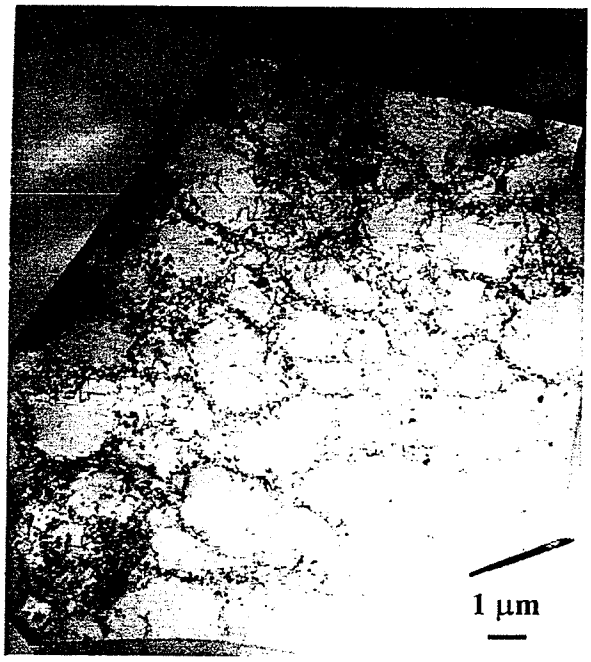

Figure 4.11 Dislocation cell structure in fatigued specimen at plastic strain amplitude $\Delta\varepsilon_{pl}/2 = 1.84 \times 10^{-4}$. $\Delta\sigma_s/2 = 25$ MPa. Cell size = 1.83 μm.

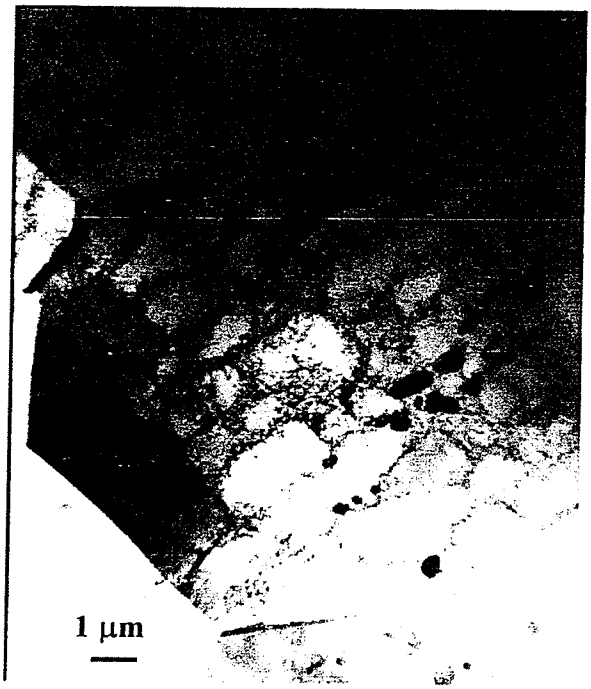

Figure 4.12 Dislocation cell structure in fatigued specimen at plastic strain amplitude $\Delta\varepsilon_{pl}/2 = 6.48 \times 10^{-4}$. $\Delta\sigma_s/2 = 34$ MPa. Cell size = 1.72 μm.

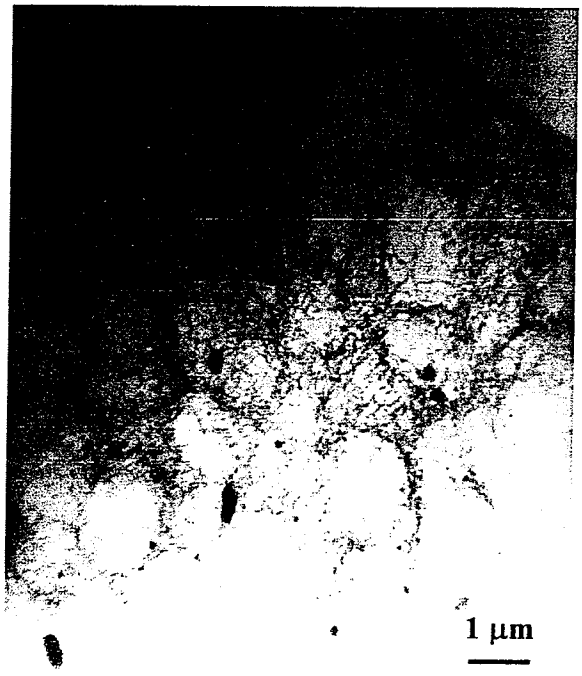

Figure 4.13 Dislocation cell structure in fatigued specimen at plastic strain amplitude $\Delta\varepsilon_{pl}/2 = 1.4 \times 10^{-3}$. $\Delta\sigma_s/2 = 42$ MPa. Cell size = 1.60 μm.

Figure 4.14 Dislocation cell structure in fatigued specimen at plastic strain amplitude $\Delta\varepsilon_{pl}/2 = 2.18 \times 10^{-3}$. $\Delta\sigma_s/2 = 48$ MPa. Cell size = 1.53 μm.

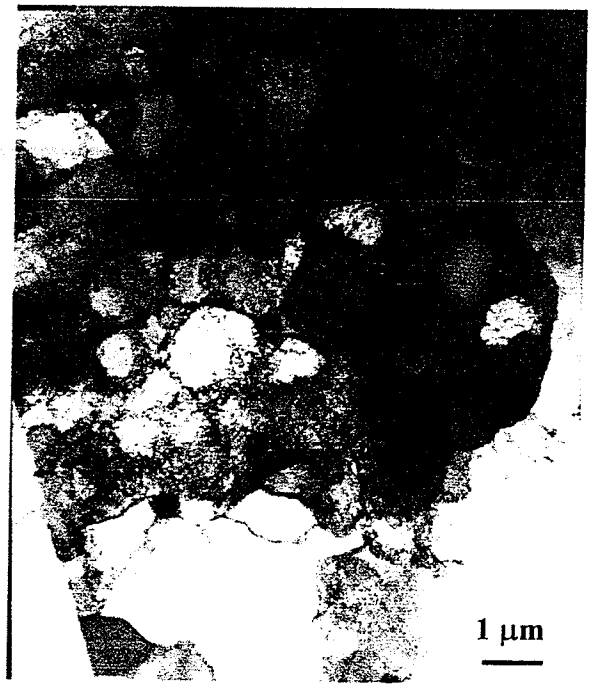

Figure 4.15 Dislocation cell structure in fatigued specimen at plastic strain amplitude $\Delta\varepsilon_{pl}/2 = 2.70 \times 10^{-3}$. $\Delta\sigma_s/2 = 51$ MPa. Cell size = 1.46 μm.

Figure 4.16 Dislocation cell structure in fatigued specimen at plastic strain amplitude $\Delta\varepsilon_{pl}/2 = 4.37 \times 10^{-3}$. $\Delta\sigma_s/2 = 55$ MPa. Cell size = 1.35 μm.

The average cell size is plotted as a function of plastic strain amplitude as shown in Figure 4.17. The reduction of dislocation cell size with plastic strain amplitude is an example of the evolution of cell structures with cyclic deformation in polycrystalline aluminums. A plot of cell size versus saturation stress is shown in Figure 4.18. Figure 4.19 is a plot of inverse cell size with saturation stress. It is clearly shown that the stress is found to be linearly related to the inverse cell size, which is directly predicted by the mesh-length theory of work hardening.

4.5.2 Mesh-length Theory of Work Hardening

The presence and development of dislocation cells play an important role in the mesh-length theory of work hardening [87]. The mesh-length theory of strain hardening is based on the arrangement of dislocations into stress-screened, low-energy configuration namely dislocation cell structures. When glide dislocations interact with each other, they mutually screen their long-range stress fields to form dislocation cells. The cells shrink in size as the flow stress, the stress needed to generate new glide dislocations, increases until they reach a critical cell size, L_c, where further shrinking does not take place as the strain is further increased.

After the establishment of the ultimate cell size the dislocation density in cell walls still increases, however no additional dislocation tangles can be formed within the cells. To accommodate the additional strain, the dislocation tangles in the cell walls may move cooperatively without generation of new dislocations.

The relationship between saturation stress and the inverse cell size obtained in this study agrees to some extent with the mesh-length theory of work hardening. However, a critical cell size after which there is no decrease in cell size with strain amplitude was not observed. In this study, the mesh-length theory is related to the obtained results qualitatively explaining the reduction of cell size with plastic strain and saturation stress. Such a relationship in the study of fatigue has not been established quantitively, which is beyond the scope of the present study.

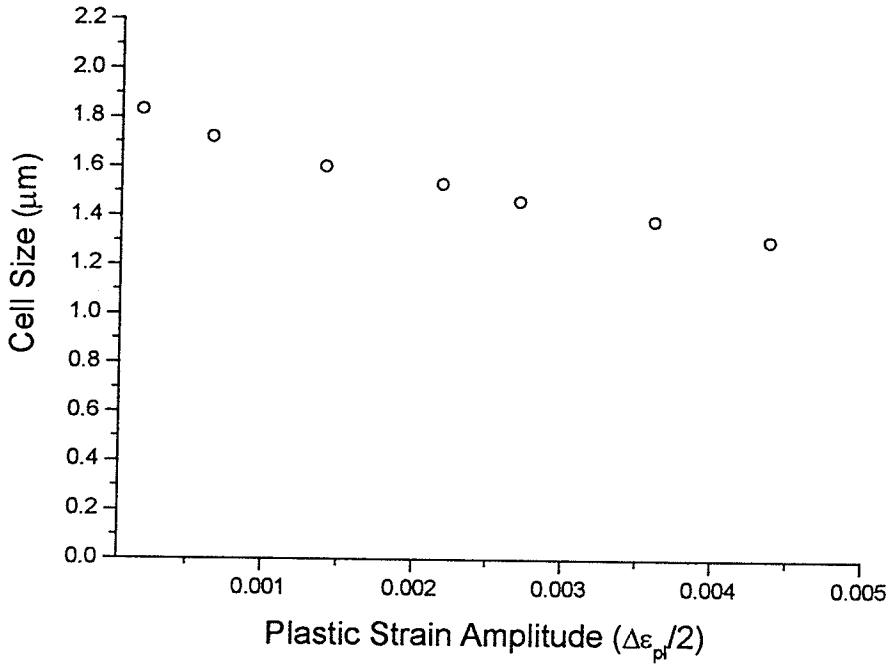

Figure 4.17 Relationship between dislocation cell size and plastic strain amplitude for polycrystalline aluminum

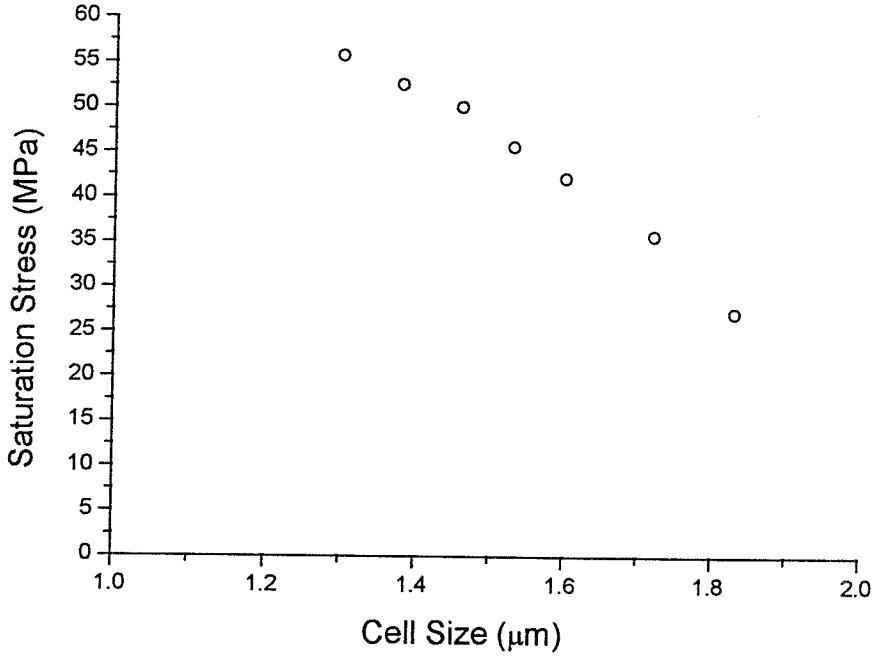

Figure 4.18 Relationship between saturation stress and dislocation cell size for polycrystalline aluminum

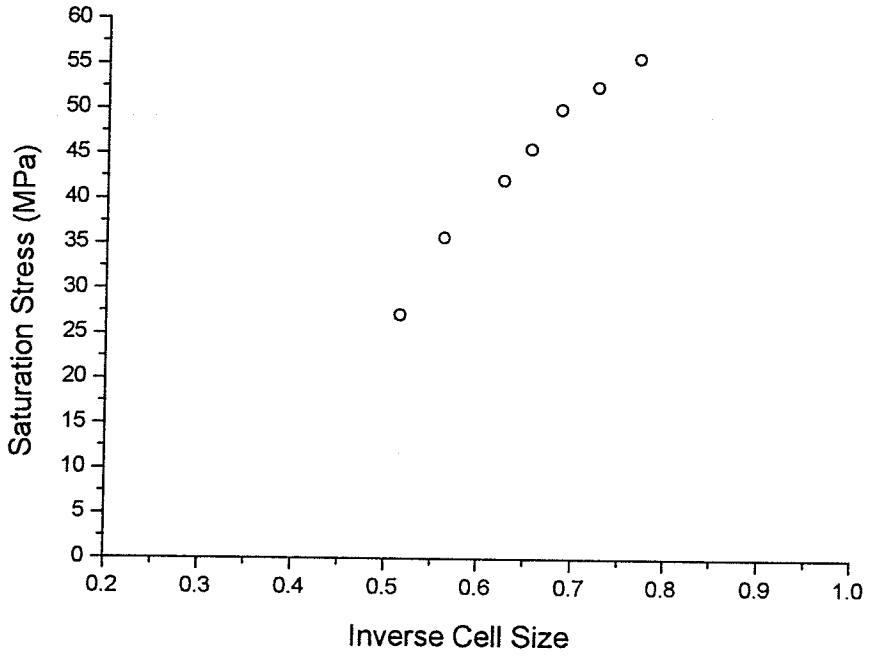

Figure 4.19 Relationship between saturation stress and inverse dislocation cell size for polycrystalline aluminum

4.5.3 Effect of Strain Amplitude

Dislocation structures evolved upon cyclic deformation at three different plastic strain amplitudes are evaluated in terms of cell size and wall thickness. Such evaluation would assist in relating the plastic strain amplitude or saturation stress to dislocation structures.

Dislocation cellular structure, observed in specimens cycled at low plastic strain amplitude of 6.25×10^{-4}, exhibits thick walls composed of entangled dislocations as shown in Figure 4.20 to Figure 4.22. It is apparent from Figure 4.20 that dislocation cell walls are formed in two different orientations indicating the operation of multiple slip systems. The activation of multiple slip systems along with the increase in the strain amplitude would favour the development of three-dimensional cell structure as shown in Figure 4.22. As the plastic strain amplitude increases to 2.60×10^{-3}, dislocation cell walls become condensed containing high dislocation density as shown in Figure 4.23. At larger plastic strain amplitude of 7.25×10^{-3}, dislocation cells are more equiaxed and show well defined and condensed cell walls as shown in Figure 4.24 and Figure 4.25. It is also found that the dislocation cell size decreased with plastic strain amplitude.

Cyclic deformation performed with medium to large plastic strain amplitude causes multiple slip to occur which results in the formation of dislocation cellular structure. For large strain amplitude fatigue, multiple slip occurs extensively in the polycrystalline aluminium. As a result the number of mobile dislocations increases and dislocation activity on other slip systems also increases with increase in strain amplitude. This results in the development of dislocation cell structures and an increase in the density of dislocations at cell walls. Table 4.3 lists the cell size and cell wall thickness of dislocation cell structure formed at three different plastic strain amplitudes.

Plastic Strain Amplitude, $\Delta\varepsilon_{pl}/2$	*Cell Size (μm)*	*Cell Wall Thickness (μm)*	*Reference*
6.25×10^{-4}	1.90 ± 0.05	0.252 ± 0.008	Figure 4.20 to 4.22
2.60×10^{-3}	1.60 ± 0.08	0.180 ± 0.005	Figure 4.23
7.25×10^{-3}	1.30 ± 0.05	0.080 ± 0.007	Figure 4.24 & 25

Table 4.3 Dislocation cell size and cell wall thickness at different plastic strain amplitudes

Figure 4.20 Dislocation cell structure in fatigued specimen at plastic strain amplitude $\Delta\varepsilon_{pl}/2 = 6.25 \times 10^{-4}$. $\Delta\sigma_s/2 = 37$ MPa. Cell size = 1.91 μm. Wall thickness = 0.246 μm

Figure 4.21 Dislocation cell structure in fatigued specimen at plastic strain amplitude $\Delta\varepsilon_{pl}/2 = 6.25 \times 10^{-4}$. $\Delta\sigma_s/2 = 37$ MPa. Cell size = 1.83 μm. Wall thickness = 0.250 μm

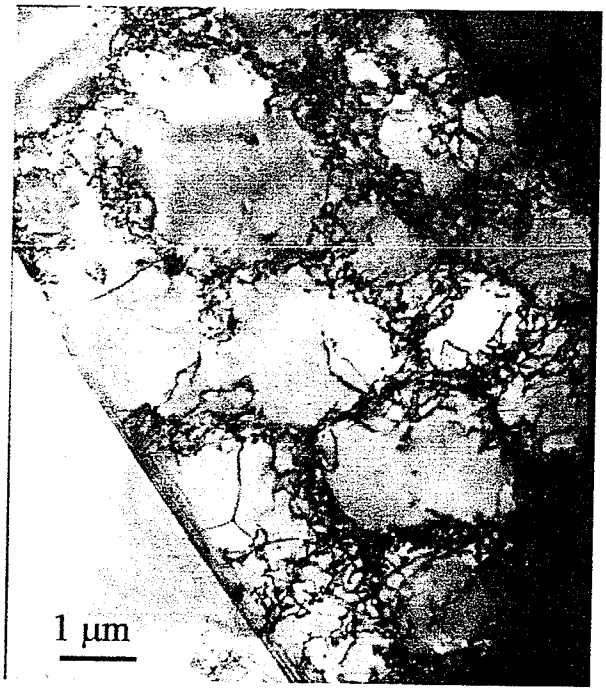

Figure 4.22 Dislocation cell structure in fatigued specimen at plastic strain amplitude $\Delta\varepsilon_{pl}/2 = 6.25 \times 10^{-4}$. $\Delta\sigma_s/2 = 37$ MPa. Cell size = 1.88 μm. Wall thickness = 0.240 μm

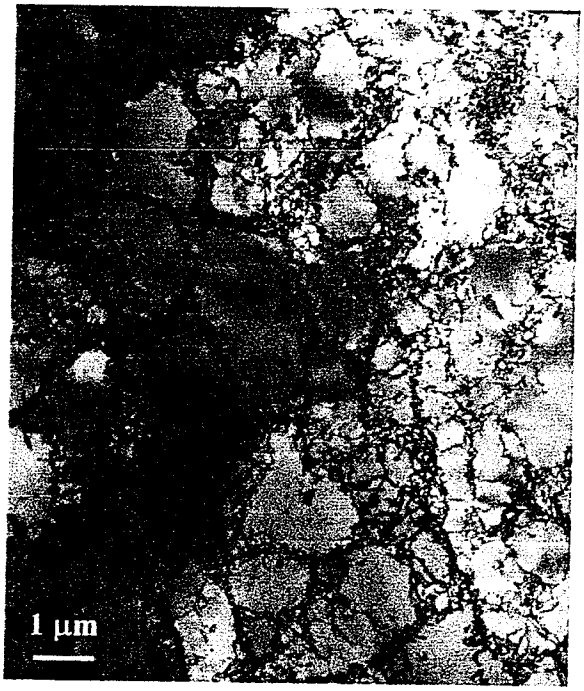

Figure 4.23 Dislocation cell structure in fatigued specimen at plastic strain amplitude $\Delta\varepsilon_{pl}/2 = 2.60 \times 10^{-3}$. $\Delta\sigma_s/2 = 49$ MPa. Cell size = 1.65 μm. Wall thickness = 0.178 μm

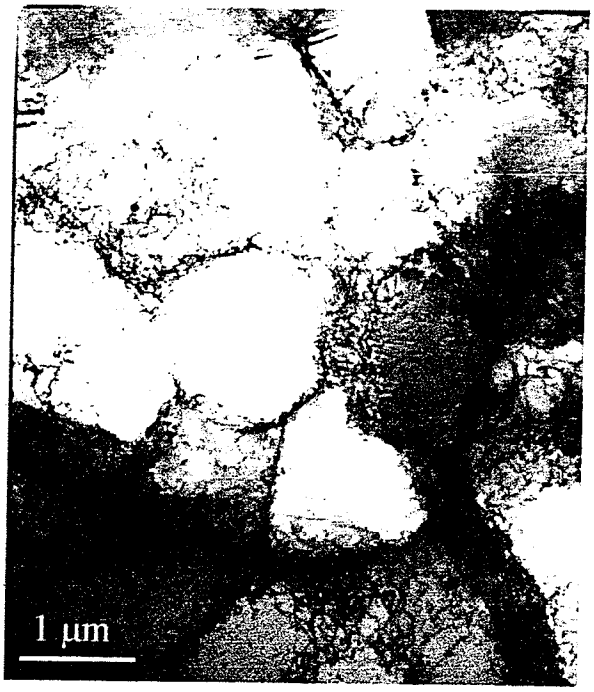

Figure 4.24 Dislocation cell structure in fatigued specimen at plastic strain amplitude $\Delta\varepsilon_{pl}/2 = 7.25 \times 10^{-3}$. $\Delta\sigma_s/2 = 59$ MPa. Cell size = 1.26 μm. Wall thickness = 0.070 μm

Figure 4.25 Dislocation cell structure in fatigued specimen at plastic strain amplitude $\Delta\varepsilon_{pl}/2 = 7.25 \times 10^{-3}$. $\Delta\sigma_s/2 = 59$ MPa. Cell size = 1.26 μm. Wall thickness = 0.060 μm

4.5.4 Effect of Fatigue Cycles

The cycle number influence on the dislocation structure has been studied for a strain amplitude value of 6.25 E-04. Microscopy observations have been made after the following fatigue cycle numbers: 5, 80, 300 and 1200. A cellular dislocation structure with cell size of 1.6 μm is observed as early as the first few fatigue cycles as shown in Figure 4.26 a. However the dislocation cell structure is not well developed and exhibited loose cell walls composed of entangled dislocations. As the cycle number increases to 80 cycles, cell walls become more condensed and the cell structure is more developed as shown in Figure 4.26 b. After cyclic saturation, i.e. after 80 fatigue cycles, the dislocation cell size remained constant with cycling at approximately 1.4 μm. However, the cell structure becomes more condensed and well developed as shown in Figure 4.26 c and d.

It is apparent that dislocation cell size during the stress saturation stage of cyclic deformation remained unchanged. This finding could be explained by the mechanism of cross-slip of screw dislocations and climb of edge dislocations within the cell walls, which results in maintaining constant dislocation density and consequently constant cell structure during stress saturation stage.

The operation of cross-slip and climb mechanism is mainly driven and enhanced by the stacking fault energy. A larger value of SFE in aluminum makes secondary slip (i.e. slip on more than one glide system) easier and increases the probability of cross slip because of the lower stress required for dislocation intersection. The ability of dislocations to cross slip easily favors the formation of dislocation cell structures. In addition, aluminium, the material with the greatest tendency for wavy slip, forms a cell structure even at low strain amplitudes. As a result materials of wavy slip mode will always form cell structures at high strain amplitudes.

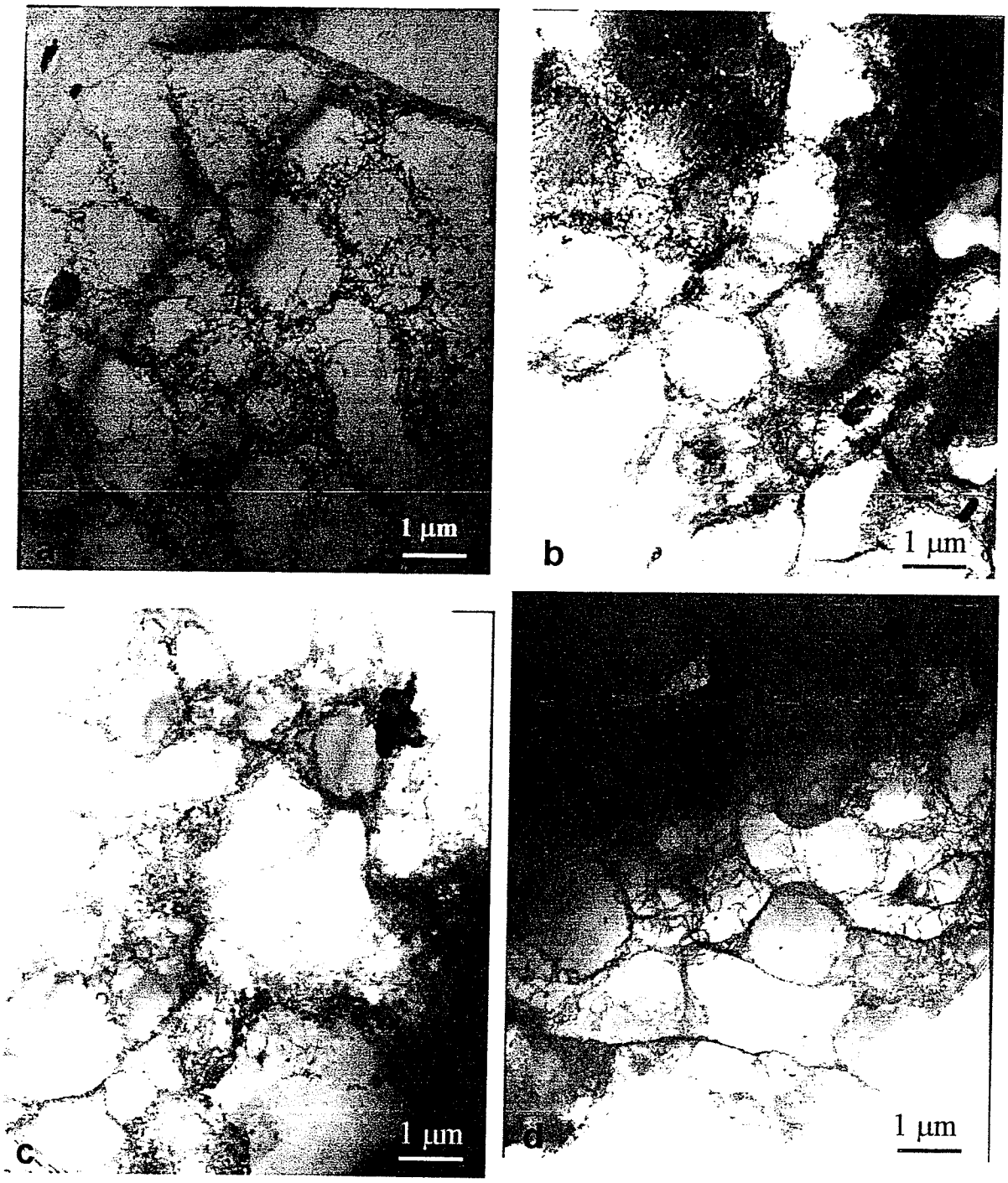

Figure 4.26 Dislocation structure evolution during cycling at $\Delta\varepsilon_{pl}/2 = 6.25 \times 10^{-4}$.
a) Dislocation structure after 5 fatigue cycles. Cell size = 1.60 μm
b) Dislocation structure after 80 fatigue cycles. Cell size = 1.44 μm
c) Dislocation structure after 300 fatigue cycles. Cell size = 1.43 μm
d) Dislocation structure after 1200 fatigue cycles. Cell size = 1.41 μm

4.6 SUMMARY

The cyclic deformation behavior of polycrystalline aluminum, as depicted by the cyclic stress-strain curve, exhibited cyclic hardening at which saturation stress increased with plastic strain at all plastic strain amplitudes tested. A comparison of the cyclic stress-strain response of polycrystalline aluminum with previous results revealed that fine-grain material exhibited higher saturation stress than coarse-grained material as predicted by a Hall-Petch relationship of grain size effect. In addition, the plastic strain amplitude at which the test was conducted influences cyclic hardening rate. It is found that the larger the plastic strain amplitude, the more pronounced the cyclic strain hardening.

Microscopy investigations revealed a continual increase in the propensity for cell structure formation in polycrystalline aluminum with plastic strain amplitude and fatigue cycle. Dislocation cell structure is the dominant deformation structure in deformed polycrystalline aluminum. No persistent slip bands or labyrinth structures have been observed in fatigued pure aluminum. The high value of stacking fault energy of aluminum polycrystals accounts for such behavior. High stacking fault energy favors the activation of multiple glide systems and formation of three-dimensional dislocation structures. In addition, microscopy observations revealed that dislocation cells become increasingly equiaxed and smaller and cell walls become more condensed with increase of strain amplitude.

A correlation between stress-strain response and development of dislocation structures in deformed polycrystalline aluminum revealed that the saturation stress is linearly related to the inverse dislocation cell size. This relationship is equivalent to the mesh-length theory of work hardening over the strain range used in this study.

CHAPTER FIVE: RESULTS AND DISCUSSIONS
POLYCRYSTALLINE NICKEL

5.1 INTRODUCTION

This chapter summarizes the experimental results for polycrystalline nickel such as the cyclic response in terms of cyclic stress-strain curve and cyclic hardening curve. The evolution of dislocation structures with cyclic deformation is studied. In addition, a correlation of the dislocation structure with plastic strain amplitude and cycle number is discussed.

5.2 STRESS-STRAIN HYSTERESIS LOOP

Experimental stress-strain hysteresis loop of polycrystalline nickel fatigued at plastic strain amplitude of 4.38 $x10^{-3}$ is shown in Figure 5.1. Stress amplitude increases rapidly in the initial several cycles and the increase of stress per cycle decreases with increasing number of cycles until it reached to saturation after 22 fatigue cycles. Strain hardening rate, the slop of the hysteresis loop, is higher in first quarter cycle of compressive deformation, but, after second cycle at same strain, no appreciable change in the strain hardening rate can be noted from cycle to cycle.

5.3 FATIGUE DATA

Table 5.1 lists the experimental conditions and results for all specimens tested, including the total strain amplitude, plastic strain amplitude and the saturation stress amplitude as well as the frequency used. Similar calculations, as outlined in section 4.3, were performed to obtain the saturation stress and plastic strain amplitude from stress-strain hysteresis loop and present the cyclic deformation in terms of cyclic stress-strain curve.

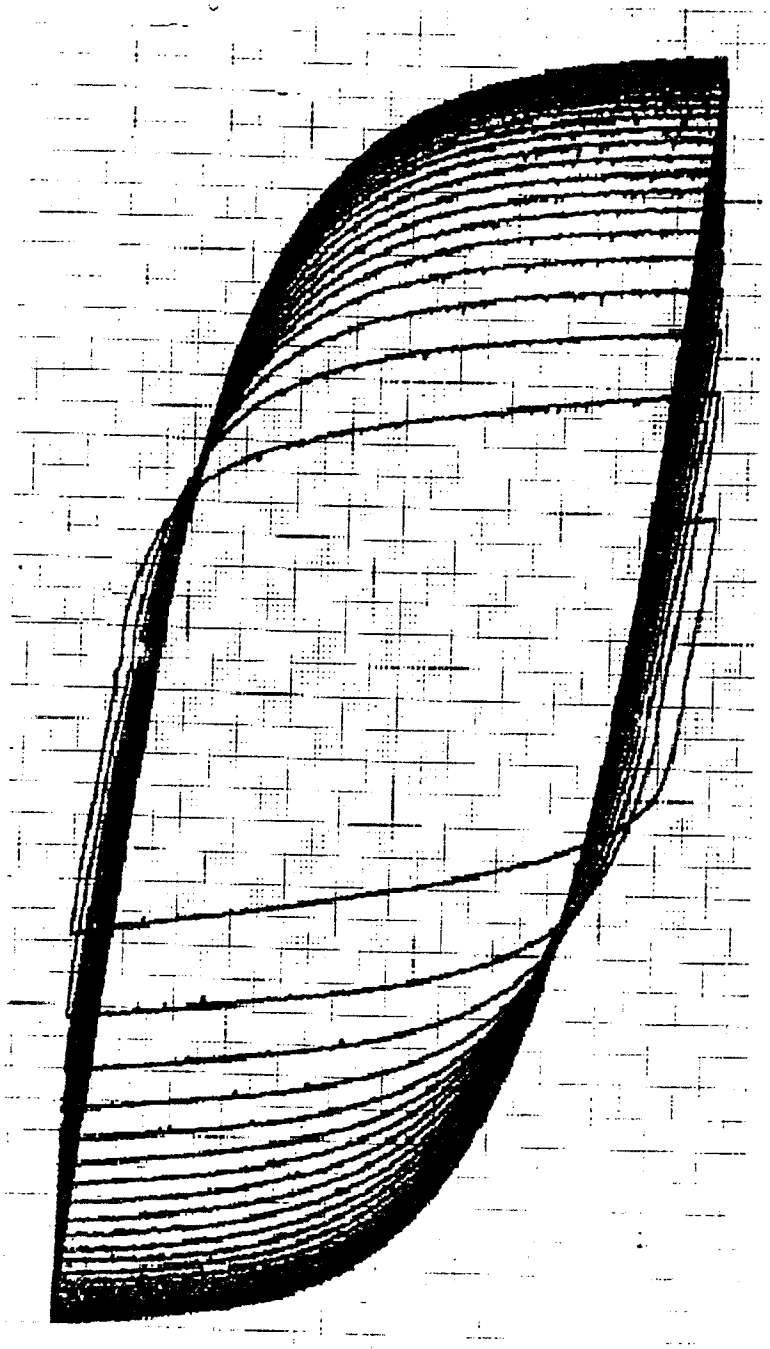

Figure 5.1 Stress-strain hysteresis loop ($\Delta\varepsilon_{pl}/2 = 4.38 \times 10^{-3}$, $\Delta\sigma_s/2 = 307$ MPa)

Specimen	*Input Values*		*Output Values*	
	$\Delta\varepsilon_t/2$	**Frequency (Hz)**	$\Delta\varepsilon_{pl}/2$	$\Delta\sigma_s/2$ **(MPa)**
Ni **8**	1.50E-03	0.067	4.25E-04	93.0
Ni **7**	2.20E-03	0.045	5.80E-04	121.5
Ni **10**	2.70E-03	0.037	7.76E-04	135.0
Ni **6**	3.10E-03	0.032	8.44E-04	148.0
Ni **5**	3.80E-03	0.026	1.22E-03	154.0
Ni **1**	4.20E-03	0.024	1.45E-03	156.0
Ni **4**	4.70E-03	0.021	1.54E-03	158.0
Ni **2**	5.40E-03	0.019	1.87E-03	189.2
Ni **16**	6.00E-03	0.017	2.02E-03	187.7
Ni **14**	8.00E-03	0.013	2.81E-03	211.4
Ni **15**	9.00E-03	0.011	3.64E-03	254.2
Ni **3**	1.10E-02	0.009	4.43E-03	269.0

Table 5.1 Fatigue test data for polycrystalline nickel

5.4 CYCLIC DEFORMATION BEHAVIOR

5.4.1 Cyclic Stress-Strain Curve

By plotting all saturation stress amplitudes, $\Delta\sigma_s/2$, as a function of plastic strain amplitudes, $\Delta\varepsilon_{pl}/2$, the cyclic stress-strain curve was obtained as shown in Figure 5.2. It is observed from the cyclic stress strain curve that the saturation stress increases with increasing $\Delta\varepsilon_{pl}/2$ up to plastic strain amplitude 8.44×10^{-4}, then the saturation stress levelled off at plastic strain amplitude from 1.22×10^{-3} to 1.54×10^{-3} in the quasi-plateau region. The saturation stress increased with plastic strain amplitude after plastic strain amplitude of 1.87×10^{-3} in the high amplitude range.

The cyclic stress strain curve of polycrystalline nickel obtained in this study is compared with the results of Morrison in reference 51 as shown in Figure 5.3. Cyclic hardening behaviour of polycrystalline nickel studied in the present work with grain size of 40 μm exhibits lower saturation stress than polycrystalline nickel with grain size of 24 μm. This difference in the cyclic behaviour would explain the effect of grain size on the cyclic saturation stress as predicted by a Hall-Petch type of argument, which results in a higher saturation stress with fine grain size. The grain structure effect on the saturation stress obtained in this study is in agreement with Morrison et al. findings [57]. However, this result is opposite to few of the previous findings [24,42,56].

A comparison of the cyclic stress strain response of polycrystalline aluminium and polycrystalline nickel with a grain size of 40 μm obtained in this study is shown in Figure 5.4. The cyclic deformation behaviour of polycrystalline aluminium exhibits lower saturation stress as compared to polycrystalline nickel over the plastic strain amplitude range studied. Such difference is due to the higher fatigue resistance offered by the nickel specimens as compared to aluminium specimens. In addition, Polycrystalline aluminium exhibits cyclic hardening at all plastic strain amplitudes, however polycrystalline nickel showed three distinct regions in the cyclic stress strain curve. This difference in the stress strain curve behaviour is due to high stacking fault energy of aluminium specimens (γ_{Al} =

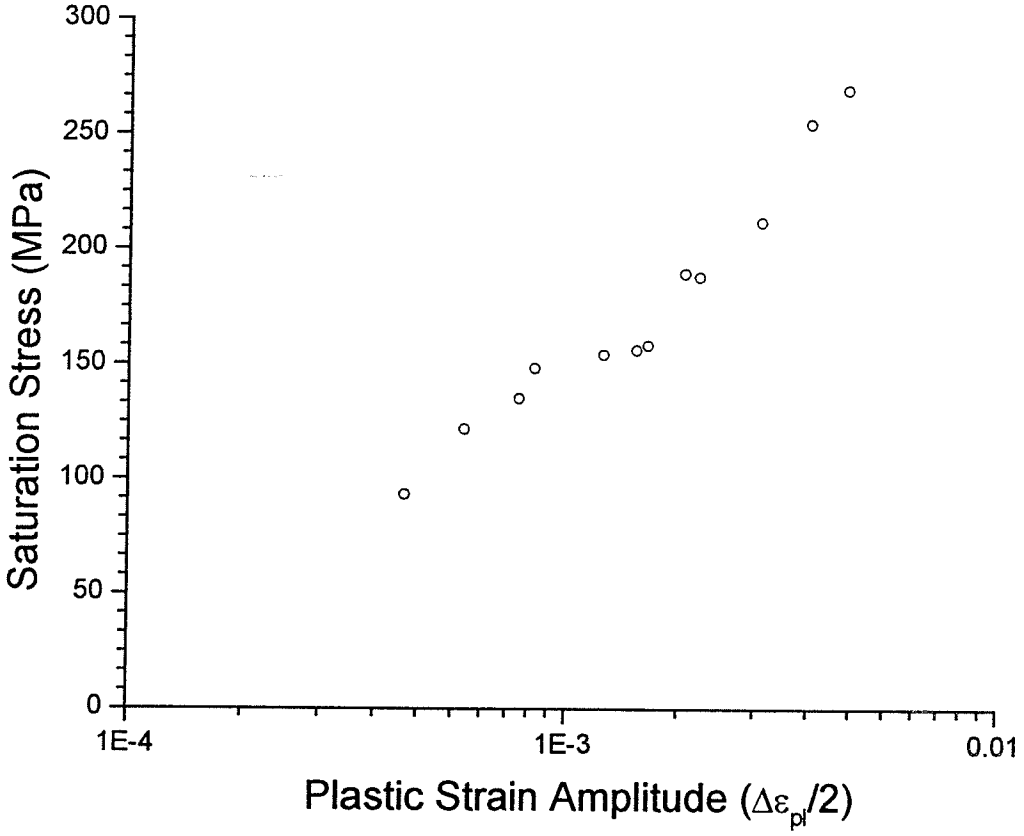

Figure 5.2 Cyclic stress-strain curve for polycrystalline nickel

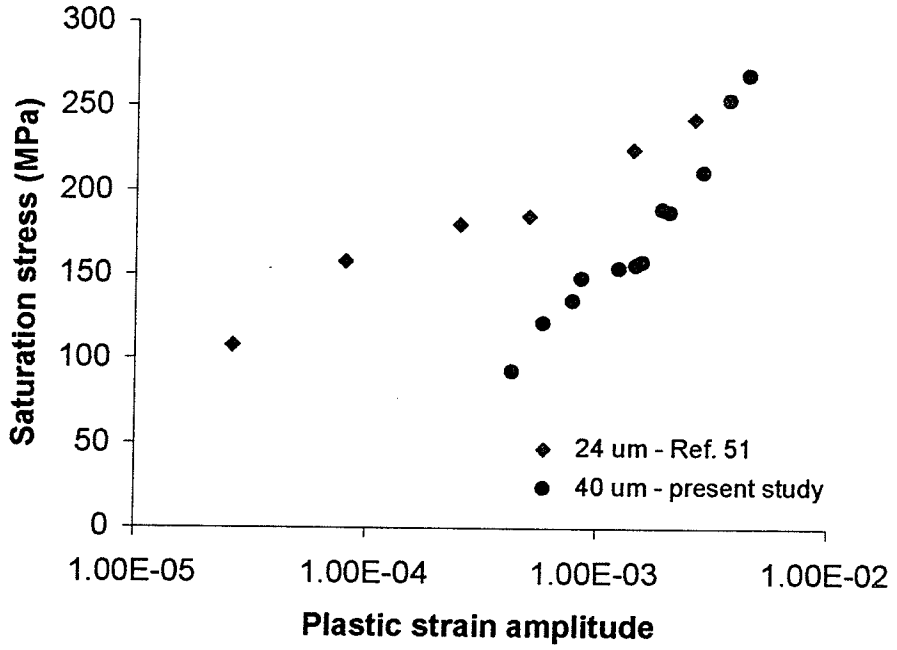

Figure 5.3 Cyclic stress-strain curve for polycrystalline nickel as compared to previous work from reference 51.

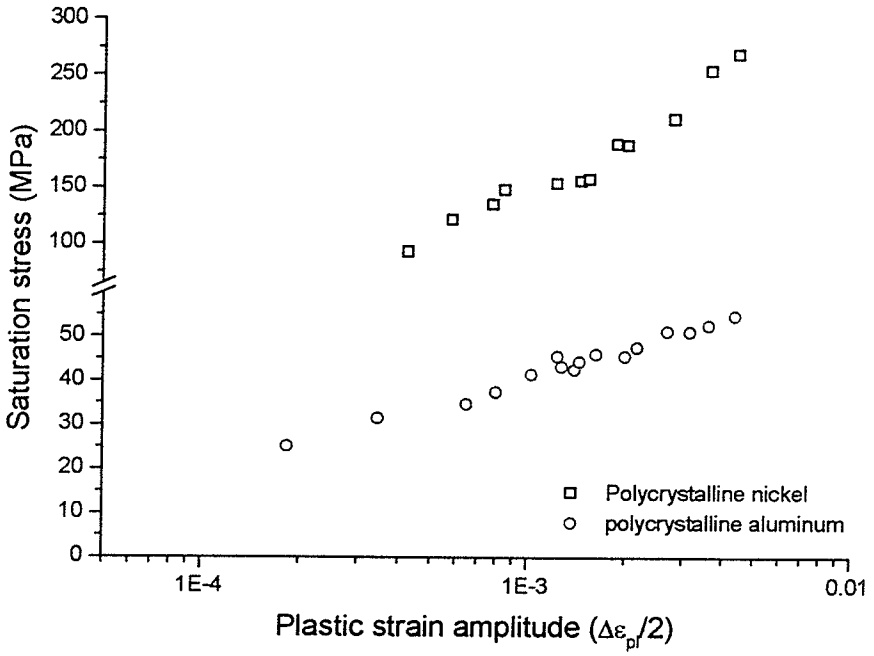

Figure 5.4 Comparison of cyclic stress-strain curve for polycrystalline nickel and polycrystalline aluminum

166 mJ m^{-2}) as compared to nickel specimens (γ_{Ni} = 128 mJ m^{-2}). Such high stacking fault energy would enhance the onset of multiple slip systems producing a three-dimensional dislocation network such as cell structure. Formation of a cellular structure leads to secondary hardening early in the fatigue cycles and at low plastic strain amplitudes.

5.4.2 Cyclic Hardening Curve

The material response to cyclic deformation as depicted by the cyclic hardening curve is shown in Figure 5.5 for specimen cycled at plastic strain amplitude 1.50 x 10^{-3}. Figure 5.6 is the cyclic hardening curve for specimen cycled at plastic strain amplitude 3.0 x 10^{-3}. It is observed from both figures that strain hardening was most pronounced in the early stage of cycling. After a large number of cycles (i.e. 180 cycles for specimen test at $\Delta\varepsilon_{pl}/2$ = 1.50 x 10^{-3} and 50 cycles for specimen test at $\Delta\varepsilon_{pl}/2$ = 3.0 x 10^{-3}), the strain hardening becomes saturated.

In agreement with prior work on polycrystalline copper [33], the results of the present study demonstrated that the initial cyclic hardening rate was strongly influenced by the plastic strain amplitude at which the test was performed. As shown in Figure 5.5 and Figure 5.6, the specimen cycled at plastic strain amplitude 3.0 x 10^{-3} exhibited 20% higher saturated stress than the specimen cycled at plastic strain amplitude 1.50 x 10^{-3}. In addition, it is also observed that the larger the plastic strain amplitude, the more pronounced the cyclic strain hardening, i.e. stress saturation is reached earlier in the fatigue cycle.

An initial rapid hardening stage followed by cyclic saturation characterizes the cyclic hardening curve. In the early stages of the rapid hardening, the dislocation density increases rapidly and many dislocation tangles and loops are formed. In the last stages of the rapid hardening and the early stages of the saturation hardening, the structures are divided into dislocation bundles and bundle spacing, which have a little dislocation and lie between the bundles. In the last stage of the saturation hardening, the bundles consist of many small dislocation loops and their spacings are as wide as the walls,

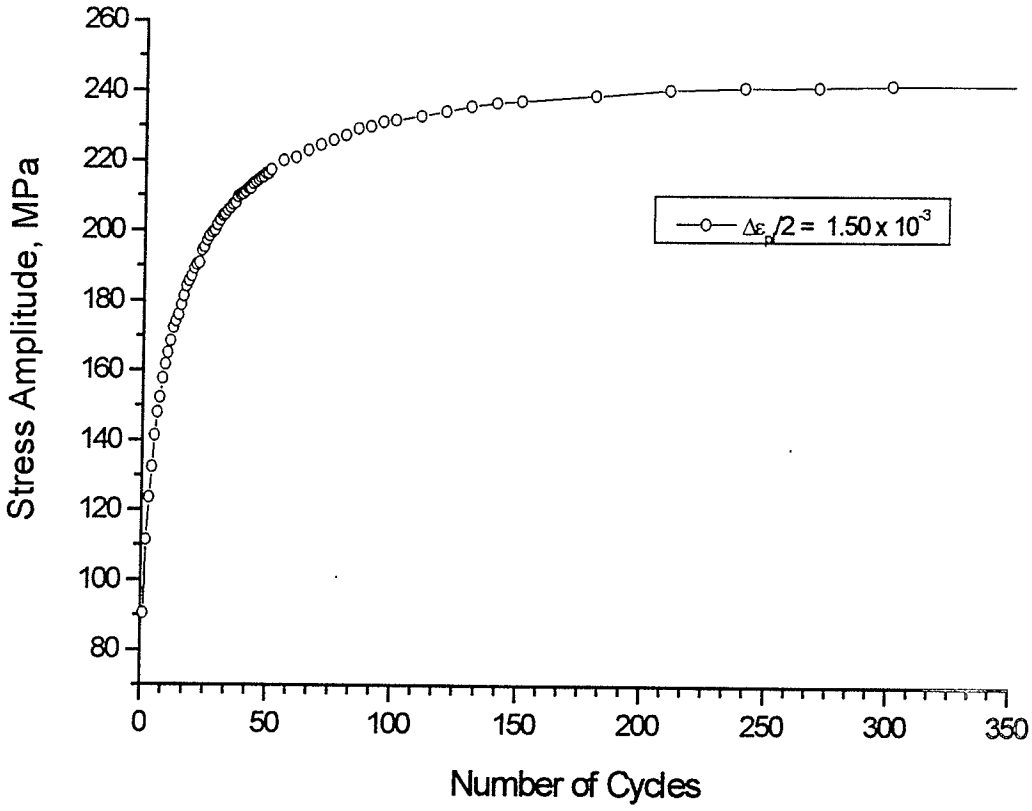

Figure 5.5 Cyclic hardening curve for polycrystalline nickel cycled at plastic strain amplitude of 1.50×10^{-3}. $\Delta\sigma_s/2 = 243$ MPa

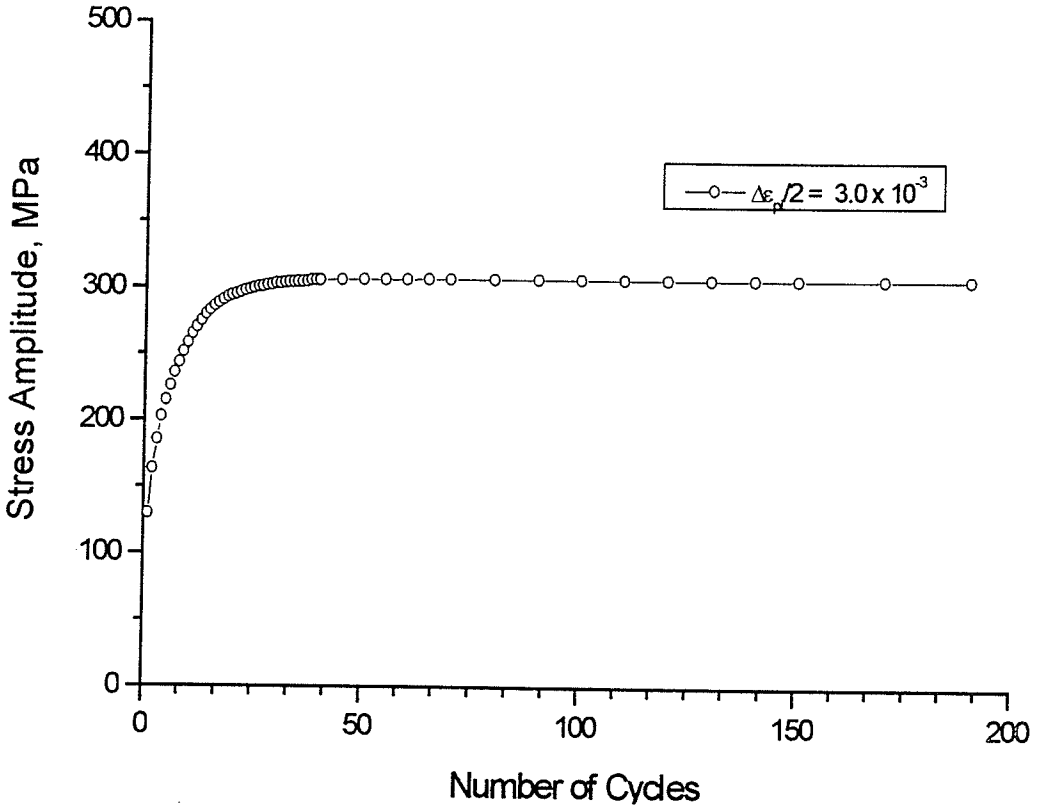

Figure 5.6 Cyclic hardening curve for polycrystalline nickel cycled at plastic strain amplitude of 3.0×10^{-3}. $\Delta\sigma_s/2 = 307$ MPa

which are called as loop patch structures or called vein structure composing of loop patches separated by dislocation-free channels.

5.5 MICROSTRUCTURAL OBSERVATIONS

5.5.1 Cyclic Deformation and Dislocation Structures Evolution

Three distinct regions were observed in the cyclic stress-strain response differing in both the dislocation structures and the stress-strain responses. In the low amplitude region ($\Delta\varepsilon_{pl}/2 < 8.44 \times 10^{-4}$), vein dislocation structures were observed in agreement with pervious observations on single crystals and polycrystals [16,79]. The slip within individual grains takes place in a single slip system, resulting in a multipole dislocation configuration, which forms the veins. Following the low amplitude region, a short quasi-plateau region with slight increase in the saturation stress with plastic strain amplitude occurred from plastic strain amplitude of 1.22×10^{-3} to 1.54×10^{-3}. In this region the vein structure is cut through by persistent slip bands, which have a characteristic ladder-like dislocation structure

The high amplitude region ($\Delta\varepsilon_{pl}/2 > 1.54 \times 10^{-3}$) is characterized by a number of structures depending on orientations of a grain and its neighbour. A very regular walls structure results from cyclic straining with the prevalence of a single slip system. Cell structures result if multiple slip systems are active. Such activation of multiple slip systems would lead to the activation of secondary slip systems within individual grains resulting to a build-up of the forest dislocation density and hence secondary hardening.

Three types of dislocation configuration were observed in polycrystalline nickel after cyclic deformation at plastic strain amplitude 1.50×10^{-3} to 300 fatigue cycles as shown in Figure 5.7. In this figure, vein structure can be seen, consisting of dense irregular regions of dislocation loop patches with narrow irregular channels, which have a relatively low dislocation density. The second structure has regions of two sets of dislocation wall perpendicular to each other called labyrinth structure. Also observed in

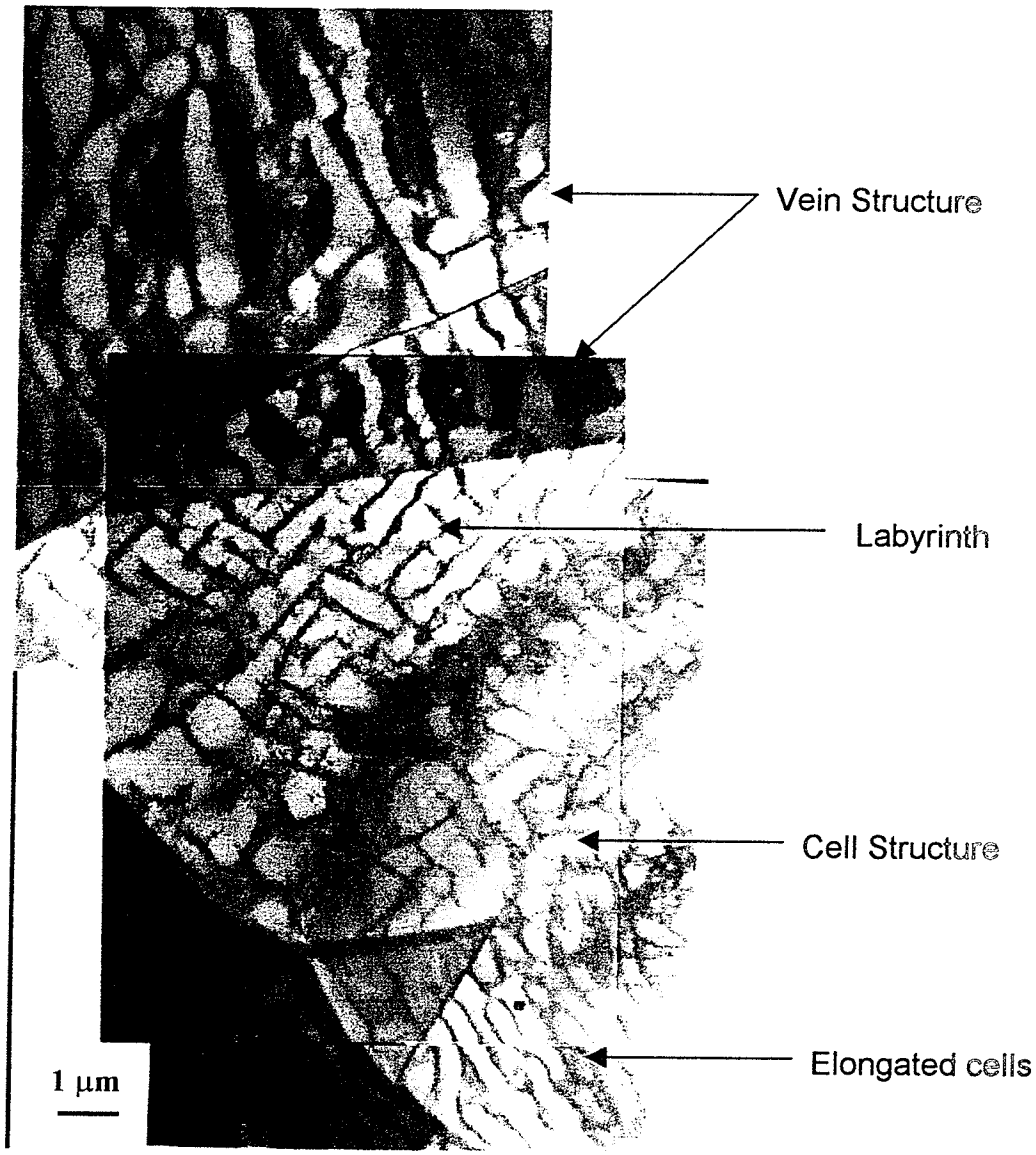

Figure 5.7 Dislocation structures formed in polycrystalline nickel cycled at plastic strain amplitude 1.50×10^{-3} to 300 cycles

this figure, cellular structure evolving from the labyrinth structure, which in turn evolves to elongated cells after a prolonged fatigue cycling.

In contrast to the early appearance of dislocation cell structure in polycrystalline aluminium at low plastic strain amplitudes, polycrystalline nickel exhibited the absence of cellular structure at low plastic strain amplitudes. Dislocation structure consisted of loop-patch/channel or vein structure was observed at low plastic strain amplitudes in the range of 4.25×10^{-4} to 8.44×10^{-4} as shown in Figures 5.8 to 5.11.

Since the loop patches are considered potent obstacles against glide dislocation motion, the more these patches the greater their density, and the imposition of a strain amplitude must open channels for the motion of the requisite glide dislocations. Cyclic hardening will result from the growth of the loop patches and the consequent decrease of the channel width. This hardening is observed in constant strain amplitude fatigue as an increase in the cyclic stress. The loop patches will eventually break into persistent slip bands (PSB's) with increase of stress.

The dislocation structure keeps evolving as the plastic strain increases. Loop patches become denser and the channels thinner, until another structure appears. This structure consists of bands about 1.2 microns wide, where plastic deformation is heavily localized. They are ladder-like structure called persistent slip band in which the density of dislocations is low in the middle of the PSB and very high at the walls. These bands are the main reason for the presence of the plateau.

Persistent slip bands (PSBs) were observed in cycled polycrystalline nickel at plastic strain amplitude of 1.22×10^{-3} as shown in Figures 5.12 to 5.14. However, these slip bands were short and not well developed as those observed in polycrystalline copper in previous studies [33]. The appearance of PSB in few areas of the specimen explains the minor effect of PSB on the cyclic deformation behaviour as depicted by the short quasi-plateau in the cyclic stress strain curve. The presence of short plateau in the cyclic stress

Figure 5.8 TEM image of longitudinal section of the specimen cycled at a plastic strain amplitude of 4.25×10^{-4} showing loop patches (dark phase) and matrix (light phase) forming vein structure. Wall spacing = 0.823 μm

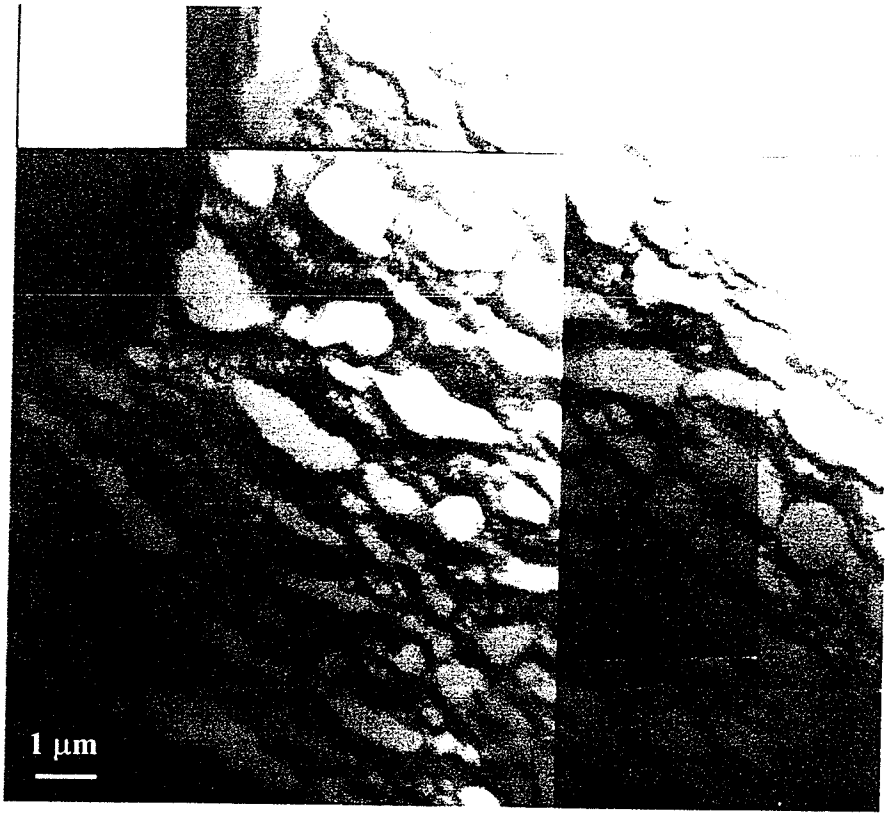

Figure 5.9 TEM image of longitudinal section of the specimen cycled at a plastic strain amplitude of 5.80×10^{-4} showing cylindrically shaped vein structure. Wall spacing = 0.733 μm

Figure 5.10 TEM image of longitudinal section of the specimen cycled at a plastic strain amplitude of 7.76×10^{-4} showing vein structure. Wall spacing = 0.609 μm

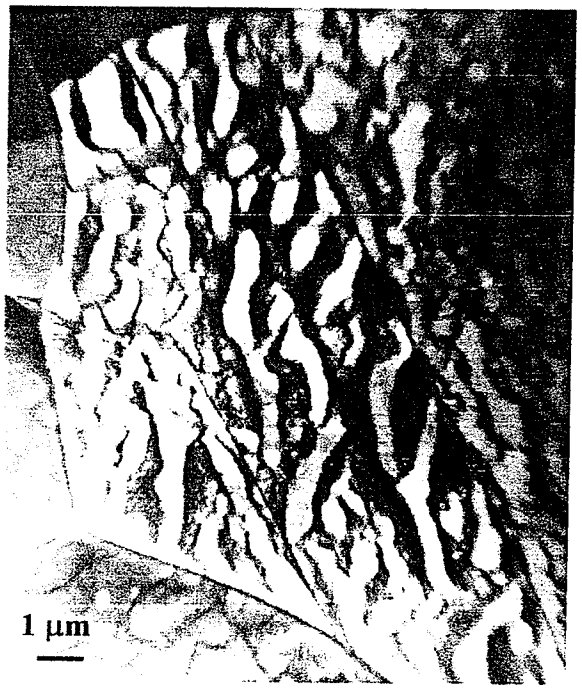

Figure 5.11 TEM image of longitudinal section of the specimen cycled at a plastic strain amplitude of 8.44×10^{-4} showing vein structure. Wall spacing = 0.519 μm

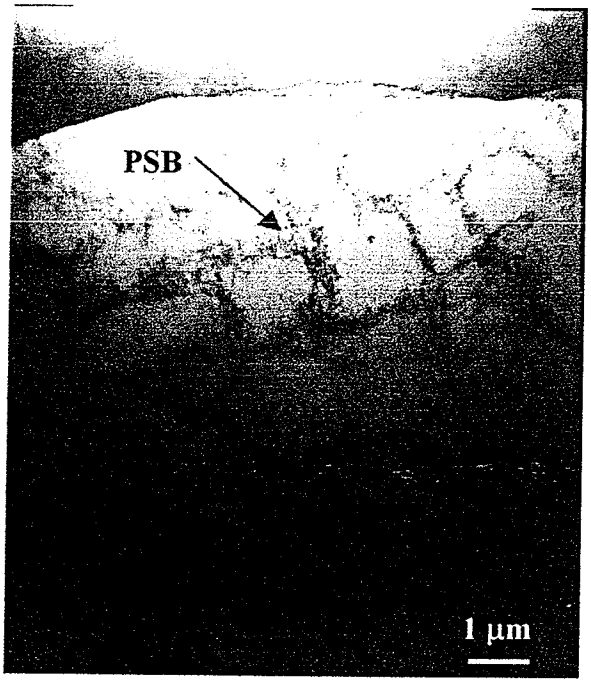

Figure 5.12 TEM image of longitudinal section of the specimen cycled at a plastic strain amplitude of 1.22×10^{-3} showing the presence of persistent slip band (PSB). Wall spacing = 1.2 μm

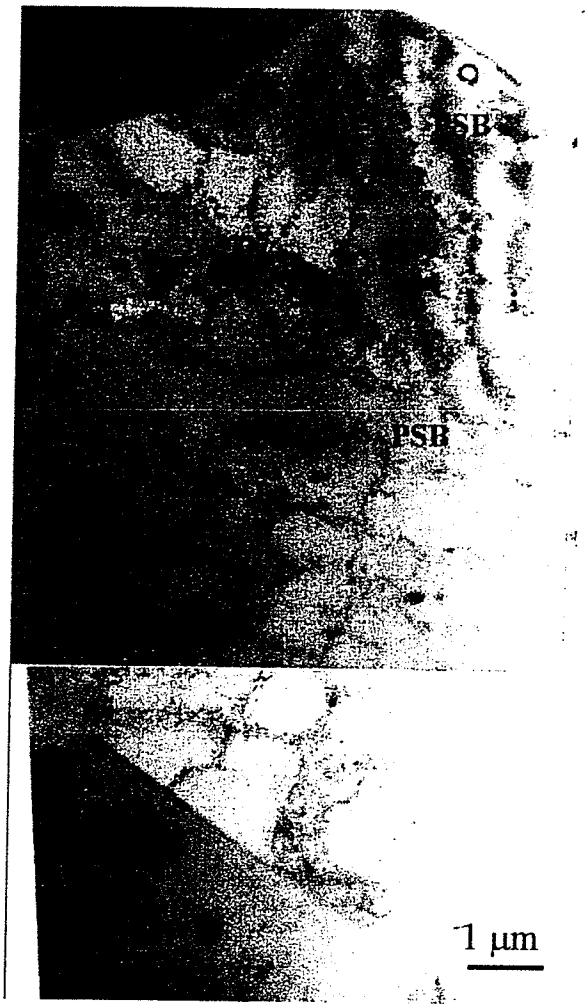

Figure 5.13 TEM image of longitudinal section of the specimen cycled at a plastic strain amplitude of 1.22×10^{-3} showing the presence of persistent slip bands (PSB) as indicated by arrows. Wall spacing = 1.2 μm

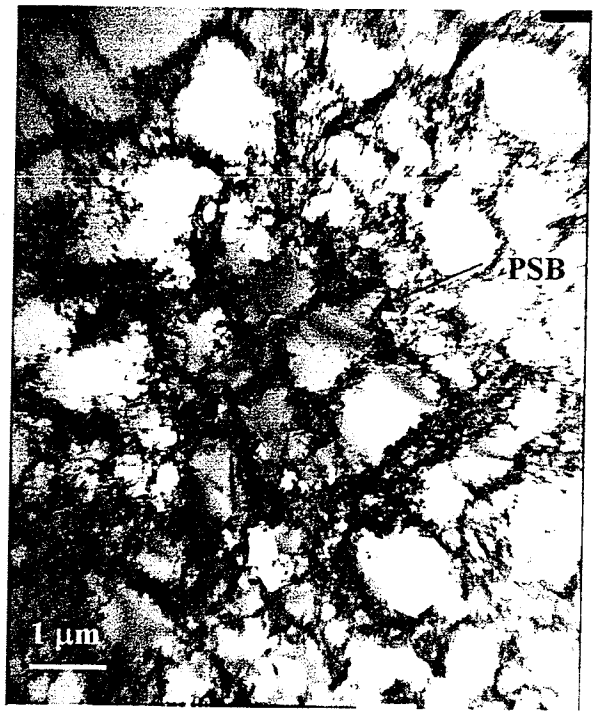

Figure 5.14 TEM image of longitudinal section of the specimen cycled at a plastic strain amplitude of 1.22×10^{-3} showing the presence of short persistent slip band (PSB). Wall spacing = 1.2 μm

strain curve for polycrystalline nickel agrees with the Morrison et al. [32] and Morrison [51] findings.

At high levels of plastic strain, PSB's and remaining vein structure break down as several slip systems need to be activated to carry out the plastic deformation, and the so called "multiple slip" dislocation structures appear such as labyrinth and cell structure. At a plastic strain amplitude of 1.45×10^{-3} labyrinth structure was observed along with the vein structure as shown in Figure 5.15. TEM micrograph of labyrinth structure is show in Figure 5.16 and Figure 5.17. The dislocation structure of the specimen cycled at plastic strain amplitude of 1.54×10^{-3} also showed vein structure along with labyrinth structure as shown in Figure 5.18.

With increasing strain amplitude, the dipolar walls of the labyrinth structures are still the predominant feature and present untill 1.54×10^{-3} strain. At applied strain of 1.87×10^{-3}, the labyrinth structure start to contain some cells, the path in the labyrinth structures is closed and the labyrinth evolves to square-shaped cellular structures. This implies that the third slip system is enhanced during the deformation causing the operation of multiple slip systems and the formation of three-dimensional dislocation network. Figure 5.19 is a TEM micrograph of specimen cycled at plastic strain amplitude of 1.87×10^{-3} showing the evolution of closed-path labyrinth structure to cell type of dislocation structure.

As the cells are much larger than the wall spacing, it would seem that they are not nucleated by individual walls. On the other hand, the presence of a sufficiently strong local surplus of dislocations of one type and sign, whether edge dislocation in the dipolar walls or screw dislocations in the channels, will trigger non-primary slip systems. This will give rise to dislocation cell formation as shown in Figure 5.20 for specimen cycled at plastic strain amplitude of 2.02×10^{-3}.

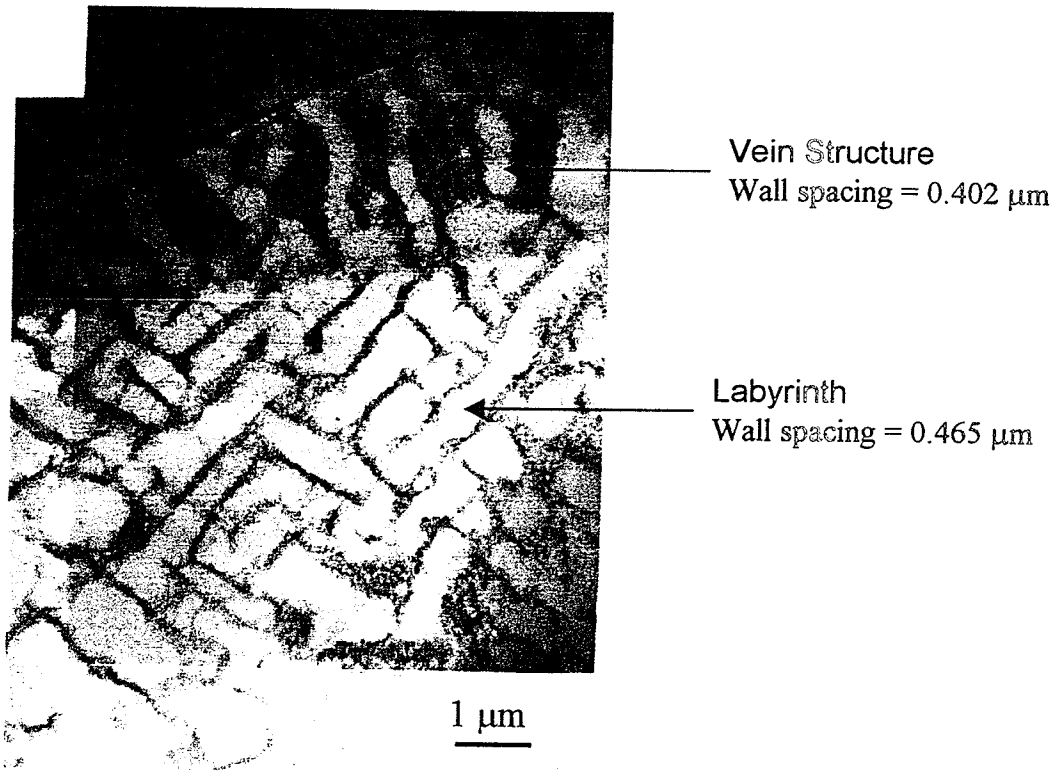

Figure 5.15 TEM image of longitudinal section of the specimen cycled at a plastic strain amplitude of 1.45×10^{-3} showing the evolution of vein structure to labyrinth structure.

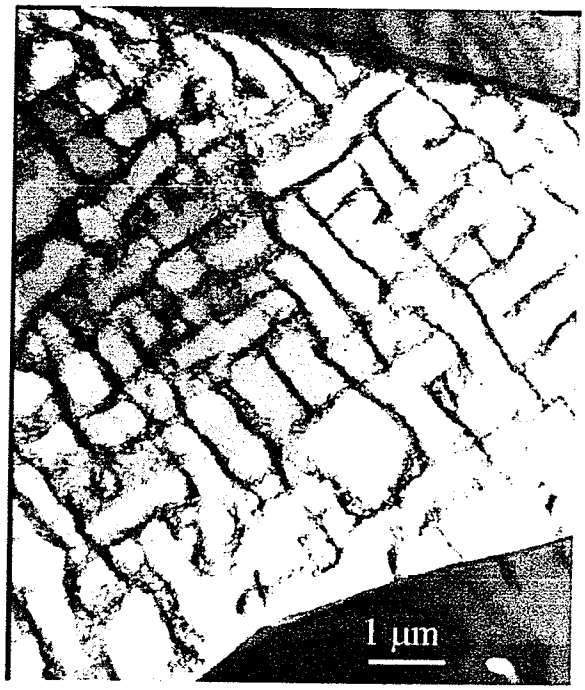

Figure 5.16 TEM image of closed-path labyrinth structure in longitudinal section of the specimen cycled at a plastic strain amplitude of 1.45×10^{-3}. Wall spacing = 0.465 μm

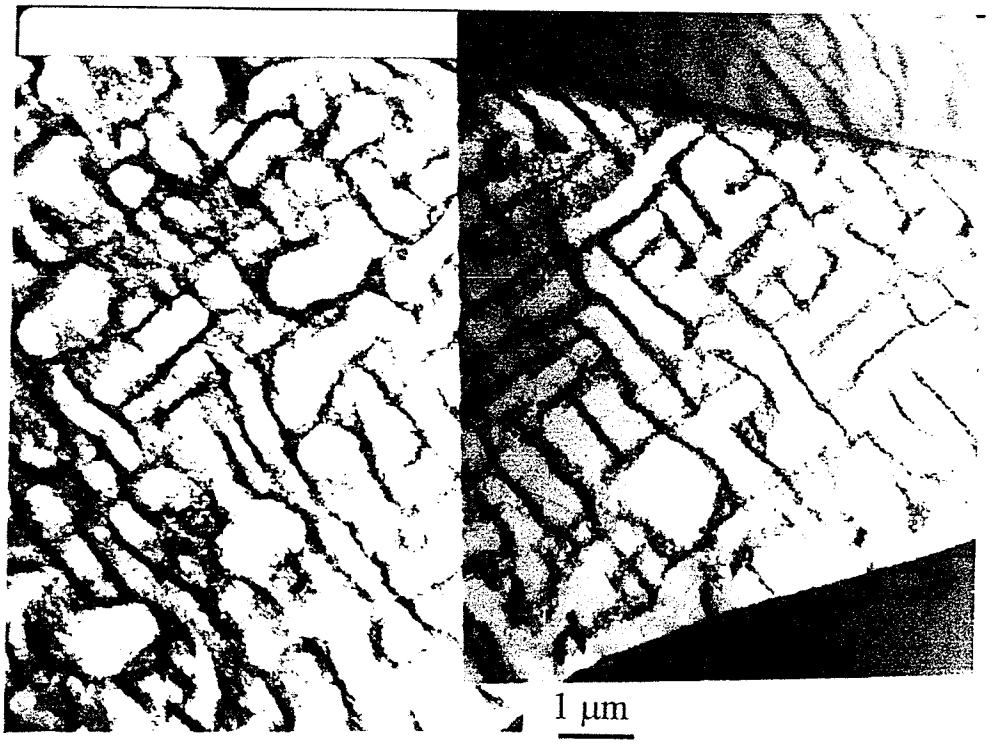

Figure 5.17 TEM image of closed-path labyrinth structure in longitudinal section of the specimen cycled at a plastic strain amplitude of 1.45×10^{-3}. Wall spacing = 0.465 μm

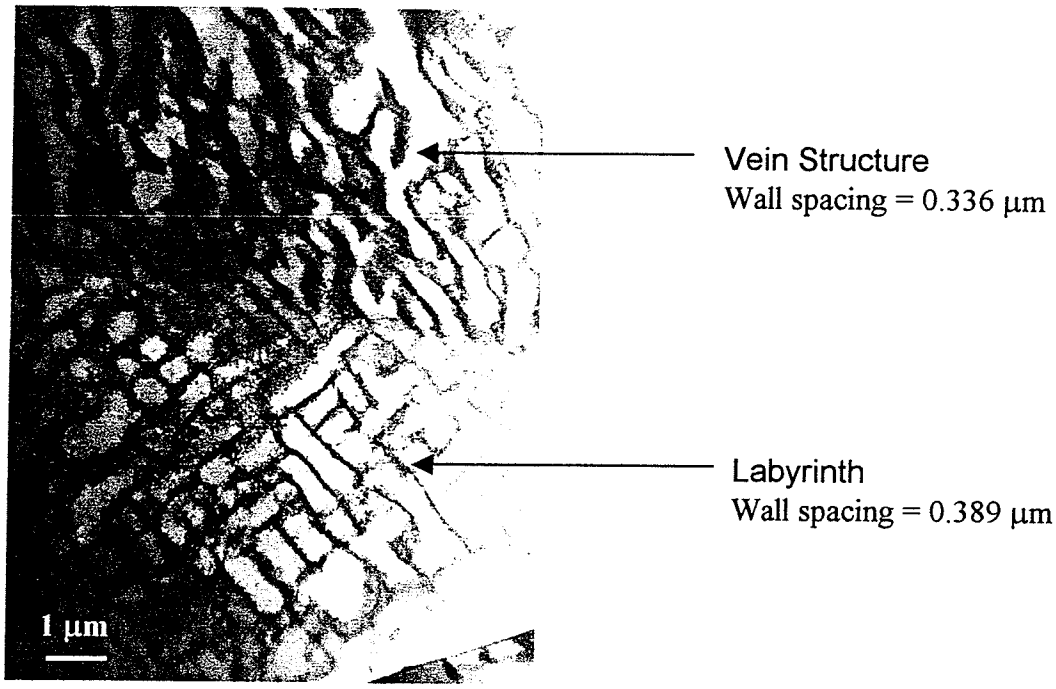

Figure 5.18 TEM image of longitudinal section of the specimen cycled at a plastic strain amplitude of 1.54×10^{-3} showing the evolution of vein structure to labyrinth structure.

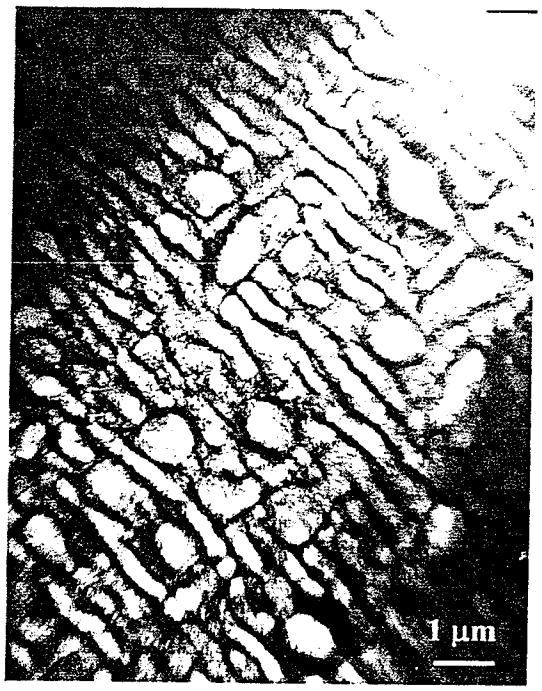

Figure 5.19 TEM image of longitudinal section of the specimen cycled at a plastic strain amplitude of 1.87×10^{-3} showing the evolution of labyrinth structure into cells Wall spacing = 0.313 μm. Cell Size = 0.757 μm.

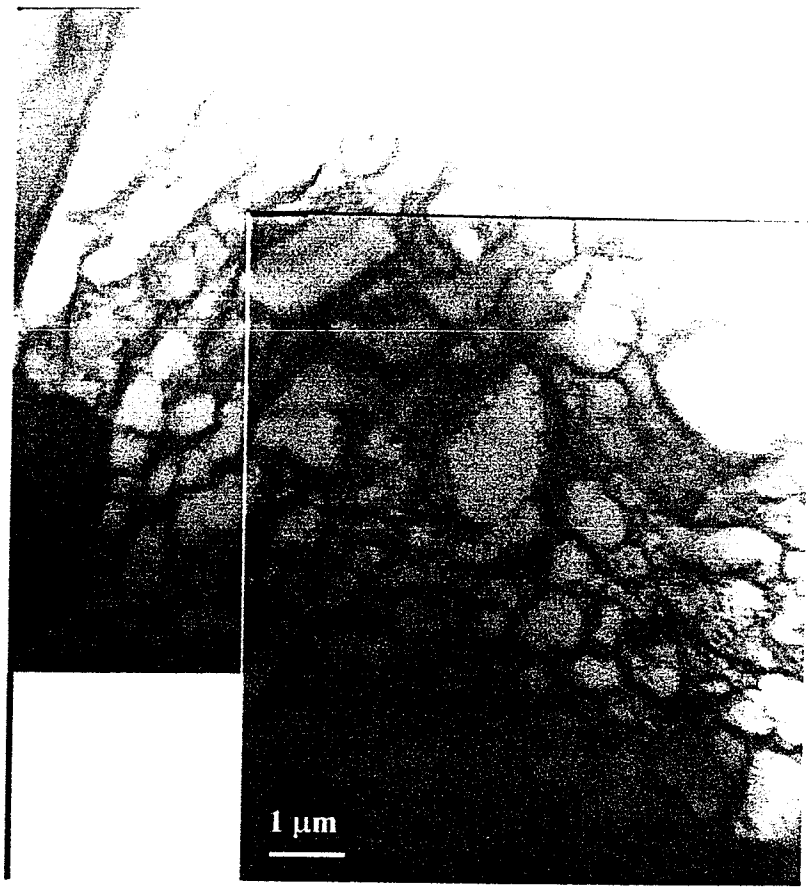

Figure 5.20 TEM image of dislocation cellular structure in longitudinal section of the specimen cycled at a plastic strain amplitude of 2.02×10^{-3}. Cell Size = 0.693 μm.

Figure 5.21 and Figure 5.22 are TEM micrographs of elongated cellular structure in a specimen cycled at plastic strain amplitude of 2.81 x 10^{-3}. As plastic strain amplitude is further increased, the width of the channels separating dislocation cellular structure becomes narrower producing elongated dipolar walls structure. A TEM micrograph of uncondensed dipolar wall structure is shown in Figure 5.23 for specimen cycled at plastic strain amplitude of 3.64 x 10^{-3}. Condensed dipolar wall structure was also found in specimen cycled at plastic strain amplitude of 4.43 x 10^{-3} as shown in Figure 5.24.

In summary, the dislocation structures formed in polycrystalline nickel after cyclic deformation have many different appearances like loop patches, vein and dipolar walls, when subjected to different strain amplitudes. These structures are formed from a similar dislocation deposition mechanism and are dipolized dislocation structures. Difference in appearance is the result of being condensed under different conditions.

Table 5.2 lists the dislocation structures and wall spacing formed under different plastic strain amplitudes. It is found that the average wall spacing between dislocation wall decreases with plastic strain amplitude. Figure 5.25 shows a linear relation between the average wall spacing and the cyclic saturation stress for both low amplitude and high amplitude ranges. An inverse relationship between the wall spacing and saturation stress is shown in Figure 5.26. This relationship is in agreement with mesh-length theory of work hardening discussed in chapter 4. The observed decrease in the average distance between the walls or the average cell diameter with increasing plastic strain amplitude (and saturation stress) is in agreement with previous observations [64].

The cycle number influence on the microstructure has been studied for a strain amplitude value of 3.0 E-03. Microscopy observations have been made after the following fatigue cycle number: 18, and 200. It was found that the cell structure becomes more equiaxed with increase in fatigue cycles as shown in Figure 5.27 and Figure 5.28.

5.6 SUMMARY

Cyclic stress-strain (CSS) curve of cyclically deformed polycrystalline nickel exhibited three distinct regions. Two cyclic hardening regions were observed at low amplitude and high amplitude ranges and short quasi-plateau region with a slight increase of saturation stress with plastic strain amplitude at intermediate amplitude range. A comparison of the cyclic stress-strain response of polycrystalline nickel with previous results revealed that fine-grain material exhibited higher saturation stress than coarse-grained material as predicted by a Hall-Petch relationship of grain size effect. A comparison of the cyclic stress-strain curve for both polycrystalline aluminum and nickel with grain size of 40 μm revealed that nickel specimens exhibited higher saturation stress than aluminum specimens due to the high fatigue resistance offered by the nickel specimens. In addition, the plastic strain amplitude at which the test was conducted influences cyclic hardening rate. It is found that saturation stress is reached earlier in fatigue cycle with high plastic strain amplitude.

Dislocation structures in fatigued polycrystalline nickel are amplitude dependent and are classified into three types of dislocation structures corresponding to the three regions in the cyclic stress-strain curve. Vein structures consisting of loop patches were observed at low strain amplitudes. These structures become mixed with labyrinth structure at intermediate amplitudes. In addition, persistent slip bands were observed in the quasi-plateau regions of CSS curve. Cellular structures were observed at higher amplitudes which become increasingly equiaxed and smaller with fatigue cycles. The results on the dislocation structure evolution found in this study are in agreement with most recent low cycle fatigue studies on polycrystalline nickel documented in reference 88 by Jia Yan.

A correlation between stress-strain response and development of dislocation structures in deformed polycrystalline nickel revealed that the saturation stress is linearly related to the inverse wall spacing. This relationship is equivalent to the mesh-length theory of work hardening over the strain range used in this study

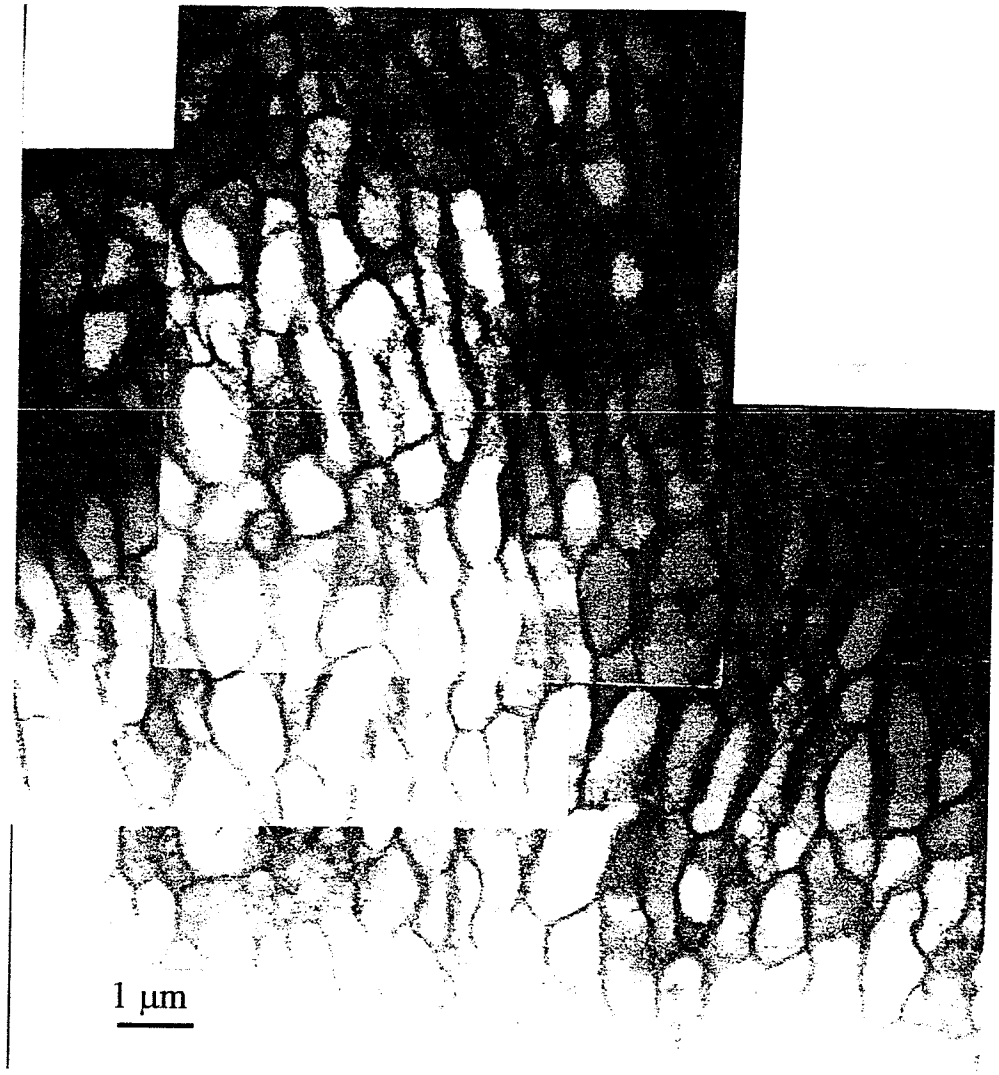

Figure 5.21 TEM image of elongated cellular structure in longitudinal section of the specimen cycled at a plastic strain amplitude of 2.81×10^{-3}. Wall spacing= 0.488 μm.

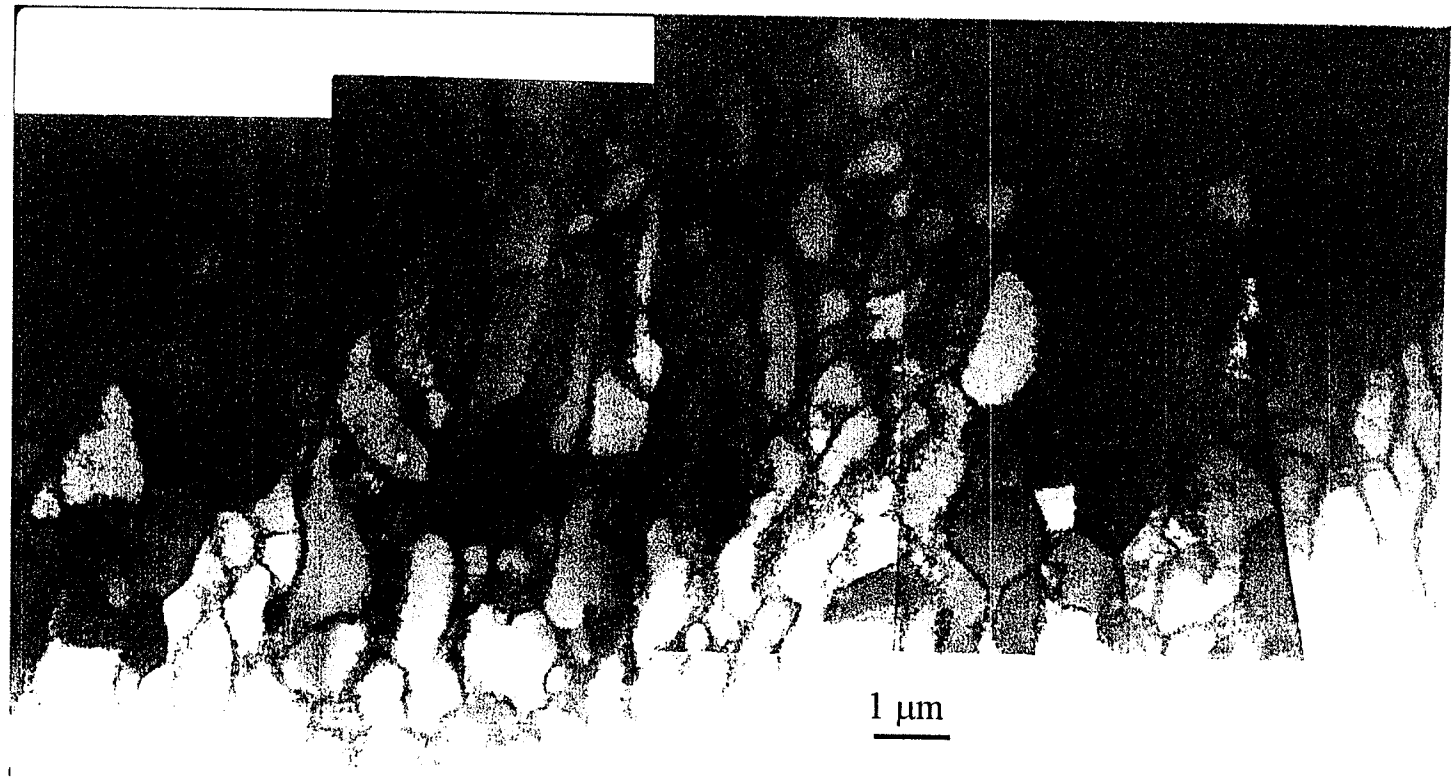

Figure 5.22 TEM image of elongated cellular structure in longitudinal section of the specimen cycled at a plastic strain amplitude of 2.81×10^{-3}. Wall spacing = 0.488 μm

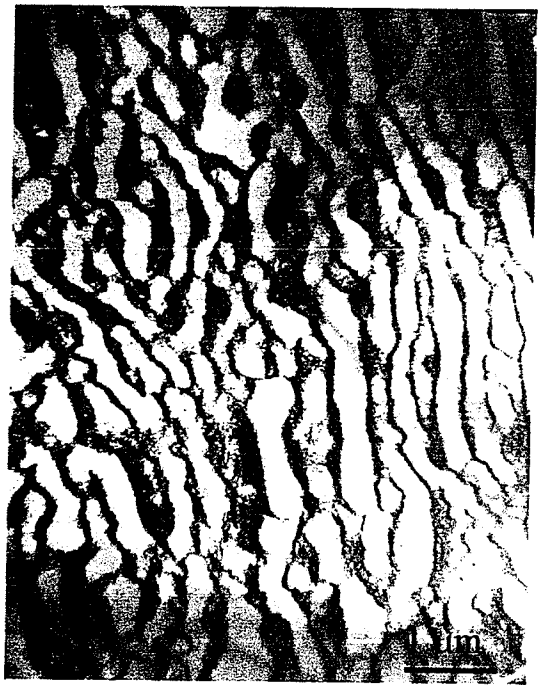

Figure 5.23 TEM image of uncondensed dipolar wall structure in longitudinal section of the specimen cycled at a plastic strain amplitude of 3.64×10^{-3} Wall spacing = 0.347 μm

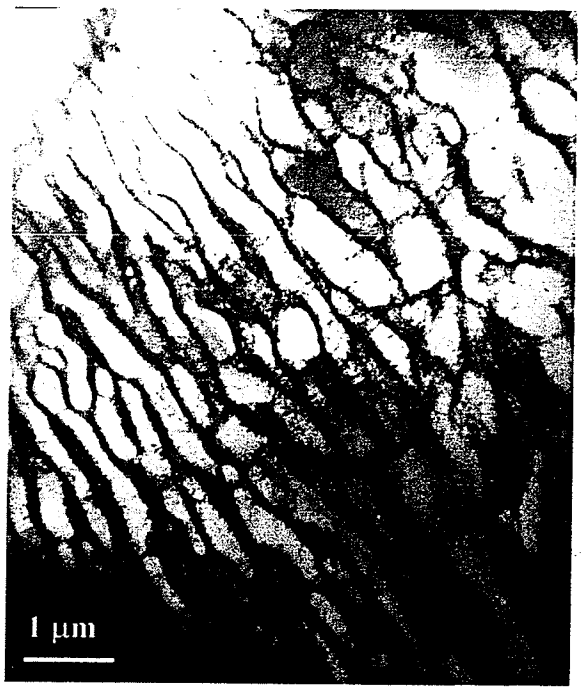

Figure 5.24 TEM image of condensed dipolar wall structure in longitudinal section of the specimen cycled at a plastic strain amplitude of 4.43×10^{-3}. Wall spacing = 0.268 μm

Plastic Strain Amplitude $\Delta\varepsilon_{pl}/2$	*Dislocation Structure*	*Wall Spacing* (μm)	*Reference*
4.25×10^{-4}	Loop Patch	0.823	Figure 5.8
5.80×10^{-4}	Loop Patch	0.733	Figure 5.9
7.76×10^{-4}	Loop Patch	0.609	Figure 5.10
8.44×10^{-4}	Loop Patch	0.519	Figure 5.11
1.22×10^{-3}	Persistent slip band	1.194	Figures 5.12 to 5.14
1.45×10^{-3}	Loop Patch	0.402	Figure 5.15 & 17
	Labyrinth	0.465	
1.54×10^{-3}	Loop Patch	0.336	Figure 5.18
	Labyrinth	0.389	
1.87×10^{-3}	Labyrinth	0.313	Figure 5.19
	Cells	0.757	
2.02×10^{-3}	Cells	0.693	Figure 5.20
2.81×10^{-3}	Elongated cells	0.488	Figure 5.21 & 22
3.64×10^{-3}	Dipolar wall structure	0.347	Figure 5.23
4.43×10^{-3}	Dipolar wall structure	0.268	Figure 5.24

Table 5.2 Dislocation structures in polycrystalline nickel observed at different plastic strain amplitudes

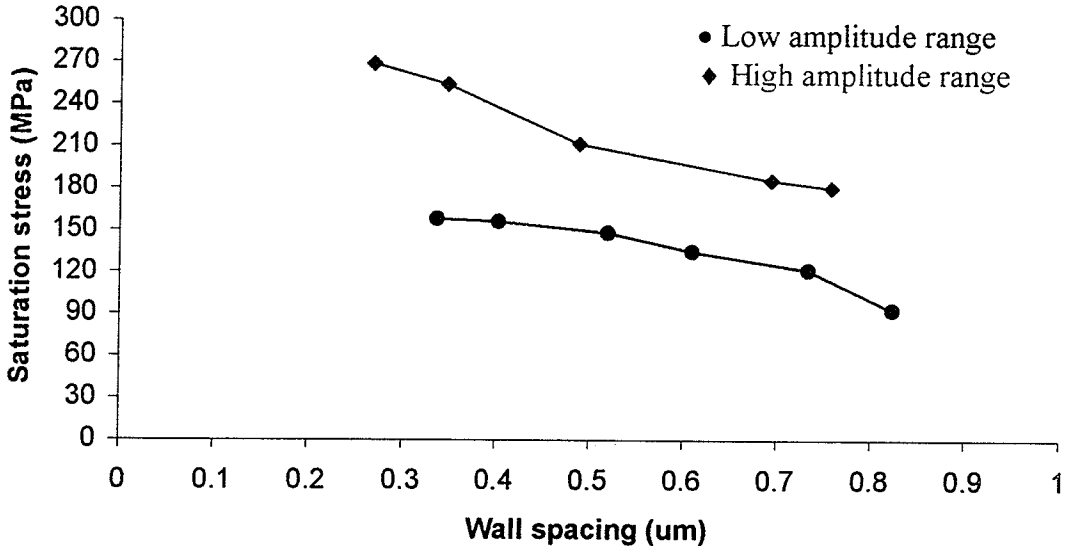

Figure 5.25 Relationship between saturation stress and wall spacing for polycrystalline nickel

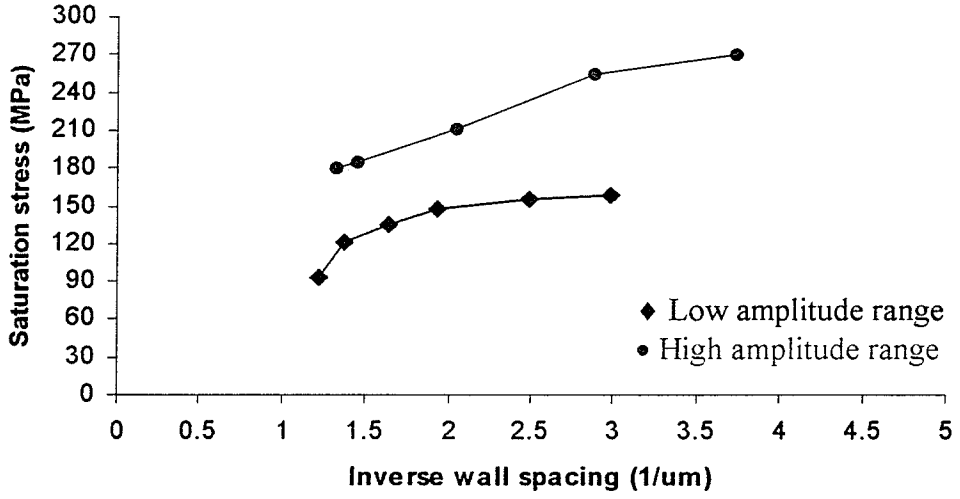

Figure 5.26 Relationship between saturation stress and inverse wall spacing for polycrystalline nickel

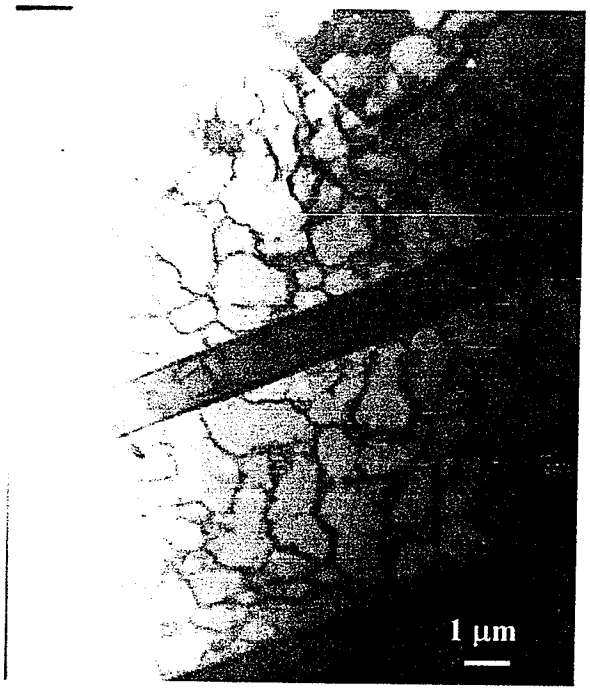

Figure 5.27 TEM image of dislocation cellular structure in longitudinal section of the specimen cycled at a plastic strain amplitude of 3.0×10^{-3} to 18 cycles.

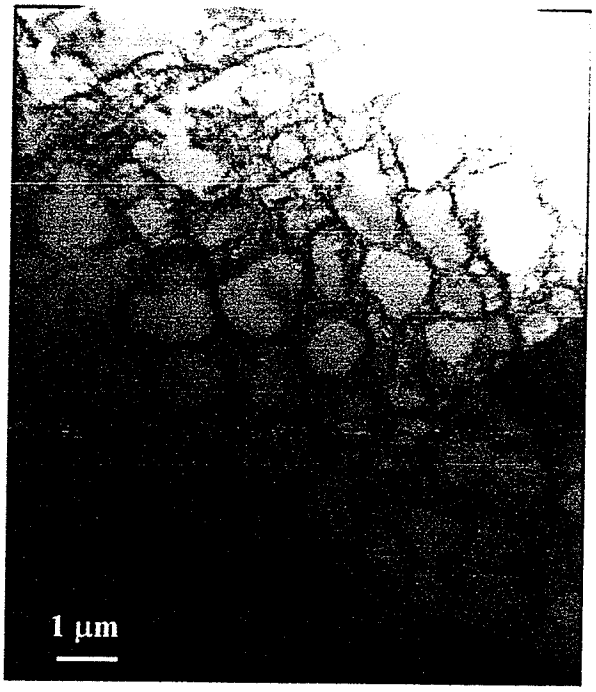

Figure 5.28 TEM image of longitudinal section of the specimen cycled at a plastic strain amplitude of 3.0×10^{-3} to 100 cycles showing equiaxed cellular structure

CHAPTER SIX: CONCLUSIONS

The fundamental objective of the present thesis was to study cyclic deformation behavior and to characterize the development of dislocation structures in cyclically deformed polycrystalline aluminum and nickel. The study revealed significant findings regarding the difference in cyclic deformation behavior in f.c.c. metals. The evolution and role of dislocation structures in plastic deformation were investigated and correlated to the cyclic deformation response. The following are the conclusions of the present thesis:

1. Results obtained from low cycle fatigue testing on polycrystalline aluminum and polycrystalline nickel led to the following conclusions concerning cyclic stress-strain (CSS) response:

   - Polycrystalline aluminum exhibited cyclic hardening at which saturation stress increased with plastic strain at all plastic strain amplitudes tested.

   - Cyclic stress-strain response of polycrystalline nickel showed the presence of three distinct regions. These regions are two cyclic hardening regions at low amplitude and high amplitude ranges and a short quasi-plateau region with a slight increase of saturation stress with plastic strain amplitude at intermediate amplitude ranges.

   - A comparison of the cyclic stress-strain curve for both polycrystalline aluminum and nickel with grain size of 40 μm revealed that nickel specimens exhibited higher saturation stress than aluminum specimens due to the high fatigue resistance offered by the nickel specimens.

   - A comparison of the cyclic stress-strain response of polycrystalline aluminum and nickel with previous results revealed that fine-grain material exhibited higher saturation stress than coarse-grained material which is equivalent to the Hall-Petch relationship of grain size effect.

- Cyclic hardening rate is influenced by the plastic strain amplitude at which the test was conducted. It is found that the larger the plastic strain amplitude, the more pronounced the cyclic strain hardening. As a result, saturation stress is reached earlier in a fatigue cycle with high plastic strain amplitude.

2. The dislocation structures in fatigued polycrystalline aluminum and nickel with grain size of 40 μm were evaluated over the plastic strain amplitudes tested. Based on TEM observations of dislocation structures, the following conclusions can be drawn:

   - Dislocation structures in fatigued polycrystalline nickel are amplitude dependent and are classified into three types of dislocation structures in the strain range from 4.25E-04 to 4.43E-03, which correspond to the three regions in the cyclic stress-strain curve.

   - In deformed polycrystalline nickel, vein structures consisting of loop patches were observed at low strain amplitudes. These structures become mixed with labyrinth structure at intermediate amplitudes. In addition, persistent slip bands (PSB's) were observed in the quasi-plateau regions of CSS curve. At higher amplitudes cellular structures formed which become increasingly equiaxed and smaller with increase of amplitude and fatigue cycles.

   - There is a continual increase in the propensity for cell structure formation in polycrystalline aluminum with plastic strain amplitude and fatigue cycle number. TEM observations revealed that only cell structure is the dominant deformation structure in deformed polycrystalline aluminum. Compared with copper and nickel polycrystals, PSB and labyrinth structures have not been observed in fatigued pure aluminum. This behavior is due to the high stacking fault energy of aluminum polycrystals as compared to copper and nickel polycrystals. The high value of stacking fault energy favors the activation of multiple glide systems and formation of three-dimensional dislocation structure, which results in cyclic hardening with plastic deformation.

- According to the increasing strain amplitude, some common characteristics can be derived from TEM micrographs concerning dislocation cellular structure observed in deformed polycrystalline aluminum:

  1) cell walls are essentially composed of entangled dislocations.
  2) dislocation cellular structure becomes more or less well condensed as the plastic strain amplitude increases.
  3) cells are more equiaxed as plastic strain amplitudes and fatigue cycles increase.
  4) cell wall thickness decreases with increasing plastic strain amplitude

3. A correlation between stress-strain response and development of dislocation structures in deformed polycrystalline aluminum and nickel revealed that the saturation stress is linearly related to the inverse dislocation cell size and wall spacing. This relationship is equivalent to the mesh-length theory of work hardening over the strain range used in this study

4. This study revealed the significance of material characteristics such as stacking fault energy on the cyclic deformation behavior. It was found that high stacking fault energy influences the evolution of dislocation structure with plastic deformation and hence influences the cyclic deformation response. As a result polycrystalline aluminum with high value of stacking fault energy exhibited a different cyclic deformation behavior and different dislocation structures than polycrystalline nickel and copper.

5. The influence of material characteristics, grain size and pre-loading history on low cycle fatigue response of polycrystalline f.c.c. metals is still subject to a debate and investigation. As summarized in chapter 2, the literature review section, many researchers studied low cycle fatigue on polycrystalline metals and alloys under different testing parameters and revealed different deformation behaviors. Such investigation of these parameters on cyclic deformation requires extensive microscopy analysis and modeling of the micro-scale dislocation structures.

REFERENCES

[1] M.N. Bassim, C.D. Liu, Strength of Metals, Japan Inst. Metals (1994).

[2] H. Mughrabi, Strength of Metals and Alloys, vol. 3, (1985) p. 1917.

[3] Manual on Low Cycle Fatigue Testing, ASTM RTP.

[4] Jo Dean Morrow, ASTM STP 378 (1964) 45.

[5] ASM, Metals Handbook Desk Edition Eight, 8 (1985).

[6] ASM, Fatigue and Microstructure, Metals Park, Ohio (1979).

[7] C.E. Feltner, Phil. Mag. 12 (1965) 1229.

[8] J.R. Hancock, J.C. Grosskreutz, Acta Mater. 17 (1969) 77.

[9] A.T. Winter, Phil. Mag. 30 (1974) 411-417.

[10] P.J. Woods, Phil. Mag. 28 (1973) 155-193.

[11] S.J. Basinski, Z.S. Basinski, A. Howie, Phil. Mag. 19 (1969) 899-924.

[12] J.G. Antonopoulos, A.T. Winter, Phil. Mag. 33 (1976) 87-95.

[13] J.M. Finney, C. Laird, Phil. Mag. 31 (1975) 339.

[14] H. Mughrabi, R. Wang, K. Differt, U. Essmann, in Fatigue Mechanisms – Advances in Quantitative Measurement of Physical Damage, ASTM STP 811, 1983 pp. 5-45.

[15] H. Mughrabi, Mater. Sci. Eng. 33 (1978) 207-223.

[16] H. Mughrabi, F. Ackermann, K. Herz, in: J.T. Fong (Ed.), Fatigue Mechanisms, Proc. ASTM-NBS-NSF Symp., ASTM STP 675, American Society for Testing and Materials, Philadelphia, PA, 1979, pp. 69-105.

[17] C.D. Liu, D.X. You, M.N. Bassim, Acta Mater. 42 (5) (1994) 1631-1638.

[18] A.T. Winter, Phil. Mag. 30 (1974) 719-738.

[19] C.D. Liu, M.N. Bassim, D.X. You, Acta Mater. vol. 42, No. 11 (1994) pp. 3695-3704.

[20] K.V. Rasmussen, O.B. Pedersen, Acta Mater. 28 (1980) 1467-1478.

[21] S.P. Bhat, C. Laird, Scr. Metall. 12 (1978) 687-692.

[22] V. Kuokkala, P. Kettunen, Acta Mater. 33 (1985) 2041-2047.

[23] C. Laird, L. Buchinger, Metall. Trans. 16A (1985) 2201-2214.

[24] P. Lukas, L. Kunz, Mater. Sci. Eng. 74 (1985) L1-L5.

[25] A. Giese, A. Styczynski, Y. Estrin, Mater. Sci. Eng. A124 (1990) L11-L13.

[26] H. Mughrabi, R. Wang, in: N. Hansen, A. Horsewell, T. Leffers, H. Lilholt (Eds.), Deformation of Polycrystals, Mechanisms and Microstructures, Proc. of 2nd Riso Intern. Symp. on Metallurgy and Materials Science, Riso National Laboratory, p.87, (1981), pp. 87-98.

[27] H. Mughrabi, Scr. Metall. 13 (1979) 479-484.

[28] P. Kettunen, T. Tiainen, in: N. Hansen, A. Horsewell, T. Leffers, H. Lilholt (Eds.), Deformation of Polycrystals, Riso, Denmark 1981 pp. 437-44.

[29] P. Kettunen, T. Tiainen, Proc. of the 2nd Riso Intern. Symp. on Metallurgy an Material Science, vol. 1, Netherlands (1978) pp. 207-223.

[30] K.V. Rasmussen, O.B. Pedersen, Cyclic Deformation of Copper Polycrystals, vol. 2, Roskilde, Denmark (1979) pp. 1219-1223.

[31] H. Mughrabi, Dislocation and Properties of Real Materials (Conf. Proc.), Book No. 323, the Institute of Metals, London 1985 p. 244.

[32] D.J. Morrison, V. Chopra, Mater. Sci. Eng. A177 (1994) 29-42.

[33] J. Polak, K. Obrtlik, M. Hajek, A. Vasek, Mater. Sci. Eng. A151 (1992) 19-27.

[34] K. Mecke, C. Blochwitz, Cryst. Res. Technol. 17 (1982) 743-758.

[35] C. Blochwitz, U. Veit, Cryst. Res. Technol. 17 (1982) 529-551.

[36] P. Li, N.J. Marchand, B. Ilschner, Elsevier Applied Science, (1987) pp. 55-64.

[37] Jo-Chi Tsou, Ph. D. Thesis, University of Rochester, Rochester, New York, 1982.

[38] G. Guichon, J. Chicois, C. Esnouf, R. Fougeres, in: C.J. Beevers (Ed.), FATIGUE 84, vol. 1, 1984 pp. 31-40.

[39] P. Charsley, L.J. Harris, Scr. Metall. 21 (1987) 341-344.

[40] N. Marchand, J.P. Bailon, J.I. Dickson, Defects, Fracture and Fatigue, Proc. 2nd Intern. Symp., Mont. Gabriel, Canada (edited by G.C. Sih and J.W. Provan), Martinus Nijhoff, The Hague (1984) p. 195.

[41] J.C. Figueroa, S.P. Bhat, R. de la Veaux, S. Murzenski, C. Laird, Acta Mater. 29 (1981) 1667-1678.

[42] L. Llanes, C. Laird, Mater. Sci. Eng. A128 (1990) L9-L12.

[43] B.D. Yan, A. Hunsche, P. Neumann, C. Laird, Mater. Sci. Eng. 79 (1986) 9.

[44] B.D. Yan, C. Laird, Mater. Sci. Eng. 80 (1986) 59.

[45] P. Neumann, Z. Metallkde 59 (1968) 927.

[46] Z. Wang, C. Laird, Mater. Sci. Eng. 100 (1988) 57-68.

[47] P. Lukas, L. Kunz, B. Weiss, R. Stickler, W. Hessler, Mater. Sci. Eng. A118 (1989) L1.

[48] C.D. Liu, M.N. Bassim, phys. stat. sol. (a) 149 (1995) 323.

[49] T.L. Johnston, C.E. Feltner, Metall. Trans. 1 (1970) 1161-1167.

[50] L. Llanes, Ph.D. Dissertation, University of Pennsylvania, 1992.

[51] D.J. Morrison, Mater. Sci. Eng. A187 (1994) 11-21.

[52] H. Mughrabi, R. Wang, in: P. Lukas, J. Polak (Eds.), Materials Science Monographs, vol. 46, Basic Mechanisms in Fatigue of Metals, Elsevier, Amsterdam 1988, pp. 1-14.

[53] R. Wang, H. Mughrabi, Mater. Sci. Eng. 63 (1984) 147-163.

[54] V.T. Kuokkala, T. Lepisto, P. Kettunen, Scr. Metall. 16 (1982) 1149-1152.

[55] P. Lukas, L. Kunz, Mater. Sci. Eng. 85 (1987) 67-75.

[56] S. Horibe, Jia-Kuen Lee, C. Laird, Fatigue of Engineering Structures and Materials, 7 (1984) 145-154.

[57] D.J. Morrison, V. Chopra, J.W. Jones, Scr. Metall. 25 (1991) 1299-1304.

[58] R.C. Boettner, C. Laird, A.J. McEvily, Metall. Trans. Soc. AIME, 223 (1965) 379.

[59] A.W. Thompson, W.A. Backofen, Acta Mater. 19 (1971) 597.

[60] Y.B. Xia, Z.G. Wang, R.H. Wang, phys. Stat. sol. (a) 120 (1990) 125-132.

[61] Y.B. Xia, Z.G. Wang, S.H. Ai, Acta Mater. Sinica 18 (1982) 606.

[62] Z.G. Wang, T.B. Hu, Y.B. Xia, Q.B. Yang, Chin. J. Met. Sci. Technol. 2 (1986) 367.

[63] Z.G. Wang, Y.B. Xia, Proc. 5th Intern. Conf. Mechanical Behavior of Materials, Beijing, vol. 1, in: M.G. Yan, S.H. Zhang, Z.M. Zheng (Eds.), Pergamon Press. Oxford (1987) p. 609.

[64] C.E. Feltner, C. Laird, Acta Metall. 15 (1967) 1633.

[65] J.C. Grosskreutz, J. Appl. Phys. 34 (1963) 372.

[66] J.T. McGrath, W.J. Bratina, Phil. Mag. 12 (1965) 1293.

[67] C.E. Feltner, Phil. Mag. 8 (1963) 2121.

[68] G. Waldron, Acta Mater. 13 (1965) 897.

[69] P. R. Strutt, J. Australian Inst. Met. 8 (1963) 115.

[70] H. Mughrabi, Proc. of the 5th Intern. Conf. on Strength of Metals and Alloys, Pergamon Press 1979 pp 1615-1638.

[71] H. Mughrabi, Proc. of 4th Intern. Conf. on Continuum Models of Discrete Systems, O. Brulin, R.K.T. Hsieh, (Eds.), North Holland Publishing Company, Stockholm, Amsterdam, p.241, (1981).

[72] C. Laird, P. Charsely, H. Mughrabi, Low Energy Dislocation Structures, Elsevier Sequoia, Lausanne 1986 pp 433-450.

[73] C.D. Liu, M.N. Bassim, phys. stat. sol. (a) 149 (1995) 331.

[74] F. Ackermann, L.P. Kubin, J. Lepinoux , H. Mughrabi, Acta Mater. 32, No. 5, (1984) 715-725.

[75] C.D. Liu, M.N. Bassim, Phil. Mag. A 70 (4) (1994) 591-605.

[76] A. Abel, Mater. Sci. Eng. 36 (1978) 117-124.

[77] J. Polak, J. Helesic, K. Obrtlik, Mater. Sci. Eng. A101 (1988) 7-12.

[78] P. Schutzner, Doctoral Thesis, Stuttgart University, 1974.

[79] A.T. Winter, O.B. Pedersen and K.V. Rasmussen, Acta Metall. 29 (1981) 735.

[80] P. Charsley, Mater. Sci. Eng. 47 (1981) 181.

[81] D. Kuhlmann-Wilsdorf, C. Laird, Mat. Sci. Eng. 27 (1977) 137.

[82] J.C. Grosskreutz, Phys. Stat. Sol. (b) 47 (1971) 11.

[83] C. Laird, In Treatise on Materials Science and Technology, 6 (1975) 101.

[84] M.A. Meyers, K.K. Chawla, Mechanical Behavior of Materials, (1999) p. 217.

[85] P.R. Swann, Electron Microscopy and Strength of Crystals, (1963) pp. 131-135.

[86] C.E. Feltner, C. Laird, TMS – AIME, vol. 242 (1968) 1253-1257.

[87] D. Kuhlmann-Wilsdorf, Metall. Trans. 1 (1970) 3173.

[88] J. Yan, "Cyclic stress-strain response and dislocation substructures evolution of nickel", PhD Thesis, Clarkson University, 2002